

1995

## Truncated Icosahedral Gravitational Wave Antenna.

Stephen Michael Merkowitz

*Louisiana State University and Agricultural & Mechanical College*

Follow this and additional works at: [https://digitalcommons.lsu.edu/gradschool\\_disstheses](https://digitalcommons.lsu.edu/gradschool_disstheses)

---

### Recommended Citation

Merkowitz, Stephen Michael, "Truncated Icosahedral Gravitational Wave Antenna." (1995). *LSU Historical Dissertations and Theses*. 6033.

[https://digitalcommons.lsu.edu/gradschool\\_disstheses/6033](https://digitalcommons.lsu.edu/gradschool_disstheses/6033)

This Dissertation is brought to you for free and open access by the Graduate School at LSU Digital Commons. It has been accepted for inclusion in LSU Historical Dissertations and Theses by an authorized administrator of LSU Digital Commons. For more information, please contact [gradetd@lsu.edu](mailto:gradetd@lsu.edu).

## **INFORMATION TO USERS**

**This manuscript has been reproduced from the microfilm master. UMI films the text directly from the original or copy submitted. Thus, some thesis and dissertation copies are in typewriter face, while others may be from any type of computer printer.**

**The quality of this reproduction is dependent upon the quality of the copy submitted. Broken or indistinct print, colored or poor quality illustrations and photographs, print bleedthrough, substandard margins, and improper alignment can adversely affect reproduction.**

**In the unlikely event that the author did not send UMI a complete manuscript and there are missing pages, these will be noted. Also, if unauthorized copyright material had to be removed, a note will indicate the deletion.**

**Oversize materials (e.g., maps, drawings, charts) are reproduced by sectioning the original, beginning at the upper left-hand corner and continuing from left to right in equal sections with small overlaps. Each original is also photographed in one exposure and is included in reduced form at the back of the book.**

**Photographs included in the original manuscript have been reproduced xerographically in this copy. Higher quality 6" x 9" black and white photographic prints are available for any photographs or illustrations appearing in this copy for an additional charge. Contact UMI directly to order.**

# **UMI**

A Bell & Howell Information Company  
300 North Zeeb Road, Ann Arbor, MI 48106-1346 USA  
313/761-4700 800/521-0600



# **TRUNCATED ICOSAHEDRAL GRAVITATIONAL WAVE ANTENNA**

**A Dissertation**

**Submitted to the Graduate Faculty of the  
Louisiana State University and  
Agricultural and Mechanical College  
in partial fulfillment of the  
requirements for the degree of  
Doctor of Philosophy**

**in**

**The Department of Physics and Astronomy**

**by  
Stephen Michael Merkowitz  
B.A., University of Colorado, 1989  
M.S., Louisiana State University, 1994  
August 1995**

**UMI Number: 9609107**

---

**UMI Microform 9609107**

**Copyright 1996, by UMI Company. All rights reserved.**

**This microform edition is protected against unauthorized  
copying under Title 17, United States Code.**

---

**UMI**

**300 North Zeeb Road  
Ann Arbor, MI 48103**

# Acknowledgments

As with most aspects of life, the exploration of nature is not a journey that we take alone. The many individuals we meet on the trail influence us in ways that cannot be measured. Their knowledge and experience becomes invaluable to our success. Without their support and guidance we would almost certainly find ourselves lost in the wilderness.

The individual who influenced me the most in this endeavor was my Major Professor, Warren Johnson. Warren's unique insight and intuition led us down paths that I would never have envisioned. His patience and attention to details are qualities we should all strive to obtain.

Warren was also extremely helpful in tracking down the gremlins that were hiding in all aspects of the experiment. How he is able to find a missing factor of root two, at first glance, in an equation with twenty terms I will never know. Warren could sit down at program that I thought was perfect and manage to exploit some undiscovered bug in the code within about 30 seconds. Although Warren would leave a trail of papers whenever he passed

through a room, he would often bring order, direction, and insight to my research.

William Hamilton's management style made working in the gravity lab a pleasure. He would often stand back letting me go in the direction I felt was correct, but once I had gone astray too far he would give me a push in the right direction. By trusting me to make the correct decisions on my own, Bill gave me the confidence I will need to succeed.

While most of the time Bill would stand back and let me investigate on my own, he also was extremely helpful with various aspects of the experiment. As an example, Bill was the first in our group to model a sphere using finite element analysis. His work guided me as I developed the models of a truncated icosahedron. Bill later modeled a truncated icosahedron, but in a different way from my own models. This brought new insights into the problem.

I'm not quite sure how to thank Brad Price. His computer skills were invaluable for setting up and maintaining the data acquisition system. However, (perhaps motivated by a bet for a case of beer) he introduced me to aspects of the computer world that were both intriguing and distracting. While I may have graduated earlier had he not led me down this path, I would not have had as much fun making the journey.

When Brad was not around, I could always count on Evan Mauceli and Andrew Morse to help me forget the problems of the day. Late night Bolo and Saturday morning basketball kept me from immersing myself in my research

too deeply. Without them, these past two years would have been much more humdrum than they were.

Norbert Solomonson and Kenny Geng were also invaluable in their assistance with various aspects of my research. Both are very experimentally talented; having experience and knowledge about the practical problems that exist in experimental work. I could always count on them to assist me with various aspects of the experiment that I could not solve myself.

Much credit should be given to Nadja Magalhães for her direction finding methods. Her work directly led me to the use of the cartesian strain tensor to find the direction of an impulse to the prototype.

Other individuals who were directly helpful and provided many useful discussions are: Odelio Aguiar, Massimo Visco, Carlos Frajuca, and the members of the Gravity Co-op.

I thank the faculty of the LSU physics department. I found this department to support an environment that encouraged interaction between the graduate students and the faculty that I believe to be rare. Special thanks go to Dana Browne, Richard Haymaker, Lai-Him Chan, Ganesh Chanmugam, Philip Adams, and Greg Guzik. Their teachings and assistance made this research possible.

My thanks go to everyone in the electronics and machine shop. Without their assistance, much of the equipment needed for this research could not have been built.



I also thank the staff of the LSU physics department. They brought me a joyful reminder that, without leaving the building, there is life outside of physics. Life in the physics department was much more difficult before Jim Fernandez came. He brought with him the skill to “work the system”, in order to get things done quickly, that was desperately missing. I thank Ophelia Dudley for her friendship. Special thanks also go to Karla Tuley, Karen Richard, Beverly Rodriguez, and Cathy Mixon. Special special thanks go to Karen Jacobs, who walked all over campus for me making my defense possible.

Finally, I thank Grettel Bustos and my family. Their love and support has helped make this research possible.

This research was supported by the National Science Foundation under Grant No. PHY-9311731.

# Contents

Acknowledgments . . . . .	ii
Abstract . . . . .	viii
1 Introduction . . . . .	1
1.1 Gravitational Waves . . . . .	3
1.2 Brief History of Resonant Mass Gravitational Wave Antennas . . . . .	8
1.3 Antenna Sensitivity . . . . .	9
1.4 Spherical Antennas . . . . .	12
2 Spherical Gravitational Wave Antennas . . . . .	14
2.1 Quadrupole Decomposition of the Gravitational Field .	15
2.2 The General Antenna . . . . .	19
2.3 The Uncoupled Sphere . . . . .	22
2.4 Sphere with Resonators . . . . .	26
2.5 Spectral Sensitivity . . . . .	39
2.6 Comparison of the TIGA to other Detectors . . . . .	48
2.7 Extensions . . . . .	52
3 TIGA Design . . . . .	54
3.1 Finite element analysis . . . . .	54
3.2 Geometry and Design . . . . .	57
3.3 Prototype Machining . . . . .	58
3.4 Suspension . . . . .	61
4 The Uncoupled Prototype . . . . .	63
4.1 Data Acquisition System . . . . .	63
4.2 Instrumentation . . . . .	70

4.3	Uncoupled Antenna Spectrum . . . . .	71
4.4	Accelerometer Calibration . . . . .	75
4.5	Mode Shape Analysis Methods . . . . .	78
4.6	Separation into Mode Channels . . . . .	82
4.7	Mode Response . . . . .	85
4.8	Impulse Direction . . . . .	90
4.9	Experimental Obstacles . . . . .	94
5	Summary . . . . .	96
	References . . . . .	99
A	Solution of the Equations of Motion . . . . .	102
B	Prototype with Resonators . . . . .	106
B.1	Resonator Design and Tuning . . . . .	106
B.2	Attachment of the Resonators . . . . .	110
B.3	Coupled Antenna Spectra . . . . .	113
C	Programs . . . . .	116
D	Letter of Permission . . . . .	131
	Vita . . . . .	134

# Abstract

A spherical gravitational wave detector can be equally sensitive to a wave from any direction, and also able to measure its direction and polarization. We derive a set of equations to describe the mechanics of a spherical antenna coupled to an arbitrary number of attached mechanical resonators. A special arrangement of 6 resonators is proposed, which we term a Truncated Icosahedral Gravitational Wave Antenna, or TIGA. An analytic solution to the equations of motion is found for this case. We find that direct deconvolution of the gravitational tensor components can be accomplished with a specified set of linear combinations of the resonator outputs, which we call the mode channels. We develop one simple noise model for this system and calculate the resulting strain noise spectrum. We conclude that the angle-averaged energy sensitivity will be 56 times better than for the typical equivalent bar-type antenna with the same noise temperature.

We have constructed a prototype TIGA. This shape was machined from an Al 6063 cylindrical bar, is 84 cm in diameter, has its first quadrupole resonances near 3200 Hz, and is suspended from its center of mass. The

frequencies of the lowest seven multiplets were found to closely match those calculated for a sphere. We observed the motion of the prototype's surface using 6 accelerometers attached to its surface in the symmetric truncated icosahedral arrangement. We have tested a first order direction finding algorithm, which uses fixed linear combinations of six accelerometer responses to first infer the relative amplitudes of the quadrupole modes and from these the location of the impulse.

The six accelerometers were then replaced by six mechanical resonators. A strain gauge was used to monitor the radial motion of each resonator. The frequency response of the coupled system was measured and compared to the eigenvalue solutions of the equations of motion. It was concluded that deviations from perfect symmetry have a second order effect on our ability to observe the prototype's quadrupole modes and thus determine the location and direction of the initial excitation.

# Chapter 1

## Introduction

One of the first predictions of Einstein's Theory of General Relativity was the existence of gravitational waves. Gravitational waves are predicted to propagate at the speed of light and represent a time-dependent distortion of the local space and time coordinates. Just as electromagnetic waves are produced by the acceleration of charge, gravitational waves are predicted to be produced by the acceleration of mass. Gravitational waves, however, differ from electromagnetic waves in a number of ways. While only a single charge is needed to produce electromagnetic waves, at least two masses are required to produce gravitational waves. The gravitational field is also very weak so that only catastrophic events are expected to produce detectable waves. Possible events include the collision of two astronomical objects and the collapse of a large astronomical object.

Confirmed detection of gravitational waves from astrophysical sources will found a new astronomy and allow direct investigation of the gravitational force under extreme conditions. The best current antennas, such as the LSU ALLEGRO detector [1], are sensitive enough to detect a gravitational collapse in our galaxy, if the energy converted is a few percent of a solar mass. However, the conventional wisdom is that we need to look at least 3 orders of magnitude further in distance, out to the Virgo Cluster, to have an “assured” event rate of several per year. This requires improving the energy resolution of the detector by 6 orders of magnitude. The best known methods for improving cryogenic resonant-mass detectors will contribute by lowering the noise temperature,  $T_n$ , from its current value of  $\approx 7\text{mK}$ . It is commonly believed that quantum noise will present a formidable barrier for improvement by more than  $10^5$ , not quite enough for “assured” detection.

There are other ways to improve resonant-mass antennas that are independent of the noise temperature. A spherical antenna has a number of inherent properties that give it an advantage over other types of detectors. A sphere will have a larger mass than an equivalent bar (bar with the same resonant frequency). The larger mass translates into an increased cross section, thus improving the sensitivity of the antenna. A single sphere is also capable of detecting gravitational waves from all directions and polarizations. One would have to construct 5 equivalent bars to obtain the same amount of information. Therefore, a sphere can be thought of 5 detectors in a single instrument. A sphere is also capable of determining the direction information and tensorial character of an incident gravitational wave.

With these obvious advantages, why has no one built a spherical antenna before? First, the extra four modes that strongly couple to a gravitational wave add an extra layer of complexity to the system. Second, a bare sphere is not a practical detector. Mechanical resonators must be attached to the surface of the sphere to turn the small motion of the sphere surface into large motions of the resonators, providing an essential increase in coupling. A minimum of 5 mechanical resonators must be attached to the sphere in order to record all the information about the modes that strongly interact with a gravitational wave. These resonators will couple to the sphere modes resulting in a total of at least 10 coupled modes. These complications along with other practical problems (such as vibration isolation) have deterred people from attempting to construct a spherical gravitational wave detector.

In this dissertation, we will show that it is possible to deconvolve the complexities of a sphere coupled to a set of mechanical resonators. We have developed a theory that enables us to reconstruct all the information about an incident gravitational wave from the motion of the mechanical resonators. We have also constructed a room-temperature prototype antenna, and have shown that the problems associated with the breaking of perfect symmetry assumed in the theory can be solved in practice.

## 1.1 Gravitational Waves

This section provides a brief overview of gravitational waves within the theory of General Relativity. For a more detailed discussion we direct the reader to the standard texts [2, 3].



The theory of General Relativity predicts that gravitational waves will be produced by a time varying quadrupole moment. The wave itself creates a time varying tidal force that propagates at the speed of light. The field of a gravitational wave is often described by a time dependent strain tensor  $h_{\alpha\beta}(t)$ . The size of the strain tensor will indicate how strongly the gravitational wave will curve spacetime.

A gravitational wave will induce a stress an extended body. For a bar antenna, the stress from a gravitational wave will cause the ends of the bar to contract and expand. The force that a gravitational wave exerts on the bar depends on both the density of the bar's material as well as the bar's length. By increasing the mass of the bar we increase the force a gravitational wave exerts on the bar, thus increasing the bar's cross-section.

The gravitational wave field is transverse and traceless, i.e. if we orient our spatial axis so that the wave propagates in the  $z$  direction, then the only non-zero components to the wave field are  $h_{xx} = -h_{yy}$  and  $h_{xy} = h_{yx}$ . The field has only two independent components, or polarization states.

We define two polarization amplitudes, which we call plus and cross (+ and  $\times$ ), in terms of the components of the wave field:

$$h_+ \equiv h_{xx} = -h_{yy} \quad (1.1)$$

$$h_\times \equiv h_{xy} = h_{yx} \quad (1.2)$$

Figure 1.1 shows the effect on a ring of test masses from a polarized wave traveling in the  $z$  direction. The wave will compress the ring in one direction,

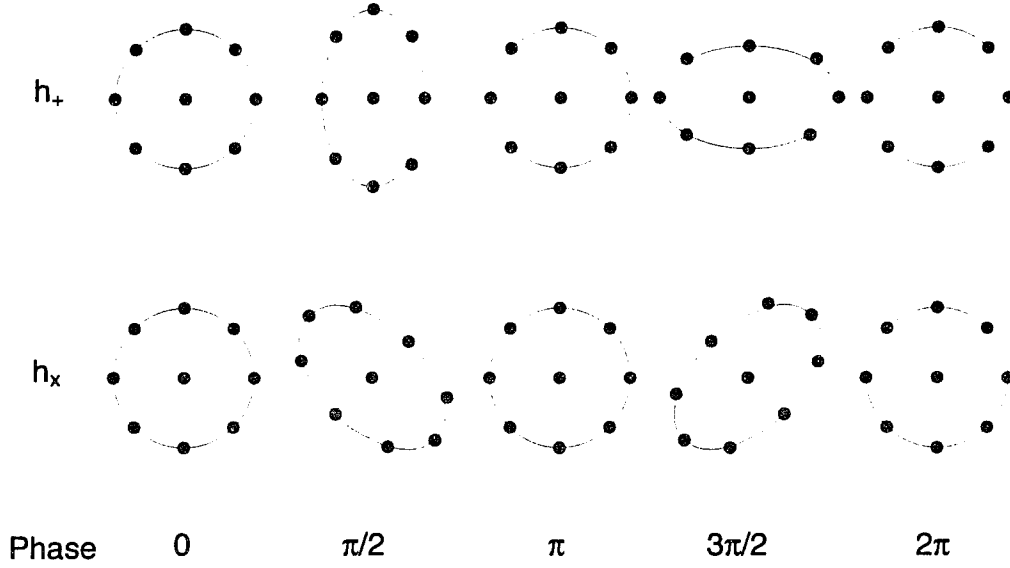


Figure 1.1: The distortion of a ring of test particles during one cycle of a gravitational wave traveling in the  $z$  direction. The effect of both linear polarizations is shown.

while expanding it in the other. The two polarizations are equivalent except for a  $45^\circ$  rotation about the propagation axis.

Gravitational waves from astrophysical sources can be divided into three classes: bursts, periodic waves, and stochastic waves. Bursts are emissions that last for a very short time, only a few cycles. Potential sources of bursts include: the collapse of a star to a neutron star or black hole, coalescence of compact binaries, and the fall of stars and small black holes into supermassive black holes. Sources of periodic waves include: rotating neutron stars and binary stars. Stochastic waves are a potential stationary random background of gravitational waves. A stochastic background might come from primordial gravitational waves or from the superposition of the radiation from a large population of binary stars in our galaxy and other galaxies.

Burst sources are the most likely to have large amplitudes at higher frequency; therefore, they are the best candidates for detection by resonant mass detectors. The signal to noise ratio of a burst signal in the detector can be shown to be [2, 4]:

$$\frac{S}{N} = \frac{h_c}{h_n}. \quad (1.3)$$

where  $h_n$  is the overall detector noise, often referred to as the “burst” noise. It is defined, in terms of power spectral density  $S_h$ , as

$$h_n = \left( 2 \int_0^\infty S_h^{-1}(\omega) \frac{d\omega}{2\pi} \right)^{-\frac{1}{2}}. \quad (1.4)$$

The characteristic strength of the source,  $h_c(f_c)$ , can be written in terms of the total energy  $\Delta E_{\text{GW}}$  radiated as gravitational waves [2]:

$$h_c \simeq 2.7 \times 10^{-20} \left( \frac{\Delta E_{\text{GW}}}{M_\odot c^2} \right)^{\frac{1}{2}} \left( \frac{1\text{kHz}}{f_c} \right)^{\frac{1}{2}} \left( \frac{10\text{Mpc}}{r_0} \right), \quad (1.5)$$

where  $f_c$  is the resonant frequency of the detector, assumed to coincide with the characteristic frequency of the burst source,  $M_\odot$  is the mass of the sun, and  $r_0$  is the distance to the source. Equation 1.5 is a convenient way to express the strength of a wave relative to the estimated distance to the Virgo cluster (10 Mpc) where many sources of burst gravitational waves are expected to exist [5].

Burst sources must be very violent events. One candidate is the gravitational collapse of a massive star to form a neutron star. The strength of

emission depends on the degree of non-sphericity in the collapse and also on the speed of the collapse. A perfectly spherical collapse will produce no waves, whereas a highly antisymmetric collapse will produce strong waves. The burst of gravitational waves will cover a large frequency bandwidth, however the newly created neutron star is expected to have quadrupole modes that resonate on the order of 1 kHz, creating gravitational waves at that frequency. Supernovae are thought to occur at a rate of about one per 40 years in our galaxy and at a rate of several per year at a distance out to the center of the Virgo cluster.

A gravitational collapse might also form a black hole instead of a neutron star. Again, the greater the non-sphericity the collapse, the stronger the gravitational waves emitted. The rate for this type of collapse is predicted to be about 1/3 the rate for collapse to a neutron star [2].

A third source for bursts is the coalescence of compact binaries. These are close binary systems containing neutron stars or black holes. The binary pulsar PSR1913+16 is an example of a coalescing binary; it is predicted to coalesce in  $3.5 \times 10^8$  years.

Although there has not been any confirmed direct evidence of gravitational waves, there is strong indirect evidence of their existence. In 1975 Hulse and Taylor observed the binary pulsar PSR1913+16, whose period changes at a rate consistent with General Relativistic predictions of gravitational wave emissions [6]. For the past 20 years astronomers have continued to observe the pulsar and to this day, the orbital decay remains consistent with the predictions of General Relativity.

## 1.2 Brief History of Resonant Mass Gravitational Wave Antennas

For more than 25 years, gravitational waves have eluded confirmed experimental detection. The pioneering proposal to detect gravitational waves was made by Weber in the early 1960's. He proposed using a large piezoelectric crystal to detect the oscillating strain produced by an oscillating gravitational field [7].

By 1966 Weber had constructed the first resonant-mass gravitational wave antenna [8]. It was a large, room-temperature aluminum bar that was vibrationally isolated in a vacuum chamber. Quartz strain gauges were used to monitor the bar's fundamental mode of vibration. By 1969 Weber had achieved strain sensitivities of a few parts in  $10^{16}$  and had constructed several more gravitational wave detectors. He soon announced that he had observed coincidences between them [9]. These results generated great excitement in the field and other groups began constructing gravitational wave detectors. In the end, however, Weber's findings could not be confirmed by other groups who built similar detectors.

By the early 1970's other groups were involved in building advanced gravitational wave detectors. These groups made a number of significant improvements over Weber's original design. One improvement was to lower the temperature of the bar to liquid helium temperatures (4 Kelvin) [10]. The second was a better suspension of the bar with increased vibration isolation. A third was the use of a *resonant* transducer and low noise amplifier to observe the motion of the bar. The small resonator not only amplified the

displacement but attenuated large amplitude vibrations at low frequencies. Today there are three detectors of this type being operated: the LSU ALLEGRO detector [1], the Rome EXPLORER detector [11], and the Australian detector [12].

In 1991 the first tests of an *ultra*-low-temperature (50 mK) detector were performed [13]. Although the expected improvements have not yet been demonstrated, the techniques look promising.

The best current antennas, such as the LSU ALLEGRO detector [1], are sensitive enough to detect a gravitational collapse in our galaxy, if the energy converted to gravitational waves is a few percent of a solar mass. However, the conventional wisdom is that we need to look at least 3 orders of magnitude further in distance, out to the Virgo Cluster, to have an “assured” event rate of several per year. This requires improving the energy resolution of the detector by 6 orders of magnitude.

### 1.3 Antenna Sensitivity

A gravitational wave produces a spatially varying force, or stress, that will stretch and compress a bar antenna. This stress does work, thus energy can be added to or subtracted from the antenna. The more massive the antenna, the greater the amount of energy change. In other words, the gravitational force causes changes in the vibrational amplitude or phase of the antenna. It is this change in state that we try to detect.

By making the antenna's quadrupole modes resonant at the wave's frequency, the detector keeps a "memory" of the excitation, allowing extra time to detect the signal. Instead of looking at an instant of data, we can integrate over longer periods of time to look for changes in the amplitude or phase of the detector.

The sensitivity of an antenna can be improved by a number of ways. First, we can increase the force a gravitational wave will exert on the antenna by increasing its mass (see equation 2.2 in the next chapter). Second, we can make the antenna equally sensitive to all directions and polarizations. Third, we can lower the noise temperature (level of excitation from non-gravitational sources) of the antenna. Although the main portion of this dissertation is not concerned with noise temperature, we briefly describe here the physical mechanisms that determine the noise of the antenna.

There are many *non-gravitational* sources that can excite the resonances of the detector. The largest of these sources can be external vibrations, such as ground noise. A sophisticated vibration isolation system is necessary to keep these forces from exciting the antenna.

Thermal noise will also contribute to the noise of the system. The thermal energy is proportional to the temperature of the detector, so cooling the antenna to very low temperatures will lower the noise of the system. The thermal energy is also proportional to the relaxation time of the resonant mass. By using high-Q material, such as Aluminum alloy 5056, the transfer of energy to and from the heat bath will be much slower. If we keep the

integration time of our observations short, the effect of the thermal noise can be minimized. By increasing the  $Q$  of the system we not only lower the size of the noise spectrum of the detector, but give ourselves the possibility of using a longer integration time before the thermal noise dominates.

Another source of noise comes from the motion sensors. This type of noise can be referred to as “series” noise. This is an additive noise that usually comes from the first electronic amplifier. It is wide band and does not indicate excitation of the detector. A longer integration time reduces the effect of broad band noise, so it behaves in an opposite manner to thermal noise. This is another reason to require a high- $Q$  system: it reduces the effect of “force noise” on the system allowing you to use a longer integration time. The series noise can also be reduced in the obvious way by reducing the amplifier noise.

Another way to improve the signal to noise ratio is to increase the coupling,  $\beta$ , of the transducer to the antenna. Increased coupling will boost the amount of signal energy transferred to the motion sensor without increasing the series noise, so there will be a net gain in signal to noise.

The motion sensors can also generate a force noise that can excite the resonant mass. This type of noise is referred to as back-action noise. Just as the transducer can see what the large mass is doing, the large mass can also see what the transducer is doing. Increasing the coupling  $\beta$  will cause more back-action noise to be transferred to the antenna.



## 1.4 Spherical Antennas

There are other ways to improve resonant-mass antennas that are independent of the noise temperature. One way is to increase the cross-section of the antenna. Another is to construct many antennas, each aimed in a different direction, so every source direction and polarization will be in the most sensitive part of at least one antenna pattern. This method adds the ability to determine source direction and polarization. A “spherical” antenna will provide all three advantages in a single instrument. We use the word “spherical” for any shape that approximates a true sphere and has equivalent quadrupole vibrational modes.

The important question becomes: what quantitative improvement can a sphere actually deliver? We have invented a design for a nearly spherical antenna, which we call a Truncated Icosahedral Gravitational Wave Antenna [14], or TIGA, that provides a straightforward solution to certain complications of a spherical antenna, and lets us calculate the quantitative improvement. We conclude that a TIGA will be about 56 times more sensitive in energy than the typical equivalent bar-type antenna with the same noise temperature  $T_n$ . Combined with a quantum limited  $T_n$ , this is a sufficient factor to increase our range by more than the desired factor. If we further assume construction of a set of detectors for different frequencies, (a “xylophone”), the sensitivity is further improved and wave form information can be obtained.

It was recognized long ago [15] that a sphere is a very natural shape for a resonant mass detector of gravitational waves. A free sphere has five degenerate quadrupole modes of vibration that will interact strongly with a gravitational wave. Each free mode can act as a separate antenna, oriented towards a different polarization or direction. Wagoner and Paik [16] found a set of equations to determine the source direction in the celestial hemisphere from the free mode amplitudes. Compared to a bar with the same quadrupole mode frequency and a typical length to diameter ratio of 4.2, the improvement in cross-section is about a factor of 60.

That result was ignored, perhaps because a simple spherical resonator is not a practical detector. One requirement for practicality is a set of secondary mechanical resonators. All successful cryogenic bar-type detectors have such resonators; they act as mechanical-impedance transformers between the primary vibrational modes of the antenna and the actual motion sensors, producing an essential increase in the electro-mechanical coupling. We expect that a sphere with five primary modes will require at least five secondary resonators. Another requirement for practicality is a clear method for spatial deconvolution of the signal, so we can determine its direction and polarization. A third requirement is a way to quantify the noise when multiple motion sensors are used.

## Chapter 2

# Spherical Gravitational Wave Antennas<sup>1</sup>

We present here detailed calculations for the sensitivity of a spherical detector for a case where the secondary resonators have a particular useful symmetry. This chapter reproduces our discussion, with minor additions, published recently in *Physical Review D* [17], copyright 1995 The American Physical Society (see Appendix D for letter of permission).

We begin by introducing the quadrupolar decomposition of the gravitational field in section 2.1. Section 2.2 reviews the fundamental mechanical equations and the eigenfunction expansion for a general antenna. Section 2.3 reviews the quadrupolar eigenfunctions for a sphere and shows that they exactly match the quadrupolar decomposition of the gravitational field. A derivation of a general model for coupling resonators to a sphere is presented

---

<sup>1</sup>Reprinted with permission from *Physical Review D* **51**, 2546 (1995), “Spherical Gravitational Wave Antennas and the Truncated Icosahedral Arrangement” by S. Merkowitz and W. Johnson. Copyright 1995 The American Physical Society.

in section 2.4. A special geometry (the “TIGA configuration”) is introduced that simplifies the behavior of the coupled system, and allows us to obtain a general analytic solution. A direct, one-to-one, readout for each of the quadrupolar components of the gravitational field is provided by a linear combination of the resonator outputs, called “mode channels.” The behavior of the complete system is illustrated with a numerical simulation of its response to waves with different directions and polarizations. Section 2.5 develops a simple noise model, and calculates the resulting “spectral sensitivity” of the detector. Section 2.6 compares the spectral sensitivities of several detectors.

## 2.1 Quadrupole Decomposition of the Gravitational Field

A gravitational wave is a traveling time-dependent deviation of the metric tensor, denoted by  $h_{\mu\nu}$ . We follow a common textbook development for the metric deviation of a gravitational wave, which finds that only the spatial components,  $h_{ij}$ , are non-zero, and further can be taken to be transverse and traceless [2]. The tensor is simplified if we initially write it in the “wave-frame”, denoted by primed coordinates and primed indices. It is a coordinate frame with origin at the center of mass of the detector, and the  $z'$ -axis aligned with the propagation direction of the wave. Since we restrict ourselves to detectors much smaller than the gravitational wavelength, only the time dependence of  $h_{i'j'}$  will have significant physical effects. Thus, the most

general possible form for the spatial components of the metric deviation in the wave-frame can be written as:

$$h_{i'j'}(t) = \begin{bmatrix} h'_+(t) & h'_\times(t) & 0 \\ h'_\times(t) & -h'_+(t) & 0 \\ 0 & 0 & 0 \end{bmatrix} \quad (2.1)$$

where  $h'_+$  and  $h'_\times$  are the wave amplitudes for the two allowed states of linear polarization, and are called the plus and cross amplitudes.

The detector is more easily described in the “lab-frame”, denoted by unprimed coordinates and indices, with origin also at the center of mass of the detector, and  $z$ -axis aligned with the local vertical. In this frame, the primary physical effect of a passing gravitational wave is to produce a time dependent “tidal” force density  $f^{\text{GW}}(\mathbf{x}, t)$  on material at coordinate location  $x_i$  with mass density  $\rho$ , which is related to the metric perturbation by

$$f_i^{\text{GW}}(\mathbf{x}, t) = \frac{1}{2}\rho \sum_j \frac{\partial^2 h_{ij}(t)}{\partial t^2} x_j. \quad (2.2)$$

We notice that this force can be written as the gradient of a time-dependent scalar potential:

$$f_i^{\text{GW}}(\mathbf{x}, t) = \nabla_i \Phi(\mathbf{x}, t) = \nabla_i \left( \sum_{j,k} \frac{1}{4} \rho x_j \ddot{h}_{jk}(t) x_k \right). \quad (2.3)$$

This scalar potential is a quadratic form in the spatial coordinates. It is natural to look for an alternate expression that separates the coordinate

dependence into radial and angular parts. Because the tensor  $h_{ij}$  is traceless, the angular expansion can be done completely with the five ordinary spherical harmonics of order 2, which we denote by  $Y_m(\theta, \phi)$  or  $Y_m$ . We call the resulting time dependent expansion coefficients, denoted by  $h_m(t)$ , the “spherical amplitudes.” They are a complete and orthogonal representation of the cartesian metric deviation tensor  $h_{ij}(t)$ . They depend only on the two wave-frame amplitudes and the direction of propagation, and are defined by

$$\Phi(\mathbf{x}, t) = \sqrt{\frac{\pi}{15}} \rho r^2 \sum_m \ddot{h}_m(t) Y_m. \quad (2.4)$$

We have found it convenient to use a set of spherical harmonics  $Y_m$  that are linear combinations of the usual complex-valued spherical harmonics  $Y_{2m}$  [18]. We define them by

$$Y_1 = \sqrt{\frac{1}{2}} (Y_{22} + Y_{2-2}) = \sqrt{\frac{15}{16\pi}} \frac{(x^2 - y^2)}{r^2} \quad (2.5)$$

$$Y_2 = \sqrt{\frac{1}{2}} i (Y_{2-2} - Y_{22}) = \sqrt{\frac{15}{16\pi}} \frac{2xy}{r^2} \quad (2.6)$$

$$Y_3 = \sqrt{\frac{1}{2}} (Y_{21} + Y_{2-1}) = \sqrt{\frac{15}{16\pi}} \frac{2yz}{r^2} \quad (2.7)$$

$$Y_4 = \sqrt{\frac{1}{2}} i (Y_{2-1} - Y_{21}) = \sqrt{\frac{15}{16\pi}} \frac{2xz}{r^2} \quad (2.8)$$

$$Y_5 = Y_{20} = \sqrt{\frac{15}{16\pi}} \frac{(3z^2 - r^2)}{r^2 \sqrt{3}} \quad (2.9)$$

They are normalized such that  $\int Y_m \cdot Y_n d\Omega = \delta_{mn}$ .

To transform the metric perturbation to the lab-frame we perform the appropriate rotations, using the y-convention for the Euler angles [19]. Ordinarily, without making any assumptions about the source, we do not know the initial state of the polarizations; we may therefore ignore the rotation about the original  $z'$ -axis because this rotation only mixes the two polarizations and has no effect in determining the direction of the wave. We denote the rotation about the  $y'$ -axis by  $\beta$  and the rotation about the new  $z$ -axis by  $\gamma$ . The spherical amplitudes in the lab frame can now be written in terms of the gravitational wave amplitudes:

$$h_1(t) = h'_+(t) \frac{1}{2} (1 + \cos^2 \beta) \cos 2\gamma + h'_\times(t) \cos \beta \sin 2\gamma \quad (2.10)$$

$$h_2(t) = -h'_+(t) \frac{1}{2} (1 + \cos^2 \beta) \sin 2\gamma + h'_\times(t) \cos \beta \cos 2\gamma \quad (2.11)$$

$$h_3(t) = -h'_+(t) \frac{1}{2} \sin 2\beta \sin \gamma + h'_\times(t) \sin \beta \cos \gamma \quad (2.12)$$

$$h_4(t) = h'_+(t) \frac{1}{2} \sin 2\beta \cos \gamma + h'_\times(t) \sin \beta \sin \gamma \quad (2.13)$$

$$h_5(t) = h'_+(t) \frac{1}{2} \sqrt{3} \sin^2 \beta \quad (2.14)$$

If the lab  $x$ -axis points South and the lab  $z$ -axis is the local zenith, then the source has a zenith distance  $= \beta$  and an azimuth (degrees East of North along the horizon)  $= \gamma$ .

The five orthogonal spherical amplitudes  $h_m$  are the complete set of measurable quantities of the local gravitational field within General Relativity.

Combining equations (2.3) and (2.4) we can write the cartesian strain tensor in terms of the five spherical amplitudes:

$$h_{ij}(t) = \begin{bmatrix} h_1 - \frac{1}{\sqrt{3}}h_5 & h_2 & h_4 \\ h_2 & -h_1 - \frac{1}{\sqrt{3}}h_5 & h_3 \\ h_4 & h_3 & \frac{2}{\sqrt{3}}h_5 \end{bmatrix} \quad (2.15)$$

For a wave traveling in an arbitrary direction, the cartesian strain tensor will have non-zero off diagonal elements. The determination of the source direction follows immediately by solving equation (2.15) for its eigenvalues and eigenvectors. For a transverse wave, the diagonalized tensor will have non-zero  $h_{1'1'}$  and  $h_{2'2'}$  components. The  $h_{3'3'}$  component will be zero, but its eigenvector will point in the direction of the incident gravitational wave. The position determination is only unique within a hemisphere; sources in opposite directions are indistinguishable. Other descriptions of determining the source direction from a spherical detector have been discussed by others [20, 21].

## 2.2 The General Antenna

The mechanics of a general antenna can be described by ordinary elastic theory. Forces acting on the body will cause a deformation described by the displacement vector  $\mathbf{u}(\mathbf{x}, t)$ , where  $\mathbf{x}$  is the equilibrium position of a mass



element. The equations of motion for an isotropic elastic body are

$$\rho \frac{\partial^2 \mathbf{u}}{\partial t^2} = (\lambda + \mu) \nabla (\nabla \cdot \mathbf{u}) + \mu \nabla^2 \mathbf{u} + \sum \mathbf{f}. \quad (2.16)$$

where the Lamé coefficients  $\lambda$  and  $\mu$  specify the elastic stiffness of the material and  $\sum \mathbf{f}$  represents the sum of external force densities acting on the body [22].

We include two forces in  $\sum \mathbf{f}$ . First, the signal or gravitational force density,  $\mathbf{f}^{\text{GW}}$ , from equation (2.2). Second, if objects are attached to the antenna, there will exist a reaction force between the object and the surface of the antenna. Thus we choose to express the coupling to other objects, such as secondary resonators, as if they were external forces in equation (2.16). This device lets us partition the equations of motion in a convenient way.

A solution to the differential equation (2.16) can be found by the standard eigenfunction expansion. This allows a separation of the spatial and time dependence of the displacement vector,

$$\mathbf{u}(\mathbf{x}_i, t) = \sum_m a_m(t) \Psi_m(\mathbf{x}_i). \quad (2.17)$$

Each spatial eigenfunction,  $\Psi_m(\mathbf{x})$ , is the time independent part of the solution for unforced harmonic oscillation at the eigenfrequency  $\omega_m$ , and is found by solving

$$-\rho \omega_m^2 \Psi_m = (\lambda + \mu) \nabla (\nabla \cdot \Psi_m) + \mu \nabla^2 \Psi_m, \quad (2.18)$$

subject to the time-stationary boundary conditions, which for a sphere require that the total force per unit area at the surface vanish in the direction

normal to the surface. The quantity  $a_m(t)$  is the time-dependent mode amplitude. The mode index,  $m$ , enumerates the discrete set of modes, which obey the usual orthogonality property

$$\int_V \Psi_m(\mathbf{x}) \cdot \Psi_n(\mathbf{x}) d^3x = N_m \delta_{mn}. \quad (2.19)$$

The normalization constant,  $N_m$ , is arbitrary.

Combining the equations above, and using orthogonality to eliminate the summation, we find the standard result, one forced harmonic oscillator equation for each mode amplitude,

$$\ddot{a}_m(t) + \omega_m^2 a_m(t) = \frac{1}{\rho N_m} \int \Psi_m(\mathbf{x}) \cdot \sum \mathbf{f}(\mathbf{x}, t) d^3x. \quad (2.20)$$

When comparing different calculations, one source of possible confusion is the arbitrary choice of normalization constant  $N_m$ . It determines the units and the precise physical interpretation of both the mode amplitudes  $a_m$  and the eigenfunctions  $\Psi_m$ .

The mode amplitudes are a complete set of collective coordinates for the description of the antenna motion. All the interactions with the outside world, including gravitation, can be included as separate terms in the “effective force” on each mode. An efficient approximation scheme will use only those modes needed for an accurate description of the antenna. Only a few of the “overlap integrals” with  $\mathbf{f}^{\text{GW}}$  in equation (2.20) are large, so that only a few of the mode amplitudes are strongly coupled to gravitational waves.

## 2.3 The Uncoupled Sphere

Let us consider a perfectly homogeneous and isotropic sphere uncoupled from the outside world. Its eigenfunctions were found over a hundred years ago by Jaerisch [23] and Lamb [24]. More elegant derivations, using modern notation, were found by Ashby and Dreitlein [25], and Wagoner and Paik [16]. We summarize their results.

The eigenfunctions of a sphere can be described in terms of spherical harmonics  $Y_{\ell m}(\theta, \phi)$ . Looking at the overlap integral in equation (2.20), we see that we need only consider odd-parity modes. For a sphere of radius  $R$  the eigenfunctions are written:

$$\Psi_{\ell m} = [\alpha_{\ell}(r)\hat{\mathbf{r}} + \beta_{\ell}(r)R\nabla] Y_{\ell m}(\theta, \phi), \quad \ell \text{ even.} \quad (2.21)$$

The radial eigenfunctions  $\alpha_{\ell}(r)$  and  $\beta_{\ell}(r)$  determine the motion in the radial and tangential directions respectively. There are five quadrupole modes of vibration which strongly couple to the force density of a gravitational wave, and are all degenerate, having the same angular eigenfrequency  $\omega_o$ . They are distinguished only by their angular dependence. Figure 2.1 shows the shape of the quadrupole modes. For the remainder of this discussion we will only consider the quadrupole ( $\ell = 2$ ) modes so we will drop the  $\ell$  in our notation.

The radial eigenfunctions are given by Ashby and Dreitlein:

$$\alpha(r) = cR \frac{\partial}{\partial r} j_2(qr) + 6dR \frac{1}{r} j_2(kr) \quad (2.22)$$

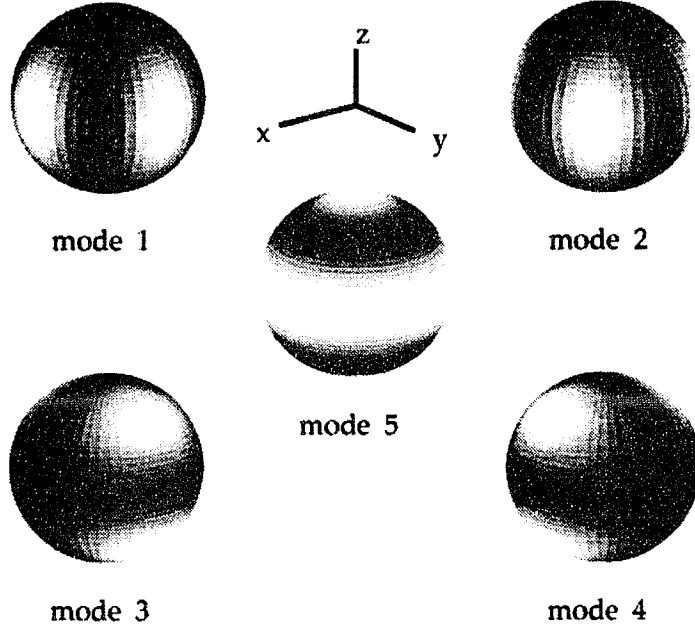


Figure 2.1: The shape of the quadrupole modes. The shading indicates the amplitude of radial motion. The dark regions have little or no radial motion; the lightest regions have the maximum of radial motion.

$$\beta(r) = cj_2(qr) + d \frac{\partial}{\partial r} [rj_2(kr)] \quad (2.23)$$

Their dependence on Poisson's ratio is shown in Figure 2.2. Here,  $j_2$  is the spherical Bessel function of order 2. The longitudinal and transverse wave vectors are given by  $q^2 = \rho\omega_o^2/(\lambda + 2\mu)$  and  $k^2 = \rho\omega_o^2/\mu$  respectively. The boundary conditions,

$$c \frac{d}{dr} \left[ \frac{j_2(qr)}{r} \right] + d \left[ \frac{5}{r^2} - \frac{k^2}{2} - \frac{1}{r} \frac{d}{dr} \right] j_2(kr) \Big|_{r=R} = 0, \quad (2.24)$$

$$c \left[ \frac{6}{r^2} - \frac{k^2}{2} - \frac{2}{r} \frac{d}{dr} \right] j_2(qr) + 6d \frac{d}{dr} \left[ \frac{j_2(kr)}{r} \right] \Big|_{r=R} = 0, \quad (2.25)$$

determine the uncoupled mode frequency  $\omega_o$ . Its dependence on Poisson's ratio is shown in Figure 2.3. Inclusion of a normalization condition,

$$N_m \equiv \frac{4}{3} \pi R^3, \quad (2.26)$$

determines the constants  $c$  and  $d$ . These coefficients specify the shape of the eigenfunctions. They are all weakly dependent on Poisson's ratio, as shown in Figure 2.4.

The gravitational effective force for mode  $m$  of the sphere,  $F_m^S$ , from equation (2.20) is

$$F_m^S \equiv \int_{V_o} \Psi_m \cdot \mathbf{f}^{\text{GW}} d^3x. \quad (2.27)$$

Solving the integrals, using equations (2.3) and (2.21), we find

$$\begin{aligned} F_m^S(t) &= \sqrt{\frac{4\pi}{15}} \rho \ddot{h}_m(t) R^4 [c j_2(qR) + 3d j_2(kR)] \\ &= \frac{1}{2} \ddot{h}_m(t) m_S \chi R. \end{aligned} \quad (2.28)$$

Thus we have that each spherical component of the gravitational field determines uniquely the effective force on the corresponding mode of a sphere, and they are all identical in magnitude. We can interpret the effective force  $F_m^S$  in each mode as the product of: the physical mass of the sphere  $m_S$ , an effective length  $\chi R$ , and the gravitational acceleration  $\frac{1}{2} \ddot{h}_m$ . The factor  $\chi$  is a weak function of Poisson's Ratio, and is shown in Figure 2.5.

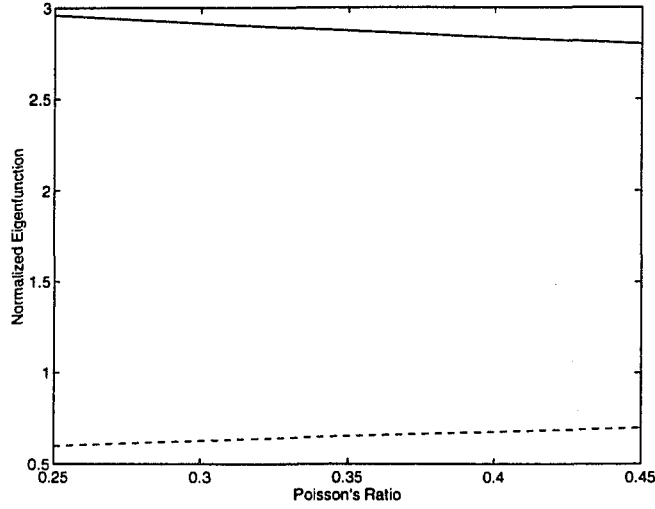


Figure 2.2: The value of the normalized eigenfunctions,  $\alpha$  (solid line) and  $\beta$  (dotted line), at the sphere surface, as functions of Poisson's ratio.

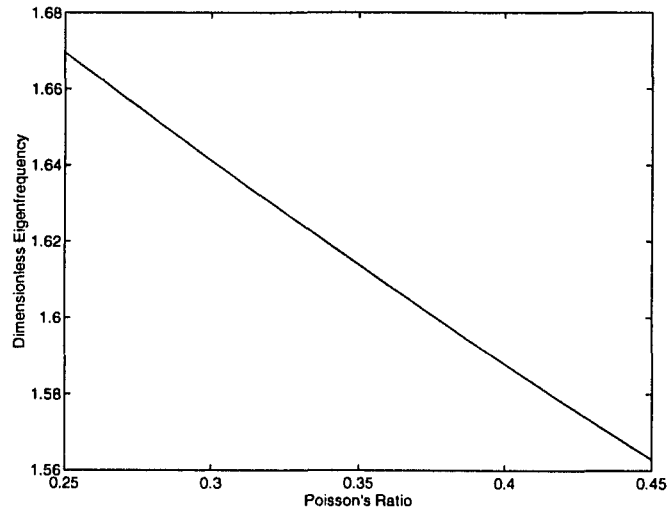


Figure 2.3: The dimensionless eigenfrequency of the uncoupled quadrupole modes of a sphere,  $\omega_o R \sqrt{\frac{\rho}{E}}$ , as a function of Poisson's ratio.

## 2.4 Sphere with Resonators

### 2.4.1 Equations of motion

We have just shown that measurement of the quadrupole modes of a sphere will provide information about all of the spatial dependence of the gravitational field, but a simple spherical resonator is not a practical detector. As mentioned in the introduction, one requirement for practicality is a set of secondary modes or mechanical resonators. All current bar antennas use resonators that interact only with the vector component of antenna motion normal to the surface on which they are mounted. Thus it seems natural to restrict our consideration to resonators of this type. The alternate possibility, interaction with transverse components of the antenna motion, is under consideration by others [20].

Designate the location of each resonator  $j$  by  $\mathbf{x}_j$ . Then the normal displacement,  $z_j$ , of the sphere surface under resonator  $j$ , is given by

$$z_j(t) = \hat{\mathbf{r}}_j \cdot \sum_m a_m(t) \Psi_m(\mathbf{x}_j). \quad (2.29)$$

By mechanical resonator we mean a small elastic system that has one of its own normal modes tuned to be resonant with the frequency of the antenna. The antenna surface motion excites this mode, and there is resonant transfer of momentum between the resonator and the antenna. Hence it acts as a resonant mechanical transformer, turning small motions of the large antenna

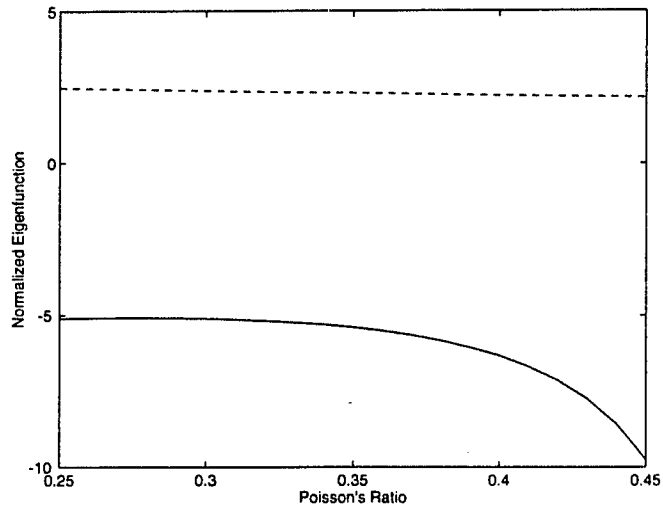


Figure 2.4: The normalized eigenfunction constants  $c$  (solid line) and  $d$  (dotted line) as functions of Poisson's ratio.

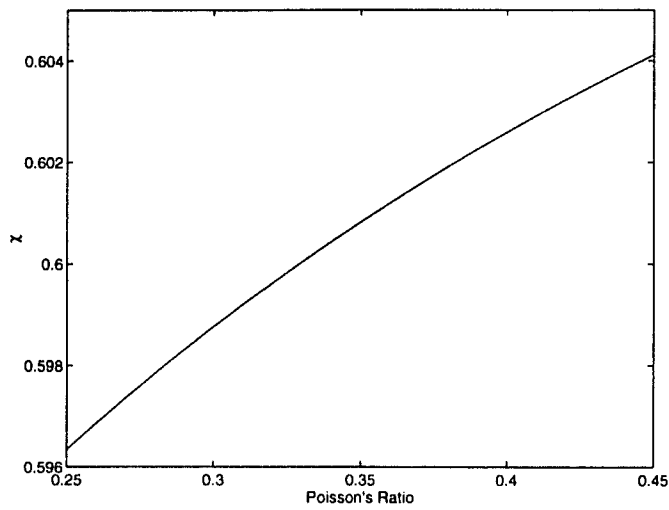


Figure 2.5: The fraction  $\chi$ , which determines the effective length of each sphere mode, as a function of Poisson's ratio.



into large motions of the small resonator. Each resonator  $j$  is constructed to obey a one-dimensional harmonic oscillator equation:

$$m_R [\ddot{q}_j(x_j, t) + \ddot{z}_j(x_j, t)] = -k_R q_j(x_j, t) + F_j^N(x_j, t). \quad (2.30)$$

The displacement of the resonator, relative to the sphere surface, is denoted by  $q_j$ . Because  $q_j$  is a relative displacement, the inertial displacement of the resonator mass is  $q_j + z_j$ , hence the peculiar form for the left hand side of the equation above. Each resonator is assumed identical, and the mass  $m_R$  and spring constant  $k_R$  of each are tuned to match the frequency of the five sphere modes so that  $k_R/m_R = \omega_o^2$ . Any random or noise forces that act between the small resonator and the sphere are included in  $F_j^N$ . A schematic of the one dimensional system is shown in Figure 2.6.

The values of the relative radial displacements of the sphere surface, at the resonator locations, can be grouped together into a “pattern vector” for a particular mode, because they describe the pattern of radial displacement for that mode. These column vectors in turn may be collected together to form a “pattern matrix”  $B_{mj}$  defined by

$$\hat{\mathbf{r}}_j \cdot \Psi_m(x_j) = \alpha B_{mj} \quad (2.31)$$

where  $\alpha = \alpha(R)$ , the value of the radial component of the eigenfunction at

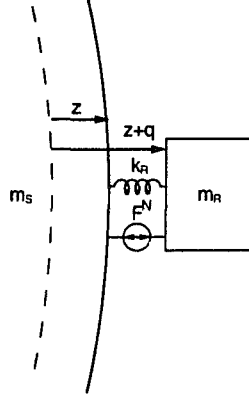


Figure 2.6: Schematic of a one-dimensional resonator attached to the surface of a sphere.

the surface. From equation (2.21) we find

$$B_{mj} = Y_m(\theta_j, \phi_j). \quad (2.32)$$

Because the wavefunctions are invariant to reflection through the origin, we may restrict the location of resonators to one hemisphere, without loss of generality.

Combining the above, we find the coupled equations of motion for the sphere modes are

$$m_S \ddot{a}_m(t) + k_S a_m(t) = \sum_j \alpha B_{mj} [k_R q_j(t) - F_j^N(t)] + F_m^S(t). \quad (2.33)$$

It is convenient to combine equations (2.30) and (2.33) into a matrix notation. We denote matrices by a double underscore and column vectors by a single underscore.

$$\begin{aligned}
 \begin{bmatrix} m_S \underline{\underline{I}} & \underline{\underline{0}} \\ m_R \alpha \underline{\underline{B}}^T & m_R \underline{\underline{I}} \end{bmatrix} \begin{bmatrix} \underline{\underline{\ddot{a}}}(t) \\ \underline{\underline{\ddot{q}}}(t) \end{bmatrix} + \begin{bmatrix} k_S \underline{\underline{I}} & -k_R \alpha \underline{\underline{B}} \\ \underline{\underline{0}} & k_R \underline{\underline{I}} \end{bmatrix} \begin{bmatrix} \underline{a}(t) \\ \underline{q}(t) \end{bmatrix} \\
 = \begin{bmatrix} \underline{\underline{I}} & -\alpha \underline{\underline{B}} \\ \underline{\underline{0}} & \underline{\underline{I}} \end{bmatrix} \begin{bmatrix} \underline{F}^S(t) \\ \underline{F}^N(t) \end{bmatrix} \quad (2.34)
 \end{aligned}$$

The vector  $\underline{a}$  has five components and the vector  $\underline{q}$  has one component for each resonator. The dimensions of the constant matrices can be inferred from these two column vectors.

These equations should give an excellent account of the mechanics of the system for arbitrary numbers and locations of resonators. They are restricted only by the previously stated assumptions: degeneracy for the uncoupled sphere modes and precise matching of the resonators. Most of the new features of a multimode spherical antenna are included, particularly the strong interactions between the sphere modes and the resonators. We have not included terms which represent the “dissipation” part of friction, which can be shown to be negligible for the sensitivity calculations we do here. We do include the “fluctuation” part of friction, within the random driving forces in  $\underline{F}^S$  and  $\underline{F}^N$ .

It is clear that these equations represent a set of elastically coupled harmonic oscillators with driving forces. The apparent peculiarities (off-diagonal terms in the mass matrix and asymmetry in the elastic matrix) are simply artifacts of use of the non-inertial coordinates  $q$ . In appendix A we show how to transform them into the canonical normal form, with normal coordinates  $\underline{\eta}$ :

$$\ddot{\underline{\eta}}(t) + \omega_o^2 \underline{\underline{D}} \underline{\eta}(t) = \underline{\underline{U}}^T \underline{\underline{K}} \underline{F}(t). \quad (2.35)$$

The sphere overlap integrals and the resonator noise forces are contained in the column vector  $\underline{F}$ .  $\underline{\underline{U}}^T$  is the transpose of a set of eigenvectors that diagonalize the equations. The matrix  $\underline{\underline{D}}$  is the diagonal matrix of eigenvalues for the normal modes described by  $\underline{\underline{U}}$ , and  $\underline{\underline{K}}$  is a constant transformation matrix. The equations of motion are now in a form that can easily be solved numerically using standard techniques.

To solve for the resonator displacements  $\underline{q}$  and sphere mode amplitudes  $\underline{a}$  we take the Fourier transform of equation (2.35), and solve for  $\underline{\eta}(\omega)$ . Once the normal coordinates have been found, the sphere mode amplitudes and resonator displacements are found by a constant transformation.

### 2.4.2 Truncated Icosahedral Arrangement

We can solve the equations above for arbitrary numbers and locations of small resonators, and determine whatever quantities are interesting, such as the coupled eigenfrequencies and eigenvectors. One important question is whether there exists any favored or optimum arrangement.

By a simple counting argument, we expect that a minimum of five resonators are required to completely measure the five quadrupole modes of the sphere, so our initial calculations considered the frequency structure with five resonators tuned to the frequency of the degenerate sphere modes.

The eigenmodes of the coupled system are naturally split up and down in frequency. From earlier work on optimizing a bar antenna coupled to a single resonator [26], we knew that the amount of frequency splitting was an indicator of the strength of the coupling, and normally would need to be adjusted to a particular value to optimize the overall signal to noise ratio. Therefore we were disappointed to discover that the 10 coupled modes did not split in an identical way. For every arrangement of five transducers that we tried, we found that the resulting coupled modes were arranged in singlets, doublets, and triplets, each with a different splitting from the original common frequency.

We then tried 6 resonators, and quickly discovered that there was an arrangement that greatly simplified the frequency structure: it became two degenerate quintuplets and a singlet. The geometric location of the resonators was found to be precisely the projection, onto the sphere, of the centers of half the faces of a concentric dodecahedron.

A Truncated Icosahedron (TI) has the same point group symmetries as a dodecahedron [27], but better approximates a sphere. It also has 32 flat surfaces suitable for mounting transducers, calibrators, balancing weights and suspension attachments. Therefore, we proposed to use 6 pentagonal faces of

a TI, instead of a dodecahedron, for arranging the mechanical resonators [14]. This shape, with the proposed resonator locations, is shown in Figure 2.7.

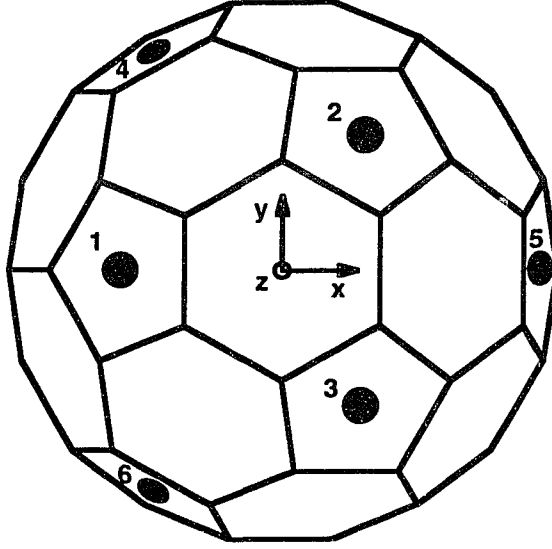


Figure 2.7: The truncated icosahedral gravitational wave antenna (TIGA) with secondary resonator locations indicated. The resonators lie at two polar angles,  $\theta = 37.3773^\circ$  and  $79.1876^\circ$ . Their azimuthal angles are multiples of  $60^\circ$ , as shown. The numbering on the resonators corresponds to the order used in the numerical simulation of section 2.4.5.

The high symmetry of the TI arrangement becomes apparent when you examine its pattern matrix. Each pattern vector is orthogonal to the others, and each has the same magnitude,  $\sqrt{\frac{3}{2\pi}}$ , or in other words:

$$\underline{\underline{B}}\underline{\underline{B}}^T = \frac{3}{2\pi}\underline{\underline{I}}. \quad (2.36)$$

This property causes the cross terms between sphere modes in the eigenfunctions to vanish, having the effect of isolating each sphere mode from the others. Without this, the energy from an excitation of a single sphere mode would end up “leaking” into the other sphere modes through the mechanical resonators. This allows us to use the sphere modes as a direct measurement of the gravitational spherical amplitudes.

In addition to the orthogonality, the sum of the components of each pattern vector vanishes, or

$$\underline{\underline{B}} \underline{1} = \underline{0}. \quad (2.37)$$

(The  $6 \times 1$  column vector  $\underline{1}$  is defined to have all elements equal to unity, while the  $5 \times 1$  column vector  $\underline{0}$  has all elements equal to zero.) This property will allow us to easily remove from our analysis the lone mode, which does not interact with a gravitational wave.

Since discovering this arrangement, we have not considered others in comparable detail. We have not attempted to make a proof that it is the optimum arrangement in terms of equal coupling to gravitational waves from any direction or polarization, but its symmetry leads us to conjecture that such a proof will be discovered.

### 2.4.3 Analytic Solution

The symmetry of the pattern matrix also suggested that there might be an analytic solution for the collection of eigenvectors  $\underline{\underline{U}}$  and the eigenvalue matrix  $\underline{\underline{D}}$  of equation (2.35). Examination of the numerical results suggested

a likely form for  $\underline{\underline{U}}$ , and substitution in the equations verified that it was a solution and determined the values of the constants. The details of this solution are found in appendix A.

It is convenient to divide the resulting set of eigenvectors,  $\underline{\underline{U}}$ , into three groups. The first two groups each contain five column eigenvectors and we denote them by  $\underline{\underline{U}}_+$  and  $\underline{\underline{U}}_-$ :

$$\underline{\underline{U}}_{\pm} = n_{\pm} \begin{bmatrix} \underline{\underline{I}} \\ c_{\pm} \underline{\underline{B}}^T \end{bmatrix}. \quad (2.38)$$

The physical interpretation of these is simple: each coupled eigenmode “mimics” the motion of one of the uncoupled sphere eigenmodes. In other words, each coupled resonator’s radial motion is proportional to the uncoupled sphere wavefunction at that resonator’s location. This amplified version of a mode’s pattern vector is either in-phase (down-shifted in frequency) or anti-phase (up-shifted in frequency). The frequency shifts are all identical, so that the quintuplet of degenerate bare sphere-modes has bifurcated into up-shifted and down-shifted degenerate quintuplets of modes. The amount of frequency shifting is given by the eigenvalues,  $\lambda_{\pm}$ , which are the diagonal elements of the matrix  $\underline{\underline{D}}$ . The identity matrix in the sphere components of the eigenvectors is an indication that energy will not be transferred from one sphere mode to another. The  $\pm$  notation has been used on the constants,  $n_{\pm}$  and  $c_{\pm}$ , as well to refer to the up (+) or down (−) shifting of the frequencies.



The remaining single eigenvector is

$$\underline{U}_o = \begin{bmatrix} 0 \\ n_o \underline{1} \end{bmatrix}. \quad (2.39)$$

This mode is at the original sphere frequency and does not interact with a gravitational wave. All the resonators move in unison and the sphere modes do not move at all.

The five dimensionless constants,  $n_{\pm}$ ,  $c_{\pm}$ , and  $n_o$ , can be determined using the Hermitian property of the transformation,  $\underline{\underline{U}}^T \underline{\underline{U}} = \underline{\underline{I}}$ . The symmetry properties of the pattern matrix, equations (2.36) and (2.37), play an important role here to simplify the work involved in determining these constants and in calculating the eigenvalues. We summarize the results:

$$n_{\pm}^2 = \frac{1}{1 + \frac{3}{2\pi} c_{\pm}^2}, \quad n_o^2 = \frac{1}{6}, \quad (2.40)$$

$$c_{\pm} = -\frac{1}{2} \left( b \pm \sqrt{b^2 + \frac{8\pi}{3}} \right), \quad (2.41)$$

$$\lambda_{\pm} = 1 + \frac{3}{4\pi} b \left( b \pm \sqrt{b^2 + \frac{8\pi}{3}} \right), \quad \lambda_o = 1, \quad (2.42)$$

where  $b \equiv \alpha \sqrt{m_R/m_S}$ . The relative splitting of the coupled modes is given by  $\Delta\omega/\omega_o = \sqrt{\lambda_+} - \sqrt{\lambda_-} \simeq 1.98 \sqrt{m_R/m_S}$  for a Poisson's ratio of 0.36.

### 2.4.4 Mode Channels

In an experiment, the measured quantities are the resonator amplitudes  $q_j(t)$ . Since they mimic the motion of the sphere, most of them are excited when only one sphere mode is excited. It would be helpful to have a direct way to determine the spherical amplitudes  $h_m(t)$ .

We have discovered that we can separate out each of the spherical amplitudes by forming fixed linear combinations of the measured amplitudes  $q_j(t)$ . We call these combinations “mode channels”, to indicate that each one is coupled only to a single mode amplitude,  $a_m(t)$ , of the uncoupled sphere, and hence to a single amplitude  $h_m(t)$  of the gravitational field. The linear combination desired for a given mode turns out to be the pattern vector for that mode. Therefore, if we denote the five desired outputs as a column vector  $\underline{g}$ , they are given by

$$\underline{g}(t) \equiv \underline{\underline{B}} \underline{q}(t). \quad (2.43)$$

The analytic solution of the complete system is most simply expressed in the frequency domain. Taking that solution from appendix A, and using equation (2.43), we find that each mode channel fourier amplitude  $g_m(\omega)$  is linearly related to the forces by equation (A.16), which is

$$g_m(\omega) = \sigma(\omega) F_m^S(\omega) + \sum_j H_{mj}(\omega) F_j^N(\omega). \quad (2.44)$$

The response function  $\sigma(\omega)$  is a scalar, so that each mode channel  $g_m(\omega)$  responds only to the corresponding spherical component  $F_m^S(\omega)$  and hence only to the corresponding gravitational component  $h_m(\omega)$ . In addition,  $\sigma(\omega)$  has the same frequency dependence as that of a bar-type antenna with one secondary resonator, so we can adopt familiar methods for parameter adjustment and time-series filtering.

In contrast, each mode channel responds to all the internal noise forces  $F_j^N(\omega)$ , via the matrix response function  $H_{mj}(\omega)$ . So the noise observed in one channel will be a superposition of the noises generated in all the resonators.

#### 2.4.5 Numerical Simulation of the TIGA system

The first major result of this chapter is that all the readout complications mentioned in the introduction are solved by using the mode channels. We illustrate this with a numerical simulation for two cases. We are only interested in demonstrating the mode channel concept, so we omit any noise terms from this simulation. For the first case, Figure 2.8 shows the response of the five sphere modes,  $\underline{a}$ , to the tidal force of a gravitational wave burst, which arrives at  $t = 0$ , propagating along the  $z$ -axis with  $h_x$  its only non-zero amplitude. The only non-zero force component is  $F_2$ , so only the  $a_2$  component of the sphere modes is excited. The special symmetry of the TI arrangement prevents transfer of excitation to the other sphere modes, so they remain unexcited.

The measurable quantities, the resonator displacements  $\underline{q}$ , are shown in Figure 2.9. To determine the sphere mode amplitudes from the observables,  $\underline{q}$ , we multiply by the pattern matrix to obtain the mode channels,  $\underline{g}$ . Figure 2.10 shows the result of this calculation. By comparing Figure 2.10 to Figure 2.8, it is obvious that (except for a phase shift of the envelope) the mode channels give a direct, one-to-one, readout of the sphere mode amplitudes, and thus of the gravitational wave.

For the second case, Figures 2.11, 2.12, and 2.13 show the results of the above calculation repeated for a gravitational wave burst propagating along the  $z$ -axis with amplitude  $h_+$ .

## 2.5 Spectral Sensitivity

We have found above a set of equations for the system and a method of solution. We can now apply them to predict the sensitivity of a model detector. First, we write down the response of each mode channel,  $g_m(\omega)$ , to the gravitational wave input  $h_m(\omega)$ . From equation (2.28) and (2.44)

$$g_m(\omega) = -\frac{1}{2}\omega^2 m_s \sigma(\omega) \chi R h_m(\omega). \quad (2.45)$$

Second, we model the noise sources, and calculate the system response to them. We have chosen to use a simple noise model which includes only two categories of noise certain to be important: (1) displacement noise, or random voltages in the electronic readout of the mechanical displacement

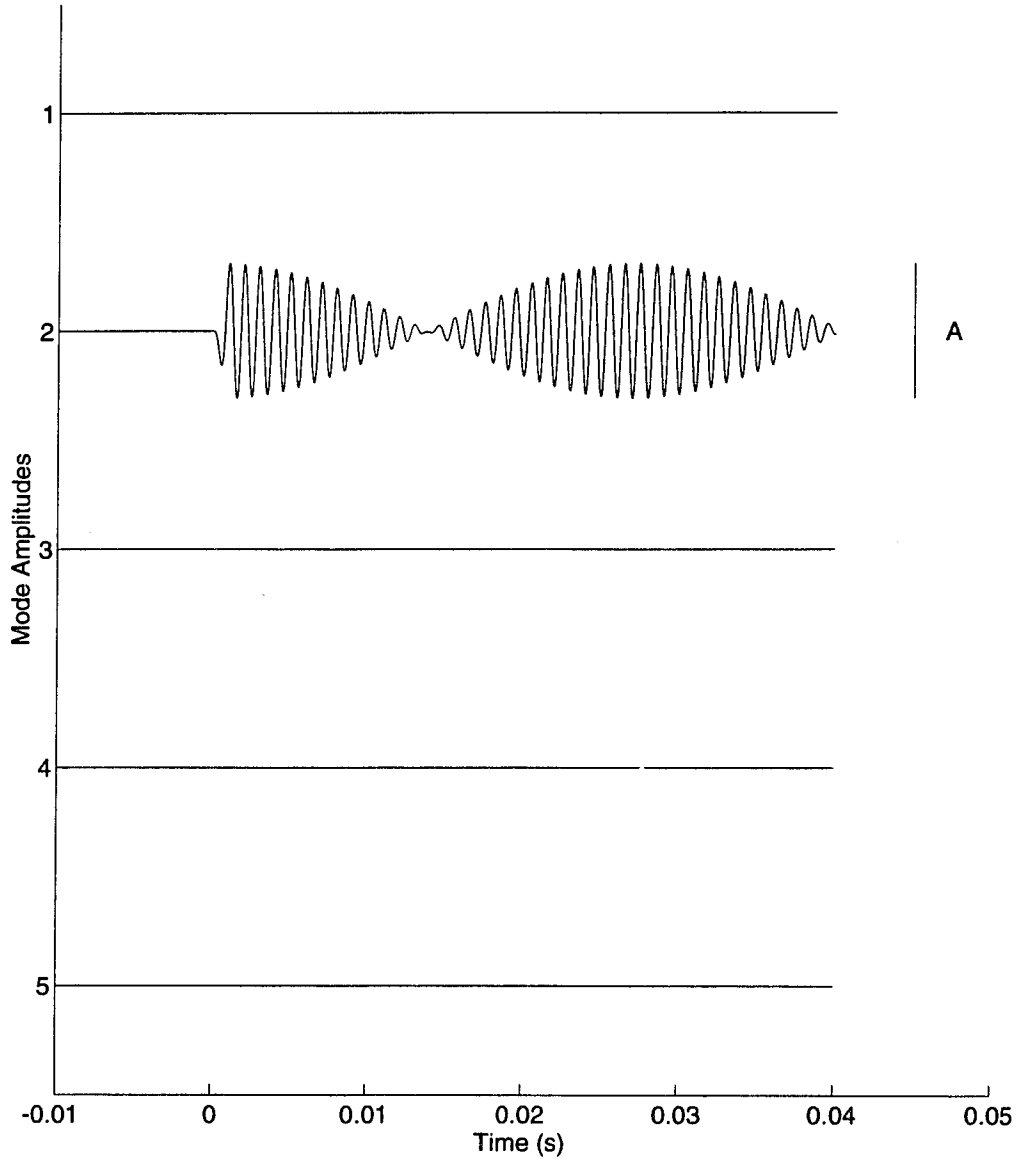


Figure 2.8: The response of the five sphere mode amplitudes,  $a$ , to the case of a gravitational wave burst of arbitrary size at  $t = 0$ , propagating along the  $z$ -axis with only non-zero amplitude  $h_x$ . The scale bar to the right indicates the maximum amplitude  $A$  of the sphere mode, for comparison with Figure 2.9.

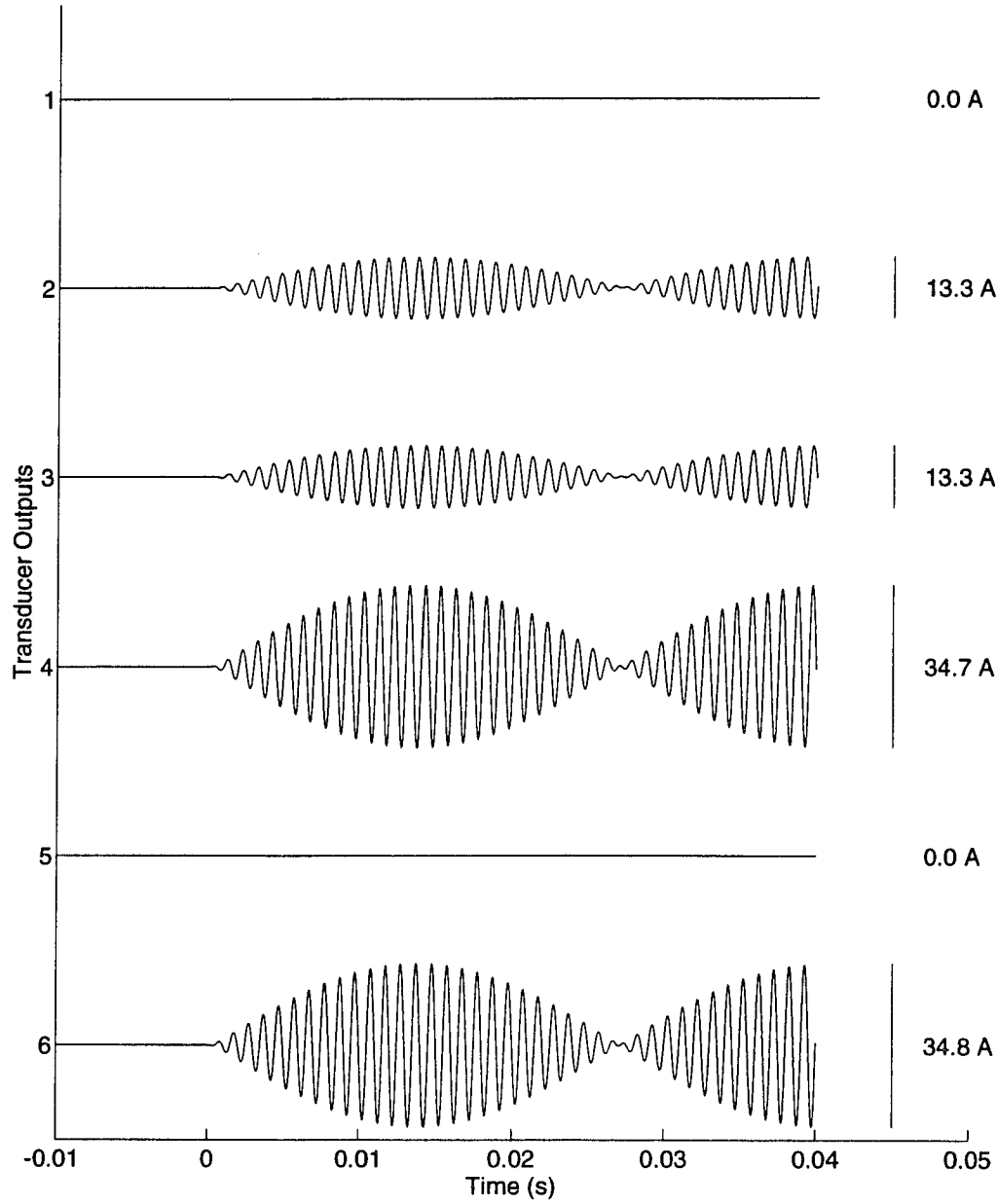


Figure 2.9: The resonator displacements  $q$ , due to the burst excitation of the first case. The scale bars to the right indicate the maximum displacement of each resonator, relative to the sphere amplitude  $A$  of Figure 2.8.

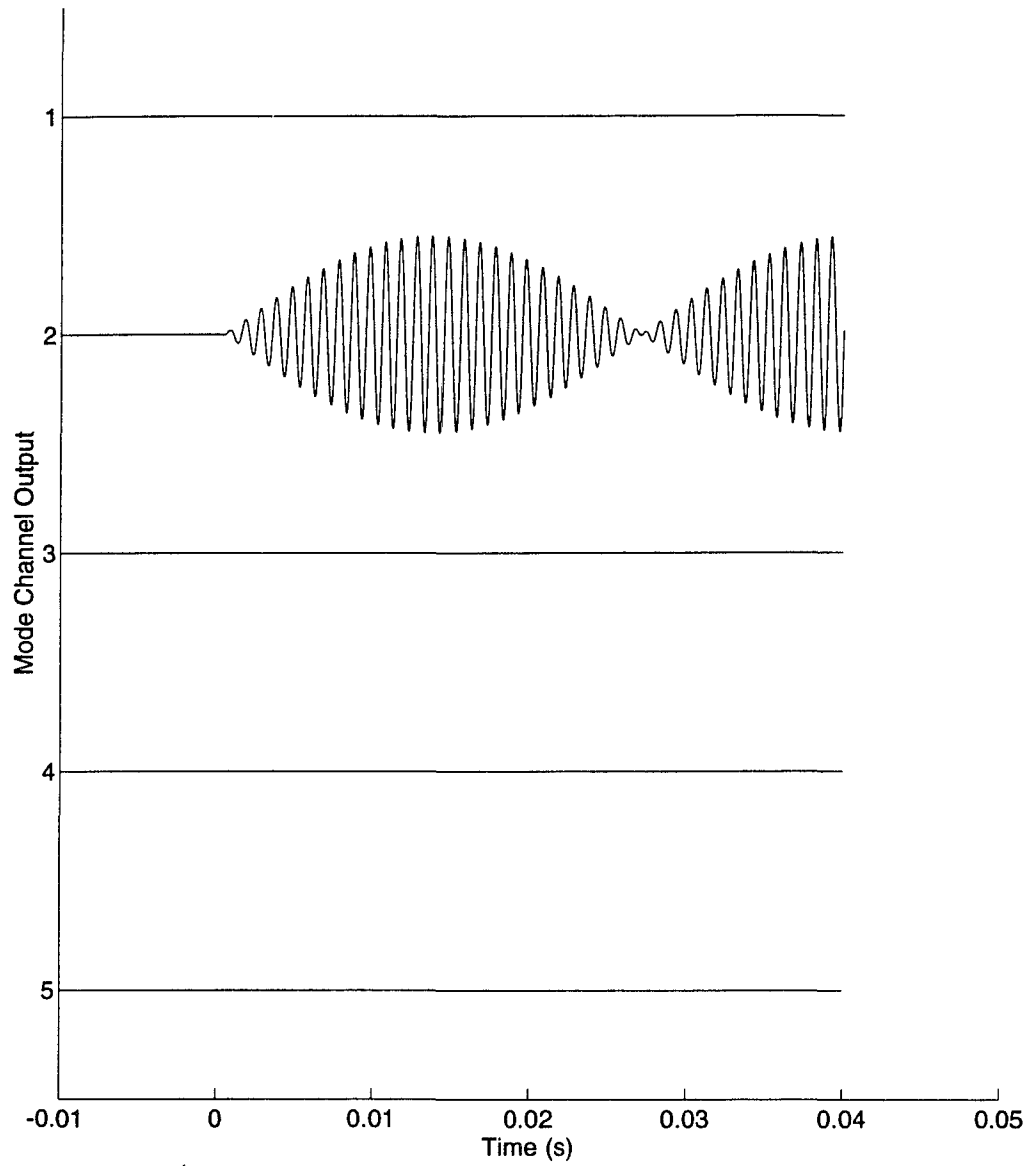


Figure 2.10: The mode channels  $\underline{g}$ , calculated from the resonator displacements of Figure 2.9 for the first case.

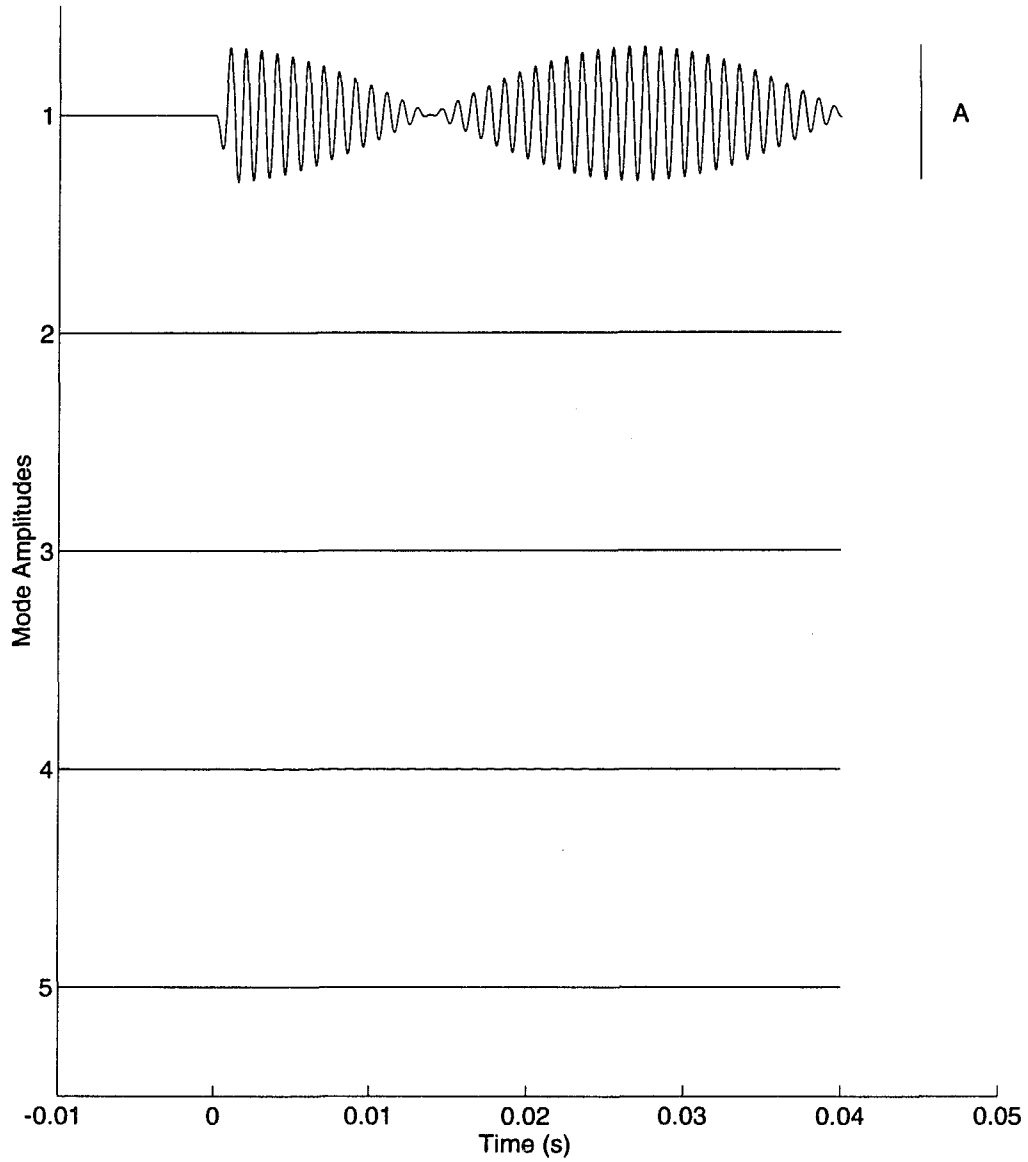


Figure 2.11: The response of the five sphere mode amplitudes  $\underline{a}$ , to the case of a gravitational wave burst of arbitrary size at  $t = 0$ , propagating along the  $z$ -axis with only non-zero amplitude  $h_+$ . The scale bar to the right indicates the maximum amplitude  $A$  of the sphere mode, for comparison with Figure 2.12.



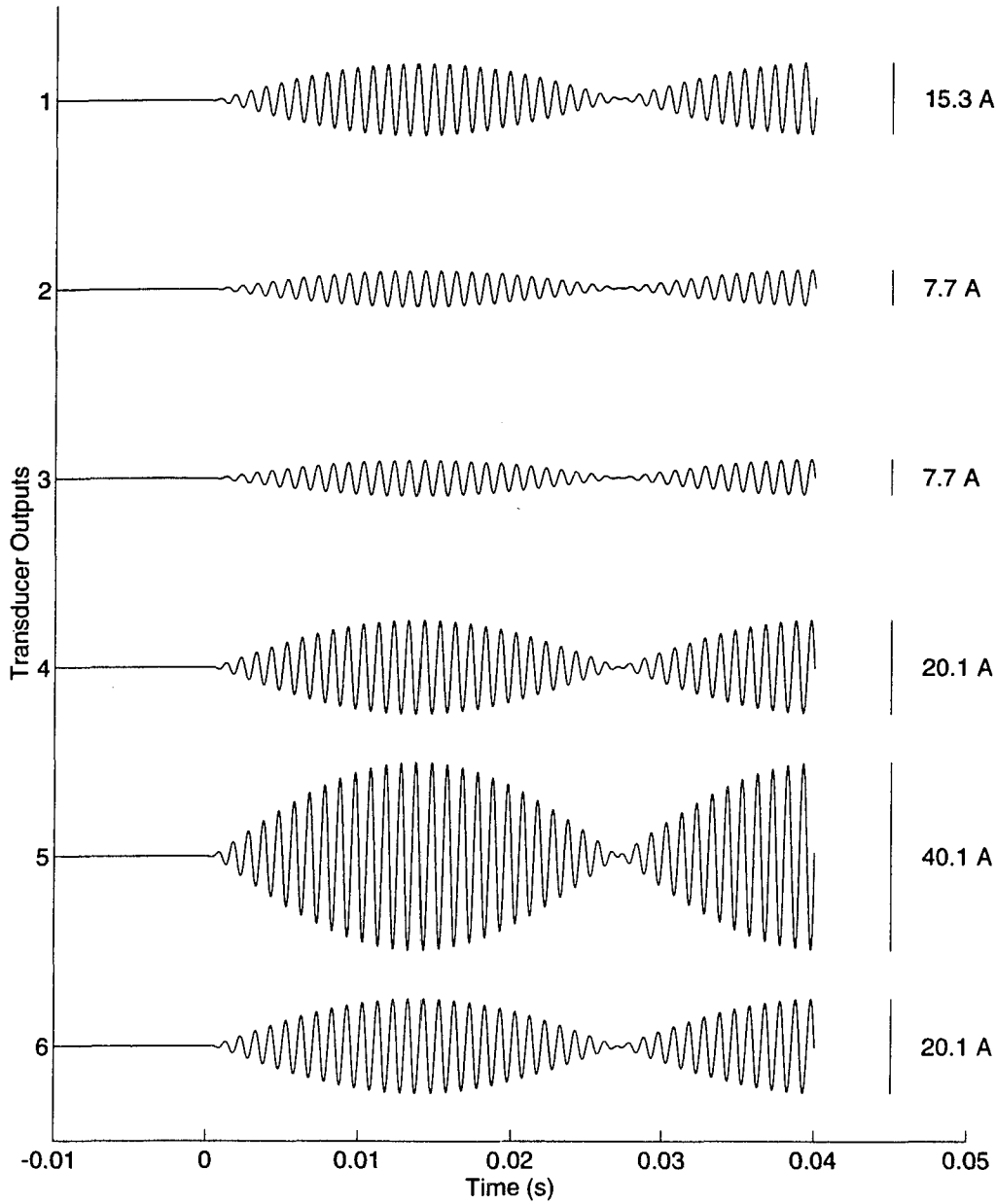


Figure 2.12: The resonator displacements  $q$ , due to the burst excitation of the second case. The scale bars to the right indicate the maximum displacement of each resonator, relative to the sphere amplitude  $A$  of Figure 2.11.

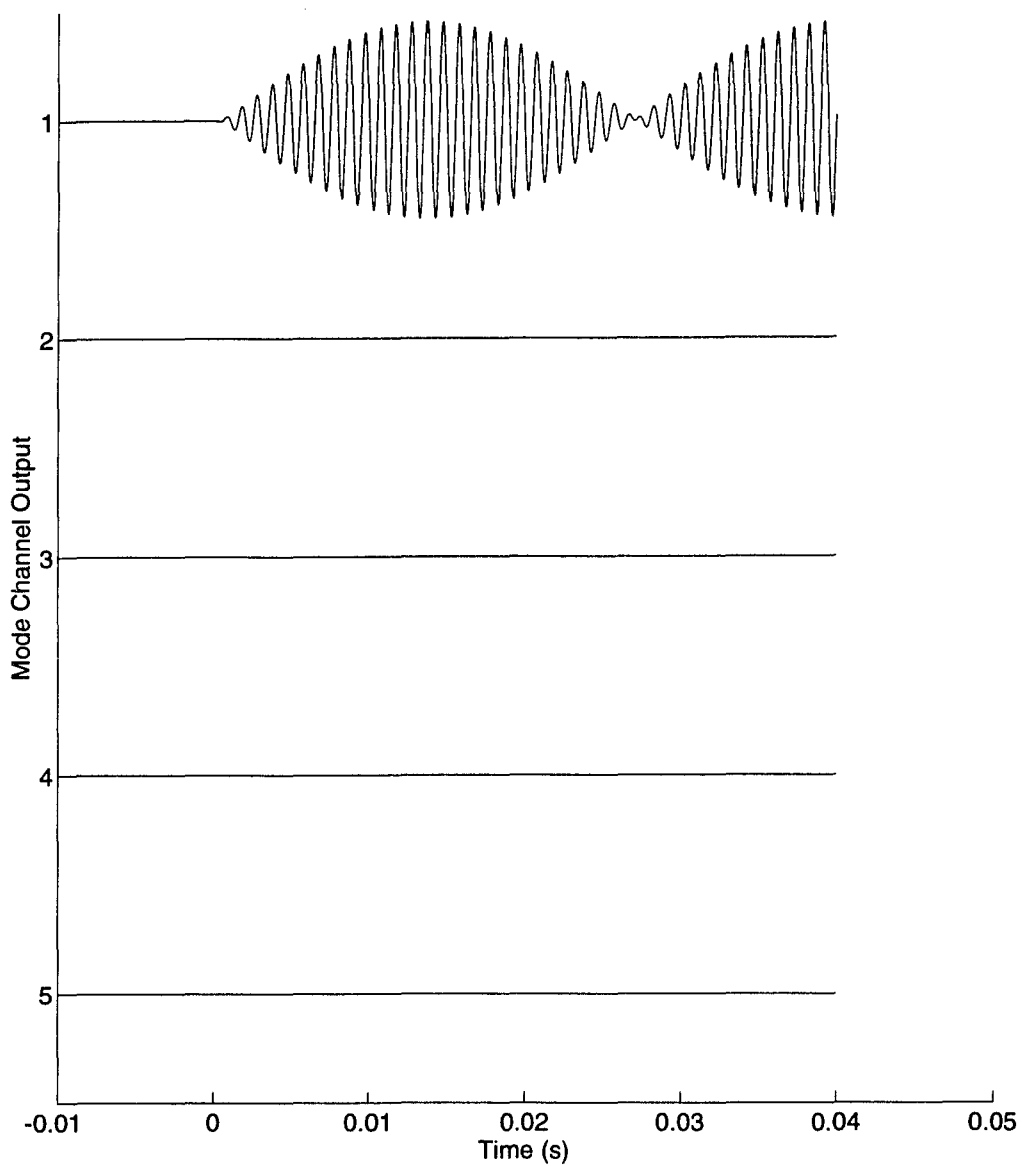


Figure 2.13: The mode channels  $\underline{g}$ , calculated from the resonator displacements of Figure 2.12 for the second case.

$\underline{q}$ , and (2) force noise, or random forces that actually excite the mechanical system. We assume both are generated in what Price [28] calls the “mechanical amplifiers”, or the transducer-amplifier combinations, which convert the resonator motions  $\underline{q}$  into an electronic readout. The displacement noise has a spectral density denoted by  $S^q(\omega)$ .

The force noise caused by the transducer-amplifier combination will appear as a random term in  $F_j^N(\omega)$ . We denote its spectral density as  $S^F(\omega)$ . We leave out of this model all of the Langevin noise forces that can be important with non-zero temperatures and non-zero mechanical losses. In other words, we are calculating the generalization, for a multimode multi-transducer antenna without mechanical losses, of the limit found by Giffard [29], who showed that the sensitivity of the detector is limited by the noise temperature of the amplifier.

These two noise sources can also be represented in a different way, by defining a “noise number” and a “noise resistance” for each transducer-amplifier. The noise number,  $N$ , is the amplifier noise temperature,  $T_n$ , referred to the quantum of energy at the antenna frequency,

$$N \equiv \frac{k_b T_n}{\hbar \omega} = \sqrt{\frac{S^F S^q}{\hbar^2}}. \quad (2.46)$$

The noise resistance is defined by

$$r_n \equiv \sqrt{\frac{S^F}{\omega^2 S^q}}. \quad (2.47)$$

It is a measure of the strength of the electro-mechanical coupling in the transducer-amplifier combination.

Combining the above, and transforming using equation (2.43) and the noise part of equation (2.44), we find that the calculated noise spectrum at mode channel  $g_m$  is

$$S_m^g(\omega) = S^F(\omega) \sum_j |H_{mj}(\omega)|^2 + S^q(\omega) \sum_j |B_{mj}|^2 \quad (2.48)$$

We assume the noise generators are all statistically independent.

Finally, we must compare the signal and noise responses, using some criterion for detectability. This final step can be done in a number of ways. For these calculations we have chosen to use a method not used before with resonant detectors, but now commonly used with laser interferometer gravitational wave detectors.

We calculate  $\tilde{h} = \sqrt{S_h}$ , the gravitational “strain spectrum” or “spectral sensitivity.” It is the square root of the total noise spectral density measured at the output, in this case  $g_m$ , referred back to the gravitational inputs  $h_m$ . It quantifies the fictitious gravitational background noise that would be required to mimic the stationary random output of the antenna. Assuming only stationary noise is present, it has the advantage of allowing comparison of different types of antennas. It also can be used to determine the signal-to-noise ratio for any specified signal waveform.

The noise spectral density of each mode channel  $g_m$ , referred back to the corresponding spherical component  $h_m$  is therefore

$$S_m^h(\omega) = \frac{4k_b T_n}{\omega^4 R^2 m_S^2 \chi^2} \frac{r_n \left| \frac{\beta_+}{\omega_+^2 - \omega^2} + \frac{\beta_-}{\omega_-^2 - \omega^2} \right|^2 + \frac{m_S m_R}{r_n \omega^2}}{\left| \frac{\alpha_+}{\omega_+^2 - \omega^2} + \frac{\alpha_-}{\omega_-^2 - \omega^2} \right|^2} \sum_j |B_{mj}|^2 \quad (2.49)$$

where  $\alpha_{\pm}$  and  $\beta_{\pm}$  are dimensionless constants found in appendix A.

From equation (2.49) we see that the calculated strain spectrum is proportional to the square root of the noise number. The shape of the strain noise is prescribed by the noise resistance,  $r_n$ , and the mode splitting. Figure 2.14 shows the strain noise for noise number,  $N = 1$ , for a 1 kHz Aluminum TIGA. The three solid lines are for different values of the noise resistance.

## 2.6 Comparison of the TIGA to other Detectors

It is possible to construct a number of TIGAs at different frequencies to create a “xylophone.” Doing so would enable one to partially determine the waveform of an incoming gravitational wave. The spectral density of a range of TIGA sizes is shown in Figure 2.15. The resonator to sphere mass ratio and noise resistance were adjusted to give consistent fractional bandwidth and a maximally flat curve. Parameters of this xylophone are shown in Table 2.1.

For comparison, the corresponding results for the equivalent bars, optimally oriented (bar axis orthogonal to an incoming wave), for the same strain

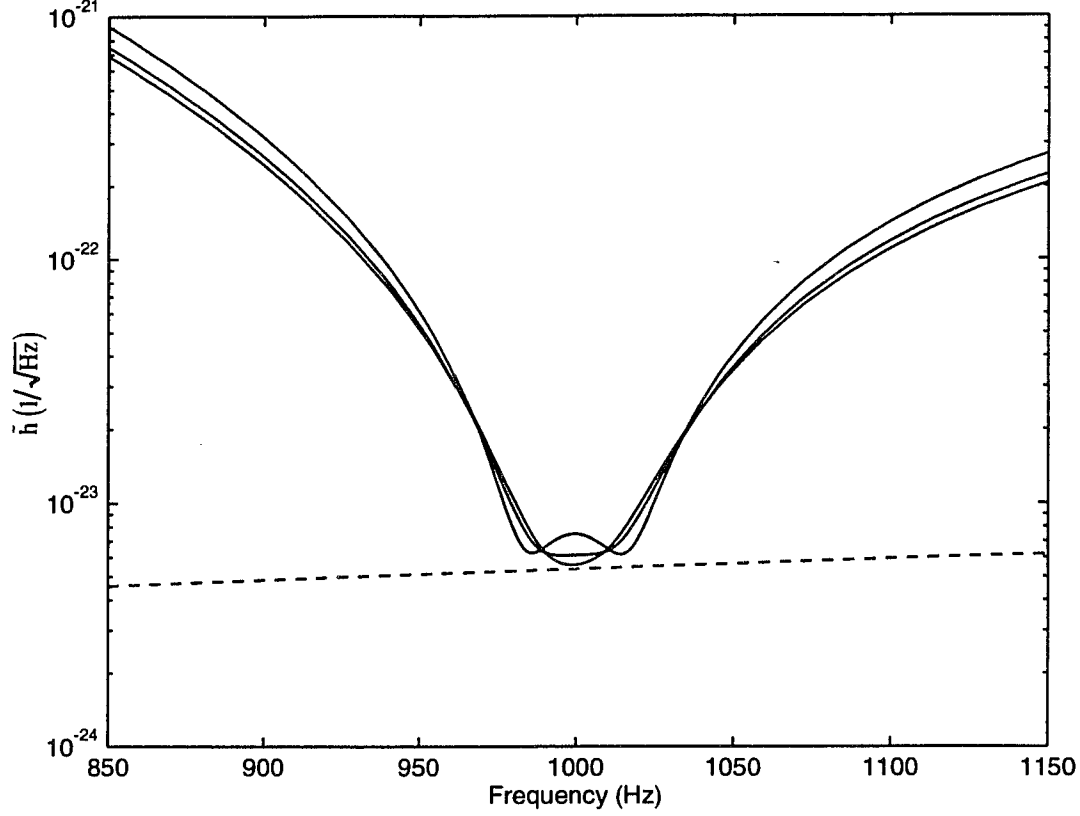


Figure 2.14: The strain noise spectrum  $\tilde{h}(\omega) = \sqrt{S_h}$  for a single mode channel of a 1 kHz Aluminum TIGA with noise number  $N = 1$ , for three different values of the noise resistance  $r_n$ . The dotted line is the additional noise due to the Langevin forces for an antenna at 50 mK with a mechanical quality factor of  $10^8$ .

Frequency (Hz)	Radius (m)	Sphere mass (kg)	Transducer mass (kg)
1000	1.30	25100	9.02
1250	1.04	12800	4.62
1500	0.87	7400	2.67
1750	0.74	4700	1.68
2000	0.65	3100	1.13

Table 2.1: Parameters for the “xylophone” of TIGA detectors shown as the solid lines in Figure 2.15. The material is aluminum.

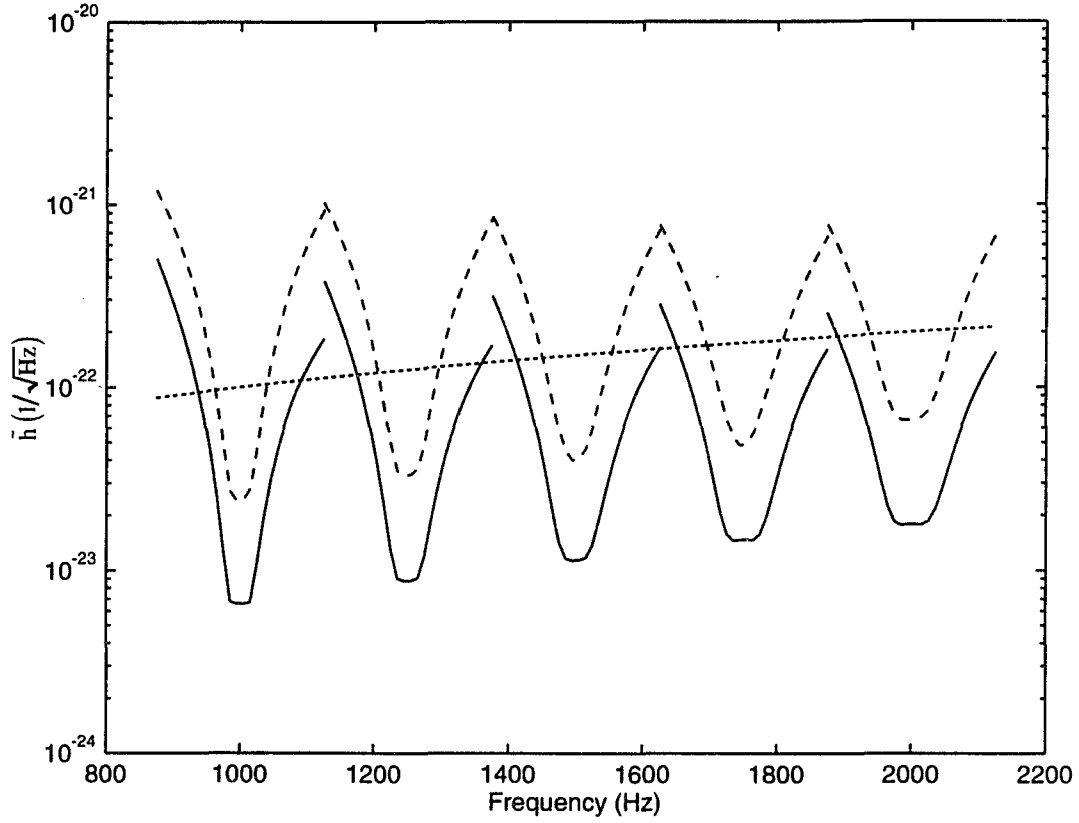


Figure 2.15: The calculated strain noise spectrum  $\tilde{h}(\omega) = \sqrt{S_h}$  for various detectors. The solid lines are a “xylophone” of TIGA detectors with quantum limited sensor noise, for a single channel (i.e., a single linear polarization arriving from an arbitrary direction). The dashed lines are a xylophone of equivalent bar antennas with quantum limited sensor noise, for the optimum orientation of the wave. The dotted line is the first generation LIGO detector, for the optimum orientation of the wave [30].

component are shown as dashed lines in Figure 2.15. The strain noise  $\tilde{h}^B$ , with  $N = 1$ , for the equivalent bar is larger by a factor of 3.9.

The second important result of this paper is that for equivalent conditions (equal noise numbers), a single channel of a TIGA will have  $3.9^2 = 15$  times better energy resolution than the optimally oriented equivalent bar. This is nearly the same improvement calculated by scaling up the mass of the bar by this amount, so we conclude that a single channel of the TIGA suffers no signal-to-noise penalty due to the various complications in the readout.

The comparisons in Figure 2.15 understate the overall advantage of the TIGA for the detection of gravitational waves. The five output channels combined make the detector optimally oriented for any polarization and incident direction. For a bar detector, it is well known that averaging over source direction and polarization [2] leads to a loss of energy resolution, compared to the optimum, by a factor of  $15/4 = 3.7$ . Thus the net result is that the angle-averaged energy resolution of the TIGA is  $3.7 \times 15 = 56$  times better than the equivalent bar detector (or about 7.5 times better in  $h$ ).

Also shown for comparison in Figure 2.15 (dotted line) is the predicted strain noise for the first generation LIGO detector [30] in its most favorable orientation for the same signal. It is evident that a xylophone of quantum limited TIGAs is significantly more sensitive over most of this frequency range, even without considering the extra information available about orientation. However, the predicted LIGO strain noise continues to drop, proportional to frequency, down to  $\sim 100$  Hz. We conclude that the two detector types are complimentary, each having a frequency domain where the predicted



sensitivities are superior. In addition to covering different frequencies, each uses a different technology, which is advantageous when confirming tentative detection of a gravitational wave.

By creating a xylophone of TIGAs, they are no longer limited to being narrow-band detectors. The “notes of the scale” can provide substantial spectral information about the detected wave. Coherent recording of the outputs will allow relative phase measurement, hence partial reconstruction of the time dependence of the waveform.

## 2.7 Extensions

Our noise model omitted the Langevin forces due to finite temperature and mechanical damping. In current practice, these are very significant. The inclusion of resonator damping will add a contribution to the random forces  $F_j^N$ , which will have the effect of increasing the noise number and the noise resistance so that their effect is immediately calculable via equation (2.49).

The inclusion of antenna damping will add noise terms to the effective forces,  $F_m^S$ , on the sphere modes. Because they act at the same point as the gravitational inputs, it is simple to calculate their spectral densities, referred to  $h_m$ . The single sided spectral density of the Langevin force is well known to be

$$S^Q = 4k_b T \frac{m_s \omega}{Q}, \quad (2.50)$$

where  $Q$  is the mechanical quality factor of the sphere,  $T$  is the physical

temperature, and  $k_b$  is the Boltzmann constant. Using equation (2.28), we refer this force to the gravitational input in Figure 2.14. The dashed line shows the noise for a TIGA with a  $Q = 10^8$  at 50 mK. Clearly if one can obtain a high enough  $Q$ , the noise in the system due to antenna damping can be ignored.

A natural extension of this work would be to calculate the effect of small departures from the perfect symmetry and perfect matching assumed here. We want to know if orthogonal mode channels can still be constructed, and also how much the sensitivity will degrade. Our experience with somewhat similar departures from perfect matching (such as the frequency mistuning of a resonator on a bar antenna) suggest that the sensitivity is affected only in second order by small departures of a parameter from its optimum value [31], but a quantitative calculation of these effects will be of practical interest for construction of such an antenna.

# Chapter 3

## TIGA Design

### 3.1 Finite element analysis

The theory contained in chapter 2 provides a solution to the elastic equations of a sphere. However, we propose using a truncated icosahedron as an approximation to a sphere. A TI has enough symmetry to ensure the degeneracy of the quadrupole modes, but to investigate how good of an approximation a TI is to a sphere we modeled it using finite element analysis.

Finite Element Analysis (FEA) is a numerical tool used to solve problems involving structural analysis, electromagnetics, heat transfer, fluid flow, etc. It involves dividing a system into smaller elements with known properties. Various boundary conditions can also be applied easily to the elements. Each element will interact with its neighbors in a specified fashion so that the behavior of the system as a whole can be described.

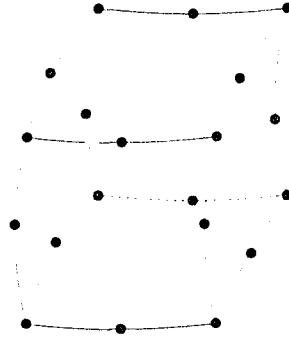


Figure 3.1: Linear 3-D 8- to 20-node isoparametric solid element

There are several commercial FEA software packages available; we used COSMOS/M [32]. It provides tools for solid modeling, mesh generation, static and dynamic analysis, and postprocessing features.

To form the volumes that make up a TI, we used a “connect the dot” approach. With the origin at the center of the TI, the coordinates of all the vertices and face centers of the polygons at the surface were calculated. By connecting all the points together, the surface of the TI is formed. These surfaces are then extruded to the center to form polygonal pyramids, which when put together form the volume of the TI.

The model was meshed using 8- to 20-node isoparametric solid elements, with 3 degrees of freedom per node. Shown in Figure 3.1, the solid element has nodes at all vertices and at positions between vertices to define the curve of the edges. Other shapes, such as a prism or pyramid, are formed with this element when more than one node is located at the same position. This type of element was found to give reliable results from experience with other models.

Free	Constrained	Description
2614	2614	Toroidal
2615	2615	Toroidal
2621	2621	Toroidal
2623	2623	Toroidal
2629	2629	Toroidal
3129	3129	Quadrupole
3129	3129	Quadrupole
3133	3133	Quadrupole
3134	3134	Quadrupole
3135	3135	Quadrupole

Table 3.1: Calculated eigenfrequencies for an aluminum truncated icosahedron, calculated with finite element analysis for two separate boundary conditions: no constraints and the center node constrained in all directions.

The analysis was performed for three separate boundary conditions: no constraints, center node constrained in all directions, and the center of three hexagonal faces constrained in all directions. Table 3.1 shows the important results of the three models. The difference in boundary conditions for each model resulted in only slight shifts in the frequencies of the quadrupole modes.

The frequencies of the quadrupole modes calculated from the FEA for the TI are equal to those calculated for a sphere, with diameter equal to 98.5% of the maximum diameter of the TI, using the elastic theory developed in chapter 2. The quadrupole modes of the FEA model are not exactly degenerate, but the frequency splitting is only 0.2%, which might be due to numerical effects.

## 3.2 Geometry and Design

We constructed a prototype TIGA to verify the theory and solve some of the practical problems that may exist in a real detector. The requirements for the prototype were that it be made of similar material to a real detector and be of practical size. The size must be large enough so that the quadrupole frequencies are close enough to a working TIGA so that the same electronics and filtering methods could be used. In addition, the prototype needed to be large enough so that attached resonators could be of the same type as those that will be used on a working TIGA.

The material for constructing the prototype came from a 34" diameter bar of Aluminum alloy 6063. This bar was previously used as a cylindrical gravitational wave detector, and was known to have good mechanical properties. To avoid using material close to the surface of the bar, the largest dimension on the prototype was set to 33".

A truncated icosahedron is a polyhedron with 32 total faces, 12 pentagons and 20 hexagons. It has 60 vertices, each with 3 edges meeting for a total of 90 edges. A TI has three defining dimensions: the two dihedral angles,  $138^{\circ} 11'$  (hexagon-hexagon) and  $142^{\circ} 37'$  (hexagon-pentagon), and the length of an edge. All other dimensions can be derived from these three using trigonometry (see appendix C). The prototype, with some important dimensions, is shown in Figure 3.2.

One advantage to using a truncated icosahedron is its high symmetry. As shown in Figure 3.3, the TI has 2-, 3-, and 5-fold symmetry. This high symmetry greatly simplifies both the design and machining of the prototype.

The prototype was designed for a center of mass suspension. It has a 1" diameter hole through the center of a hexagon face. Just above the center of the prototype the diameter of the hole increases to  $1\frac{1}{2}$ ". A rod with a wedge at one end was used to suspend the prototype from the area where the hole changes diameter. The wedge plugged the hole just above the center of mass so that balancing the prototype was relatively easy.

Three holes were also drilled and tapped in the center of the three hexagon faces adjacent to the top hexagon face (the face with the small suspension hole). Eyebolts were screwed into the holes whenever the prototype needed to be lifted or moved.

### 3.3 Prototype Machining

At first glance, the process for machining a TI is not straightforward, but a little further reflection on the high symmetry of the TI leads to a relatively easy method for cutting its faces. We include a description here to assist in developing the machining process for a large scale TIGA. The machining of the prototype was performed by FAMCO Enterprises, Inc [33].

The first step in machining the prototype was to cut the aluminum bar so that the length of the bar was precisely the caliper distance between two

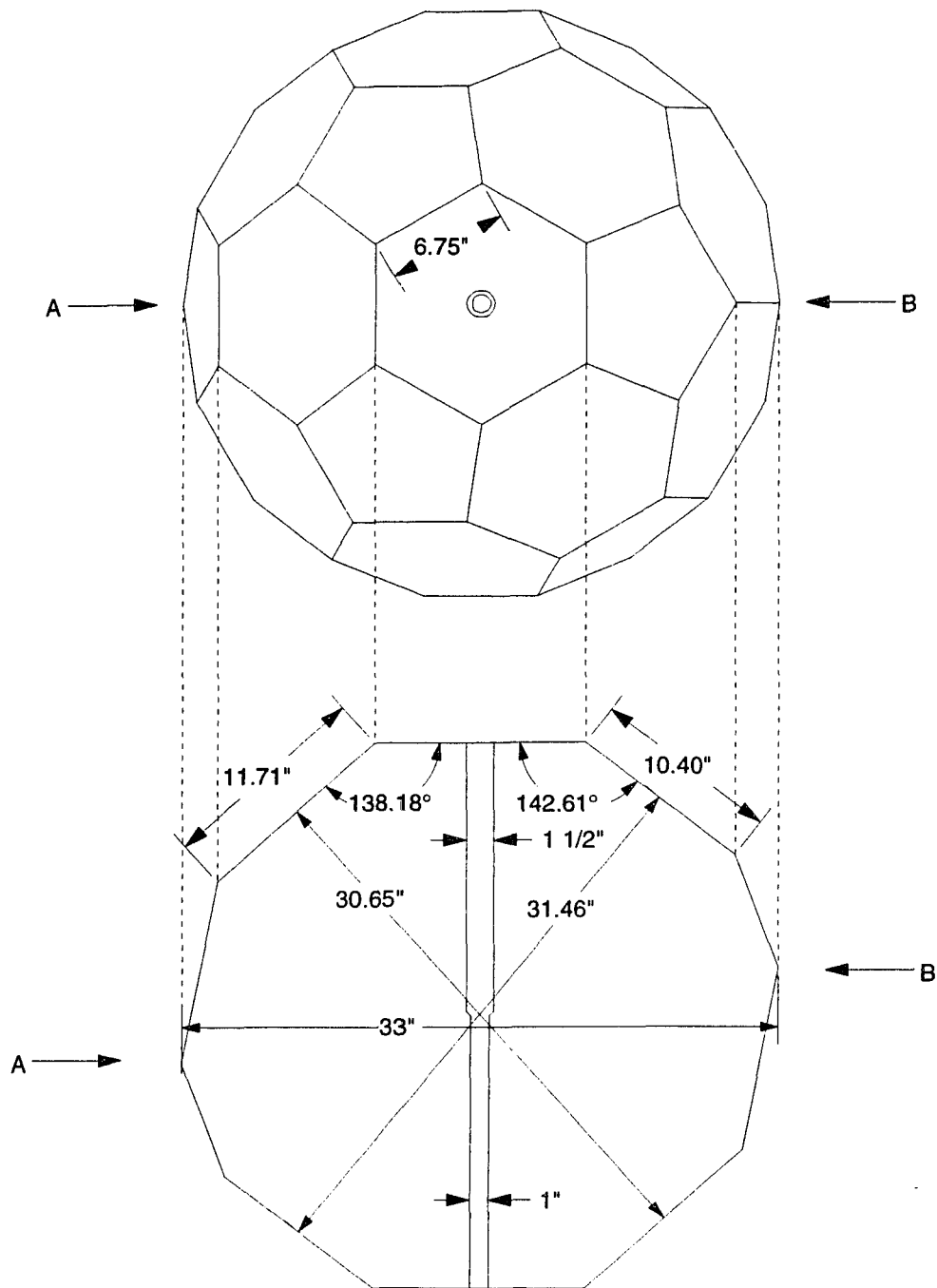


Figure 3.2: Schematic of the Truncated Icosahedron



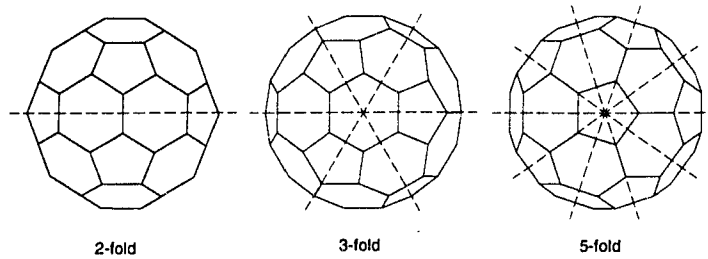


Figure 3.3: Symmetry of the Truncated Icosahedron

parallel pentagon faces (31.46"). Flanges were then bolted to these ends. The flanges were attached to a shaft so that the piece was free to rotate about the center of the two parallel pentagon faces (axis (a) in Figure 3.4). The shaft was held by a jig that sat on an indexed turntable. The jig was centered on the table so that it would rotate about the center of the piece (axis (b) in Figure 3.4). The turntable sat on a x-y table of a milling machine. The cutter could be moved vertically and in one horizontal direction.

To simplify the positioning of the piece for cutting we exploited the high symmetry of the truncated icosahedral shape. Only five rotations about axis (a) were necessary to machine all the faces. An index wheel, with five precise holes drilled into it, was attached to this axis to fix each angle of rotation. There were then three positions of the indexed turntable needed to machine the first half of the TI. The other half of the TI was then at positions reversed by 180°.

Once all the faces were machined, the suspension hole was made by first drilling a 1" diameter hole completely through the prototype through the center of a hexagon face. This hole was then redrilled half way through using

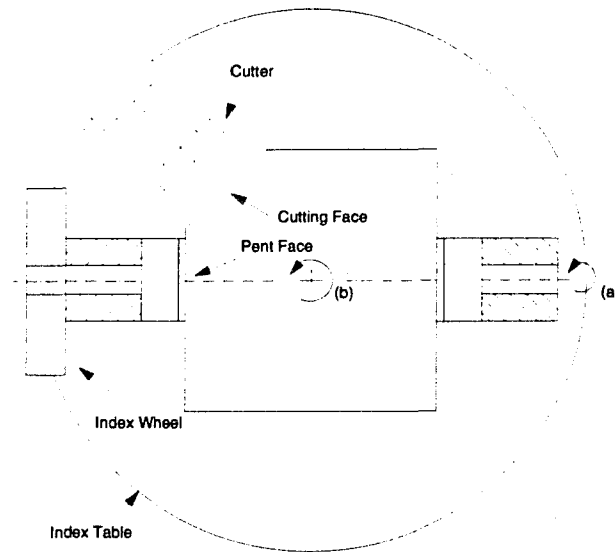


Figure 3.4: TI Machining frame, viewed from above.

the larger ( $1\frac{1}{2}$ " ) drill bit. To clean up the area where the hole expanded we used a special drill bit that was machined to match the angle of the suspension wedge.

### 3.4 Suspension

The prototype was suspended on a wedge at the end of a rod that clears the inside diameter of the large suspension hole, but plugs the small hole (Figure 3.5). The other end is threaded so that it can be screwed into a support table. For strength we made the suspension rod out of titanium.

The dimensions of the rod were set to give a large (greater than 10 times) safety factor. This compromises vibration isolation, but for early testing of

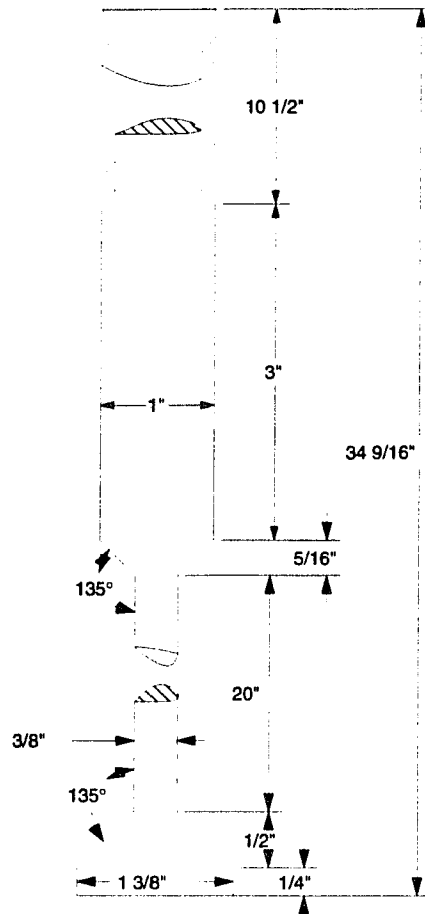


Figure 3.5: Titanium suspension rod

the TIGA, isolation is not important and the possibility of accidents may be greater because the TIGA needs to be moved often to change instruments. For future testing that requires better isolation, a thinner rod, one with more vertical compliance, can be used.

# Chapter 4

## The Uncoupled Prototype

### 4.1 Data Acquisition System

We began our study of the prototype by observing its behavior without any attached resonators. We attached small non-resonant accelerometers to its surface at the locations that the resonators would be positioned. For the initial observations we used a single channel spectrum analyzer to analyze the response of a single accelerometer. This method was very informative, but lacked the capability to observe multiple locations simultaneously. To overcome this we built a complete data acquisition system (DAS).

The data acquisition system that we used to test the prototype may end up being the system used on the final TIGA. The final system has more stringent requirements than a system sufficient to test the prototype, but to fully understand a working detector we felt it necessary to impose the

same requirements on the test system. Some of the requirements include: accurate timing, long term stability and reliability, capability of continuous acquisition over an indefinite amount of time, and ability to acquire data at a sampling rate fast enough to observe signals up to about 7000 Hz from at least six inputs. These requirements introduce difficulties that had not been addressed before in this laboratory. This section briefly describes the DAS we used and how it satisfied the above requirements.

The frequency of the quadrupole modes of the prototype are centered at 3235 Hz. If we were to sample this signal directly we would have to sample faster than the Nyquist frequency, 6470 Hz. With 6 transducer channels and a 16 bit A/D this results in a data rate of about 80 kB/s. This would fill a one Gigabyte disk in about three and a half hours. Obviously this becomes impractical very quickly.

To avoid this problem, we mixed the signal with a sine-wave reference, the frequency of which was close to the prototype's quadrupole mode frequencies, using a two phase lock-in amplifier. Both the in-phase and quadrature components of the mixed down output were recorded to preserve all the original information in the signal. If we placed our reference frequency 20 Hz away from the signal, then the minimum sampling rate was 40 Hz. The net effect was to lower the overall data rate by orders of magnitude.

When observing multiple signals, timing becomes important. We must make sure that the data is sampled at a precise rate and that each channel is

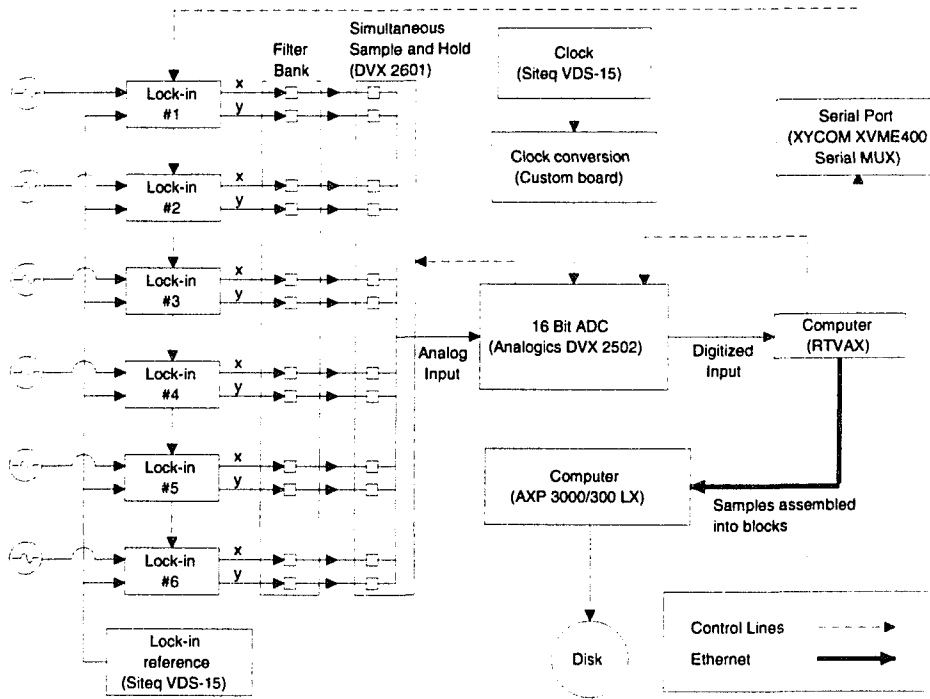


Figure 4.1: Block diagram of the prototypes data acquisition system.

sampled simultaneously. To ensure this we used a simultaneous Sample-and-Hold for each input channel. It sampled the analog signal from its channel simultaneously and held it until the A/D read the value. Each “strobe” was triggered by a precise external oscillator to ensure a fixed rate. See Figure 4.1 for a block diagram of the DAS.

A common problem with DAS’s is aliasing. Any frequency component in an analog input higher than the Nyquist frequency will appear in the data as a lower frequency signal. To avoid this, the *analog* signal must be low-pass filtered prior to digitizing. Lock-in amplifiers have built-in band-pass filters for the input and a low-pass filter for the mixed signal, but this is often

not enough. We found that an additional fourth order Butterworth low-pass filter, with a 600 Hz corner frequency, eliminated most of the aliasing problems.

To ensure the system was functioning properly, we put a known signal into it prior to collecting any data. A convenient test signal to use was a sine-wave with frequency close to the lock-in reference frequency. We call this a “sine-test.” We could then fit the acquired data to a sine-wave of frequency  $|\omega_r - \omega_s|$ , where  $\omega_r$  is the frequency of the lock-in reference and  $\omega_s$  is the frequency of the test sine-wave.

Both frequencies were not known exactly so we must first fit for the actual difference. This was done by minimizing the residuals between the data and a fitted sine-wave. The fit gave the amplitude and DC offset of the signal as well as the phase difference between the in-phase and quadrature. We also calculated the RMS of the residual of the data and the fit to determine the basic noise of the system. The results of a typical test are shown in Figures 4.2 and 4.3.

In performing the sine-tests we discovered a systematic difference between the individual lock-ins. The amplitudes of the in-phase and quadrature of each lock-in differs by a small amount. This results in a phase difference between lock-ins. Figure 4.4 shows the phase difference as a function of frequency. The phase changes with frequency because of the time-constant networks applied to the outputs of the phase sensitive detectors in the lock-ins. The only solution for this is to set the time-constants of the lock-ins as low as possible.

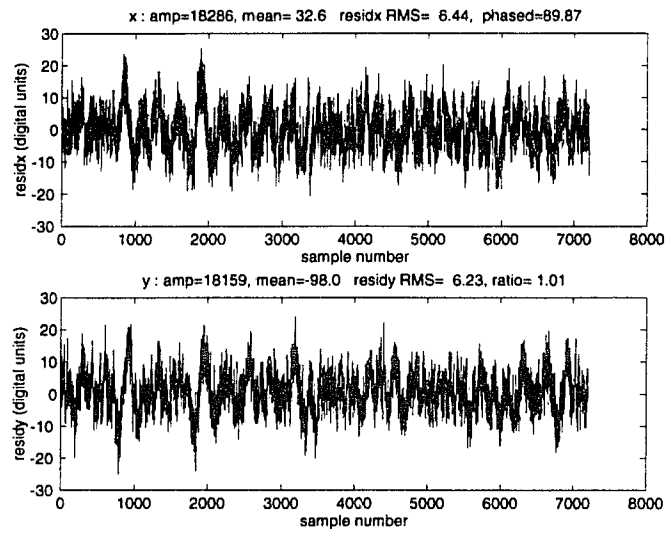


Figure 4.2: Residuals of a sine-test. Note that the residuals are  $\simeq 6/18000 = 0.03\%$ .

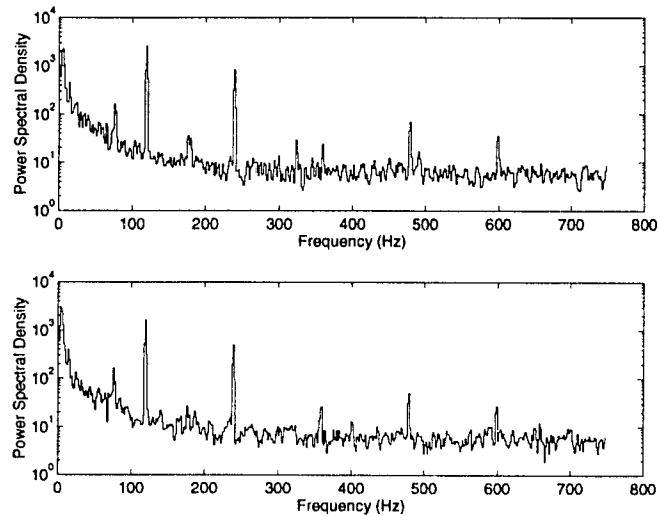


Figure 4.3: Power spectral density of the residuals of a sine-test



When putting the system together, it was important to test each component for noise sources, both individually and integrated with the entire system. The first place we looked for noise sources was in the VME crate. A number of grounding options were available. The DVX 2601 [34] has jumpers to select the input and output guard (shield) grounds. The input guards can be grounded to the chassis ground, the digital power supply ground from the VME backplane, the analog ground, or the digital-analog ground from the output of the DC/DC converter on the board. The output guards can be grounded to the analog ground or the digital-analog ground. The DVX 2502 also has a jumper to select the guard grounds. It can be grounded to digital ground (VME backplane ground), chassis ground, or analog ground.

Two tests were performed to determine the best configuration of the guard grounds. First, the inputs to the DVX 2601 were shorted and a sample of data was collected. The standard deviation and the minimum and maximum values of the data were useful measures of the level of noise left in the system. Second, a sine-test was performed for each configuration. The best configuration turned out to be analog grounding everywhere.

The lock-in amplifiers introduced most of the complexity to the system. The fact that the lock-ins we used were the most inexpensive we could find did not help matters. We used six EG&G PARC 5105 [35] dual phase lock-in amplifiers. They have no front-panel; they are controlled from the VAX via a RS232 port. We could use different settings for each individual lock-in, but in normal operation identical settings were used. We used a single oscillator for the reference of each lock-in.

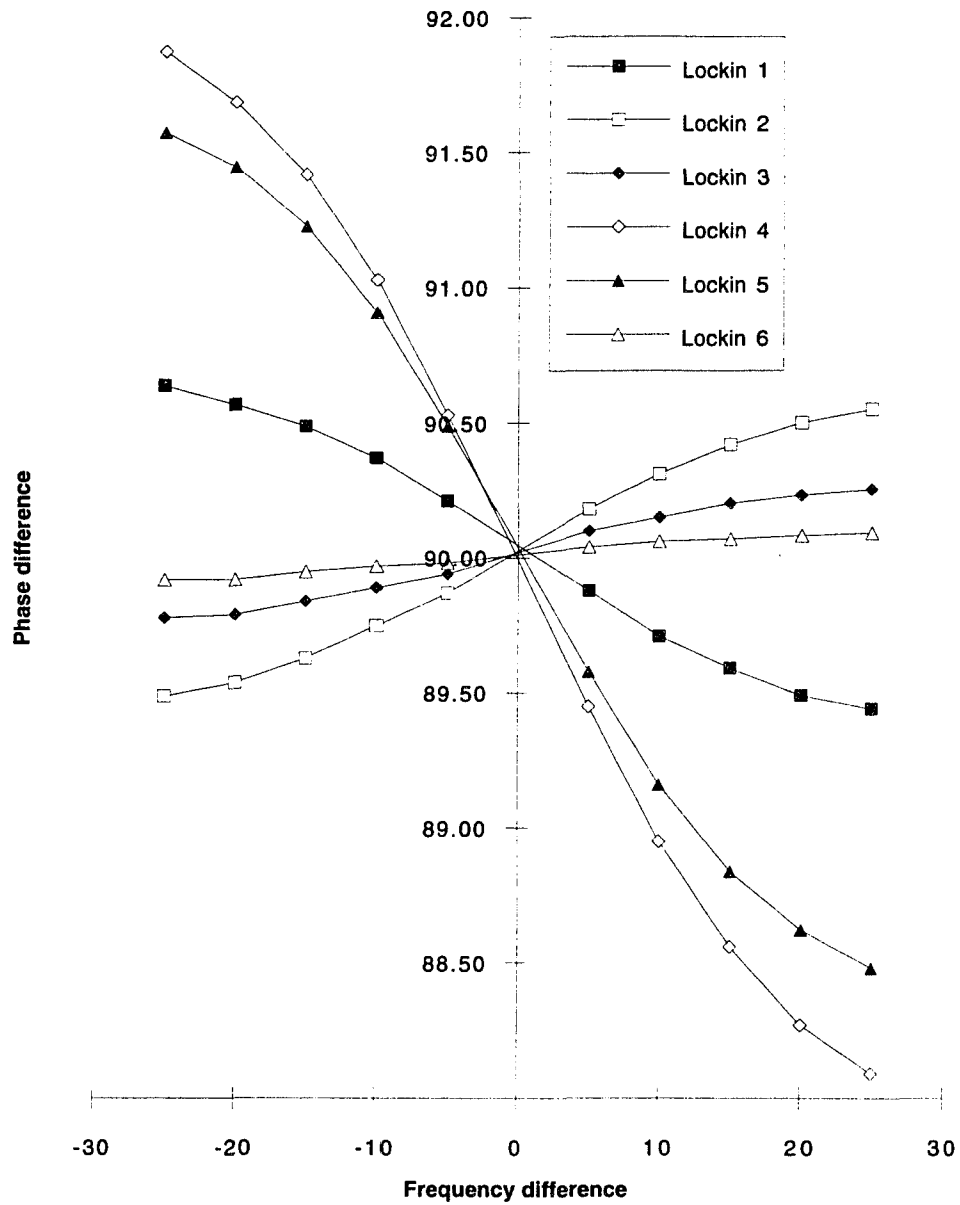


Figure 4.4: Phase difference between the in-phase and quadrature outputs of the lock-in detectors as a function of frequency.

Not much could be done to improve the lock-in's performance, but we did look carefully at the characteristics of each lock-in. For the first test, we shorted the input to a lock-in and looked at the noise spectral density on a dynamic signal analyzer. Next, we input random noise and again looked at the spectral density. This allowed us to measure the roll off of the signal due to the time-constant filter. Next we input a sine-wave from a signal generator. This test is closest to the actual experiment. One thing that was revealed by these tests is that harmonics of the signal, reference, and 60 Hz were not attenuated sufficiently by the internal filters of the lock-ins. The bank of low-pass butterworth filters between the lock-ins and the A/Ds mentioned above helped alleviate this problem. We also found that much of the 60 Hz harmonics were coming from "dirty" power supplied to the lock-ins. We were able to lower the noise coming from the lock-in significantly by R.F. filtering the A.C. power supplied to the lock-ins and the rest of the electronics.

## 4.2 Instrumentation

To measure the response of the prototype to an excitation, we used a PCB 353A quartz ICP (Integrated Circuit Piezoelectric) shear mode accelerometer [36]. The integrated circuit converts the high impedance charge signal from the quartz sensing element to a low impedance voltage signal. The voltage signal can then be fed into either a spectrum analyzer or into our DAS through a lock-in amplifier.

The PCB 353A has a frequency range of 1 to 7000 Hz with 5% sensitivity deviation and 0.7 to 10000 Hz with 10% sensitivity deviation. Each accelerometer has a mass of 10g and dimensions of  $12.7 \times 21.6$  mm. The accelerometers are screwed into a small base which is waxed onto the surface of the prototype.

We excited the prototype using a PCB 086 ICP impulse-force test hammer [36]. The hammer had a sensing element that transforms the instantaneous force into a voltage. The signal from the hammer was fed into the DAS to record the time of excitation and the size of the impulse.

The impulse force was measured to be roughly parabolic in shape and to last  $\sim 0.5$  ms. This made it easy to miss the maximum amplitude at the sampling rate appropriate for monitoring the sphere's response. To solve this problem we added an analog peak detector before the A/D. The peak detector holds the maximum voltage long enough to assure that the A/D will sample its output. The output signal then decays slowly until the peak detector is reset.

### 4.3 Uncoupled Antenna Spectrum

The spectrum of the prototype is shown in Figures 4.5 and 4.6 for a frequency range of 3000-7000 Hz. To obtain the full spectrum we had to excite the prototype several times with an impulse and change the reference on the lock-ins to be close to the peaks of interest. The data was then filtered and Fourier transformed digitally.

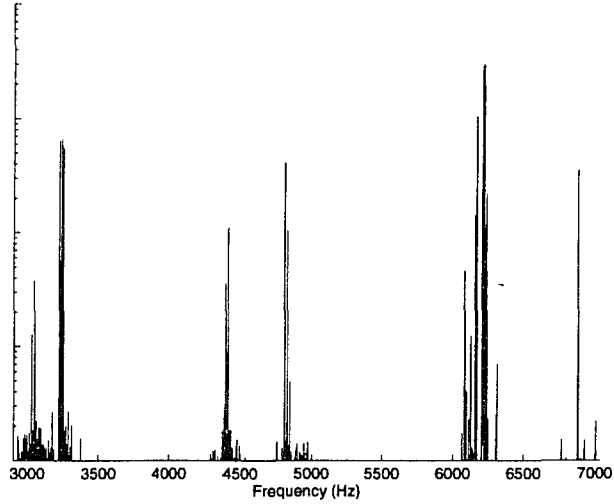


Figure 4.5: Power spectrum of the bare prototype showing most of the prominent modes below 7000 Hz.

Using the finite element model of the TI we were able to identify most of the modes, based on their frequencies. The most important peaks are the lowest quadrupole modes. As shown in Figure 4.7, they are not degenerate, but are grouped into two close doublets and a singlet. As will be shown later, the almost perfect doublet at  $\sim 3223$  is the  $Y_1$  and  $Y_2$  modes. The pair at  $\sim 3237$  is the  $Y_3$  and  $Y_4$  modes, and the singlet at  $\sim 3249$  is the  $Y_5$  mode. The doublets could only be seen as separate peaks by exciting the prototype at different locations.

Upon reflection, this mode splitting seemed to make good sense. The suspension hole through the prototype breaks the spherical symmetry. It does, however, maintain cylindrical symmetry about the  $z$  axis (the axis coaxial with the hole). With rotational symmetry about the  $z$  axis still intact,

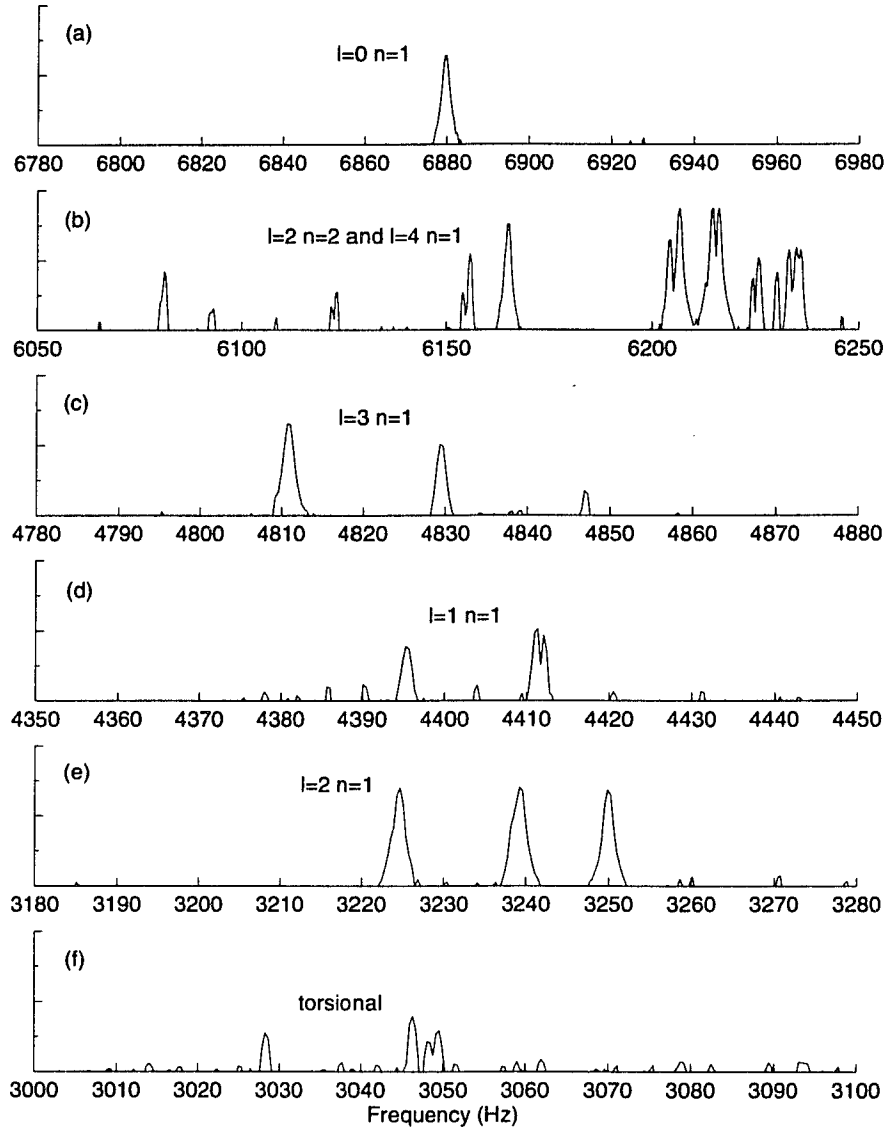


Figure 4.6: Power spectrum of the bare prototype, covering narrow frequency ranges near most of the prominent modes below 7000 Hz. Although most of the modes can be seen at this resolution, most of the larger peaks are nearly degenerate multiplets.

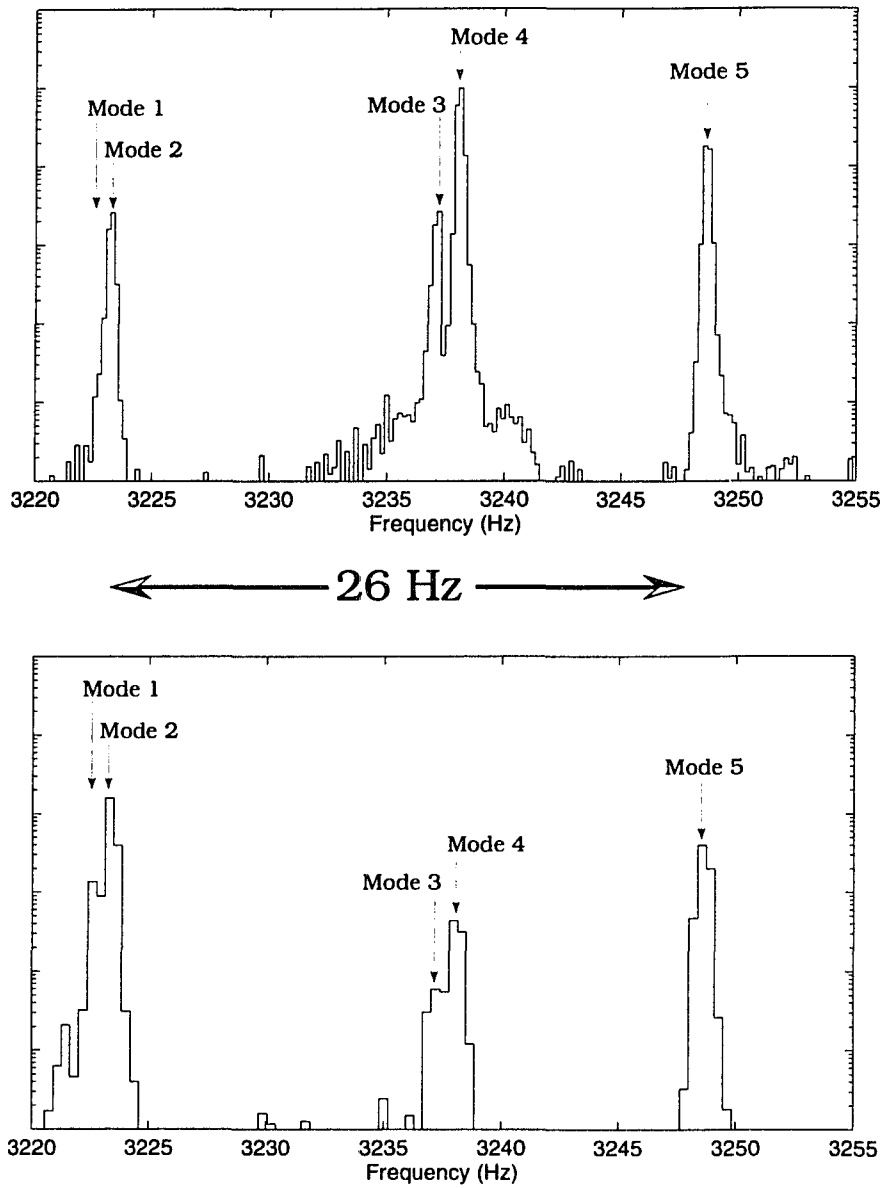


Figure 4.7: Power spectrum of the bare prototype's quadrupole modes from two separate impulse excitations at different locations

modes  $Y_1$  and  $Y_2$  form a degenerate doublet under that rotation. Likewise, modes  $Y_3$  and  $Y_4$  also form a degenerate doublet. Mode  $Y_5$  is invariant to this loss of symmetry so it is unaffected. The net result is that the suspension hole forces the  $z$  axis of the mode frame to be coaxial with it.

## 4.4 Accelerometer Calibration

While the absolute calibration of the accelerometers is not important for these tests, their relative calibration is important. One method to calibrate the accelerometers is to mount them on some type of resonator at locations that have the same amplitude of vibration for a particular mode. We tried mounting the accelerometers along a line on a prong of a tuning fork. It quickly became apparent that the response of the accelerometers strongly depended on how well the accelerometers were waxed to the fork. If an accelerometer was detached and reattached the calibration would change. To avoid this problem we needed a calibration method that could be done *in situ*.

The monopole mode of the TI (the  $\ell = 0$  mode, which for the prototype has a frequency of  $\sim 6880$  Hz) has a shape such that all locations at the same distance from the center will have the same radial acceleration. There are also no other modes in close vicinity to the monopole mode (see Figure 4.6). This makes it ideal for calibrating the system. We need only excite the monopole mode with all the accelerometers in their TI positions and observe their response simultaneously.



The results of an impulse test using the monopole mode worked very well. The response of each accelerometer was a clean, exponentially decaying sine-wave. The only major problem we encountered during this test was aliasing from other highly excited modes. We reduced this problem by increasing the time constant of the lock-ins to 3 ms. The results of one calibration are shown in Figure 4.8.

Figure 4.8 shows the impulse response of one accelerometer. Figure 4.8(a) shows the in-phase ( $x$ ) and quadrature ( $y$ ) outputs of the lock-in plotted against each other. If there is only a single decaying sine-wave, such a plot will be a spiral, as shown. Figure 4.8(a) includes some data from before the excitation; this is why there is an initial “jump” from very low amplitude to the large amplitude of the outermost circle. By following this jump one can get a quantitative idea, good to a few percent, of the initial phase of the mode when it was excited. This is useful to show that all the accelerometers are in-phase as expected.

Figure 4.8(b) shows the magnitude of the sine-wave,  $\sqrt{x^2 + y^2}$ . It is plotted on a logarithmic scale, so that a fit to the slope of this line measures the quality factor,  $Q$ , of that mode. This method also lets us extrapolate to find the initial amplitude of the mode, which can then be used to compare with the outputs of the other accelerometers. In air, the  $Q$  of the monopole mode was found to be approximately 31,000.

Figure 4.8(c) shows the spectral density for the monopole mode. The monopole mode is not close to any other modes which makes it very convenient for calibration. This type of plot is useful, not only to measure the

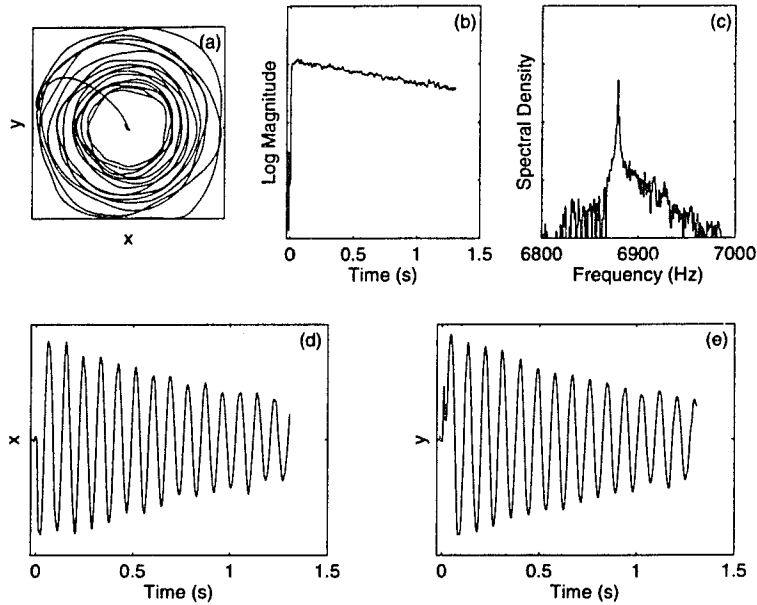


Figure 4.8: A typical calibration of the accelerometers using the prototype's monopole mode.

frequency of a mode, but also to check that there are no aliases or unexpected noise sources sneaking into the data.

Figures 4.8(d) and 4.8(e) show the in-phase and quadrature outputs of the accelerometer plotted separately. Both show a very clean decaying sine-wave. It also shows that there is no phase deviation over time of the instrumentation.

Once a fit to an exponentially decaying sine-wave is calculated, we know each accelerometer's amplitude relative to the other outputs. We can then use this ratio to correct the data for other tests. This method is very convenient, because the only change needed for other types of impulse testing is to change the reference frequency of the lock-ins; the accelerometers do not have to be removed or remounted.

One peculiarity we found remains unexplained: the output of the different accelerometers was not strictly identical during the first 30 ms. Only one accelerometer, the one directly opposite to the hammer blow, had a transient feature that did not appear in the other accelerometers. That transient is shown in Figure 4.9 for a typical data set. It is perhaps due to the initial shock wave from the impulse striking the opposite face before it is distributed throughout the body. The transient was not a problem for calibration, so we left its explanation to some future investigation.

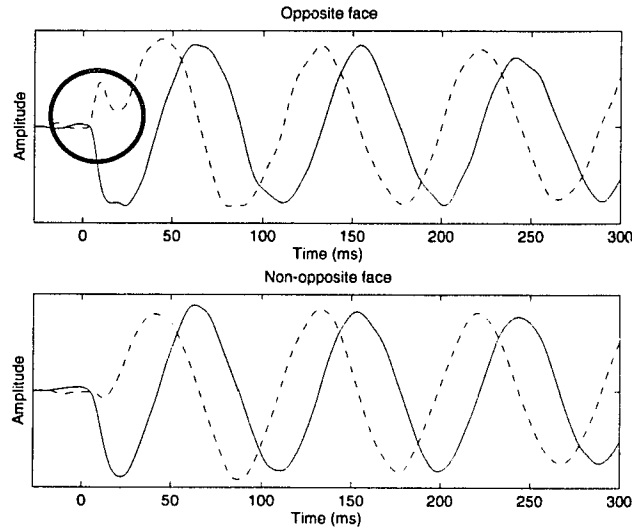


Figure 4.9: The first 350 ms of response of the monopole mode to an impulse. The solid lines are the in-phase outputs of the lock-ins, and the dashed lines are the quadrature outputs. The initial transient mentioned in the text is circled.

## 4.5 Mode Shape Analysis Methods

The next step in testing the prototype was to measure the response at the surface to an excitation of the quadrupole modes. This allowed us to identify each mode with a corresponding spherical harmonic. We developed and

tested several methods for doing this. In this section we briefly describe some of these methods.

One possible approach is to excite each mode individually from different positions on the prototype and measure the response at various locations. This can be accomplished by driving the prototype with a sine-wave. We did a feasibility test with a “home-made” shaker, made from a piezoelectric speaker element, to determine if it was possible to excite each mode individually. The near degeneracy of the modes in the two doublets made it too difficult to excite each mode individually; therefore, we rejected this method. We were able to lift the degeneracy of the modes by attaching masses to the surface of the prototype, but we decided against pursuing this method further because it might also change the shapes of the modes.

A second method is to excite prototype with an impulse from a hammer. This will excite all the quadrupole modes of the prototype. Their response will depend on the location and direction of the impulse, the type of tip used on the hammer, and the strength of the impulse. We developed several methods for analyzing the response of the accelerometers which we describe below.

We began by analyzing the response in the frequency domain. We attempted to fit the frequency response to five decaying harmonic oscillators. This involved fitting for 4 parameters (frequency, decay constant, initial amplitude, and a time shift) for each of the five modes. The near degeneracy of the two close doublets made accurate fitting impossible. Also, 20 parameters was too many for the fitting routines used, so we abandoned this method.

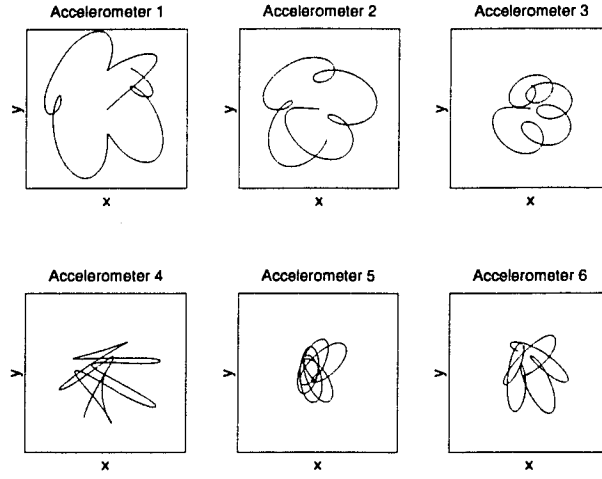


Figure 4.10: In-phase ( $x$ ) and quadrature ( $y$ ) response of the accelerometers plotted against each other for an impulse excitation.

The next analysis method we attempted was to look at the direct response of the accelerometers in the time domain. Figures 4.10 and 4.11 show a typical data set of each accelerometer's response using the plotting method described in section 4.4. The beating of the modes, because of their non-degeneracy, made an accurate measurement of the response in the transducer frame difficult.

The method we ended up using was to transform the outputs of the accelerometers to mode channels in a way similar to that discussed in section 2.4.4. The transformation was a linear combination of the outputs of the accelerometers. By minimizing the beating between modes, the transformation could be optimized to separate the modes from each other into channels. The initial response of the modes to an impulse could then be

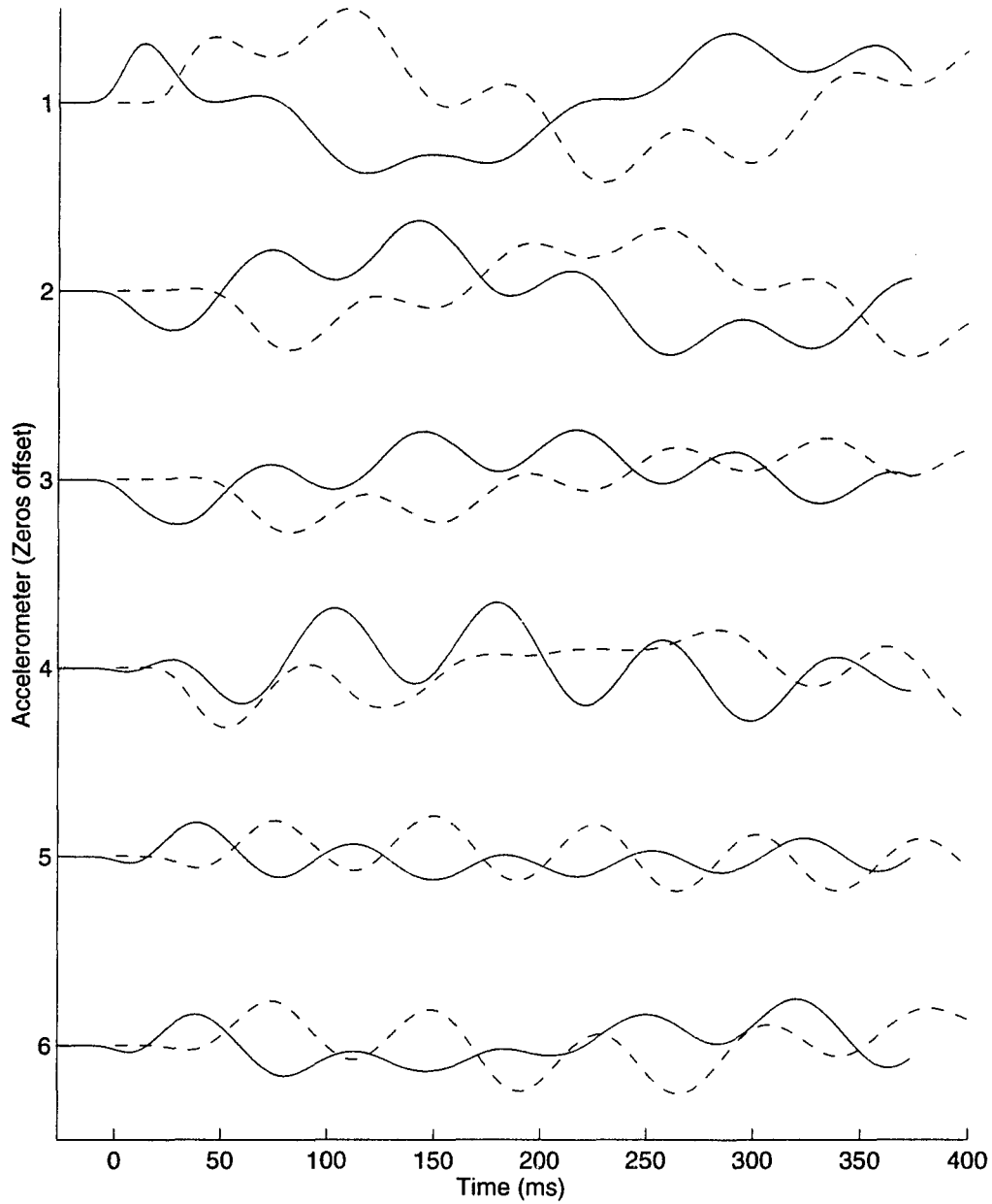


Figure 4.11: In-phase (solid lines) and quadrature (dashed lines) response of the accelerometers for an impulse excitation applied at time  $t = 0$ . This is the same data set shown in Figure 4.10, but plotted as a function of time.

interpolated by analyzing the mode channels, which were now in the form of a single exponentially decaying sine-wave. The techniques used to perform this analysis are discussed in greater detail in the following section.

## 4.6 Separation into Mode Channels

To transform the accelerometer data to mode channels we needed to determine the real pattern matrix for our imperfect “sphere.” We began by guessing a pattern matrix oriented in a lab coordinate system with the origin at the center of the prototype, z axis coaxial with the suspension hole (vertical), and a horizontal xy-plane with the x-axis in the direction of pentagon face 5 in Figure 2.7. Because of the retention of cylindrical symmetry, there was no compelling reason why the modes would choose this orientation of the x and y axes, but it seemed like a reasonable place to start.

The results were astonishingly good. Each mode channel resembled a relatively clean sine-wave. However, the magnitudes of the sine-waves did not follow a simple exponential decay. As shown in Figure 4.12, some of the magnitudes oscillated as they decayed. This indicated that the pattern matrix was off by some small amount. The oscillations also seemed to be grouped into two pairs of mode channels. We inferred from this that the pattern matrix needed to be rotated so that the modes mixed would be 1 with 2, 3 with 4, and 5 with all.

It is not convenient to change the lab-frame, so we chose to rotate the mode-frame relative to the fixed lab-frame. This was done by rotating the

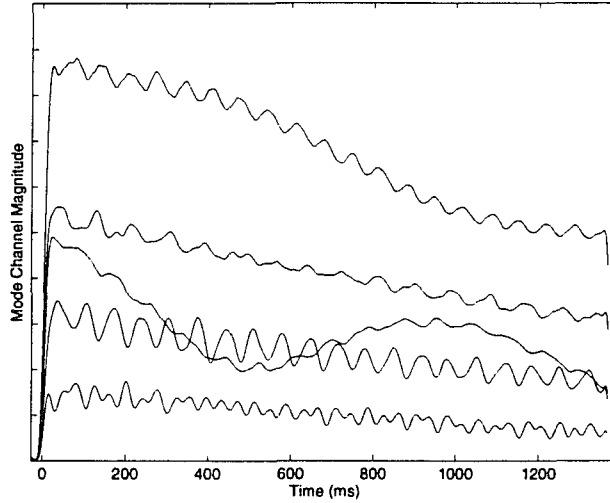


Figure 4.12: Magnitude of the mode channels calculated using the unrotated pattern matrix. The low frequency beating is due to mixing between nearly degenerate mode, which can be eliminated by rotating the pattern matrix to properly describe the transformation between the lab and the mode frames.

spherical harmonics to form a new set of spherical harmonics. The rotation was restricted so that the orthogonality of the wave functions was maintained.

We chose to use the y-convention of the Euler angles to perform the rotations. We ignored the first rotation  $\alpha$  about the z axis. The  $\beta$  rotation about the y axis mixed mode 5 with the other 4 modes. To keep the orthogonality between modes, we performed this rotation on all modes at once, or in other words we rotated the entire mode frame relative to the lab frame. The  $\gamma$  rotation about the new z axis mixed modes 1 with 2, and 3 with 4, but not 1 with 3 or 4, etc. The rotations could be different for each pair because the modes would remain orthogonal under  $\gamma$  rotation. Mode 5 was unaffected by any  $\gamma$  rotation.



Rotation	Angle (deg)
$\beta$	1.0
$\gamma_{12}$	-0.1
$\gamma_{34}$	-7.2

Table 4.1: Angles used to rotate the pattern matrix to properly describe the transformation between the lab and the mode frames.

To fit for the rotations we minimized the deviations of a least squares fit of the magnitudes of each mode channel to a simple exponential decay. We did three separate fits, one for modes 1 and 2, and another for modes 3 and 4. We also did a fit for  $\beta$  by minimizing the deviations for the  $Y_5$ -mode. The results are shown in Table 4.1.

The effects of the rotations were quite satisfying. As shown in Figure 4.13, each mode separated from the others and behaved as expected, as a exponentially decaying harmonic oscillator. Figure 4.14 shows each mode channel in the complex plane. Each mode follows a spiral. The number of turns (beat cycles) depends on a mode's frequency difference from the lock-in reference. From the polar plots, we can follow the initial excitation of the modes to determine the phase of each mode relative to the others. The small remaining oscillations, or "wiggles", are due to an imperfect separation of the modes into mode channels. This is most easily seen by looking at the spectral density of the mode channels shown in Figure 4.15. There is still between 0.008% and 2% admixture from the other quadrupole modes, which could not be eliminated with simple rotations of the wave-functions. It may be possible to lower the level of admixture by more precisely positioning the

accelerometers and impulse hammer. However, this result does indicate that the TI is a good approximation for a sphere, having less than 2% deviation from the eigenfunctions of an ideal sphere.

Also shown in Figure 4.14 is the magnitude of the mode channels. By performing a least square fit of the magnitudes we are able to measure the initial amplitude of the excited sphere modes and their Q. The average Q of the five quadrupole modes was  $\simeq 20,000$  in air.

## 4.7 Mode Response

Because we know the location and direction of the applied impulse, we should be able to predict the magnitude of the response of each mode. The output of each accelerometer is a superposition of the wavefunctions of all the modes at that accelerometer's location. It is possible to calculate the magnitudes of the wavefunctions at these locations for an impulse excitation and compare the result to the measured response, but we have devised a model that simplifies the calculation.

If the prototype had truly degenerate quadrupole modes, we would be free to choose a basis set with arbitrary orientation to describe the sphere modes. If we chose an orientation, such that the  $z'$  axis in the mode frame was along the direction of the impulse, then only a *single* mode ( $Y_5$ ) in that frame would be excited. All of the other modes have radial nodes at the north pole (see Figure 2.1), so they would *not* be excited by an impulse at that location.

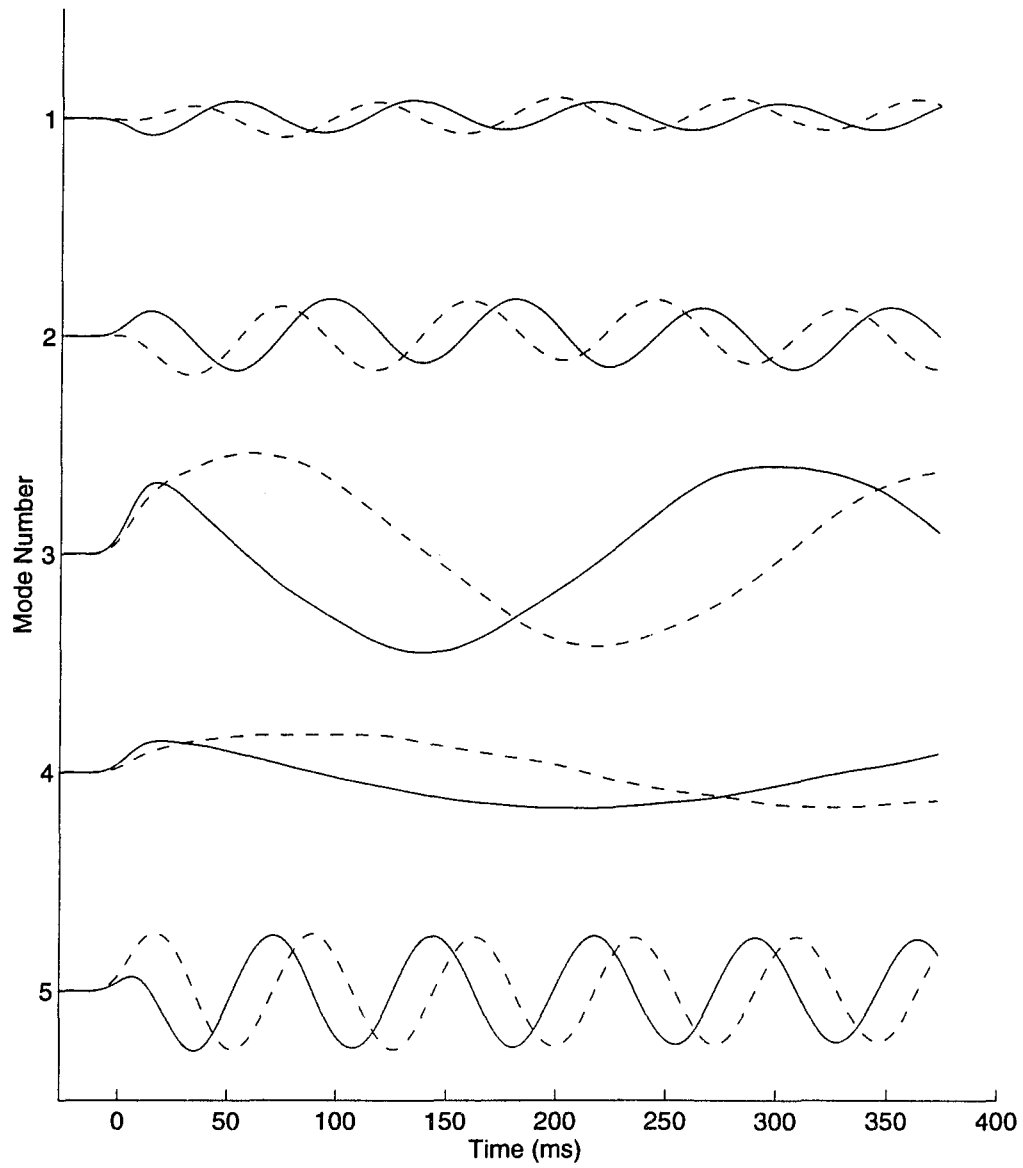


Figure 4.13: In-phase (solid lines) and quadrature (dashed lines) of the mode channels calculated from the data shown in Figure 4.10 using the rotated pattern matrix.

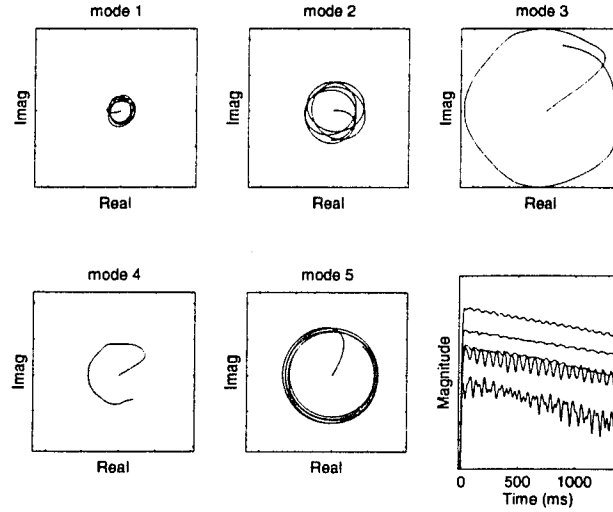


Figure 4.14: Phase and magnitude of the mode channels calculated from the data shown in Figure 4.10 using the rotated pattern matrix.

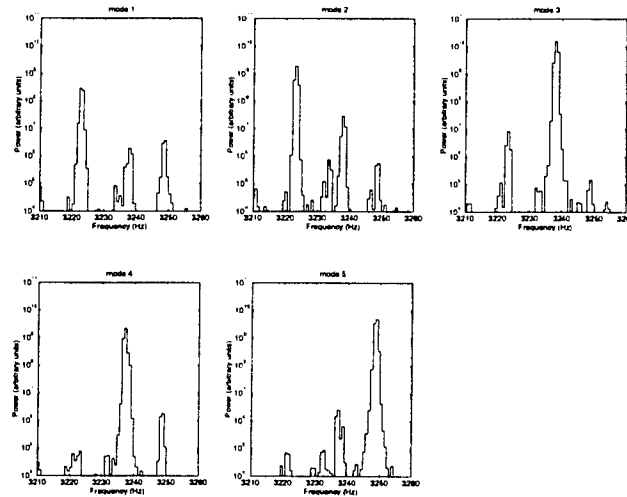


Figure 4.15: Spectral density of the five mode channels calculated using the rotated pattern matrix. As discussed in the text, the smaller peaks in each mode channel are not quite eliminated by simple rotations of the pattern matrix.

If the impulse is on a pentagon face, using the  $Y_5$ -mode shape, we conclude that the acceleration at the opposite face has a maximum, and by symmetry, the other five accelerometers surrounding will have smaller but equal magnitude. Their size relative to the amplitude of the accelerometer opposite to the hit should be

$$\frac{Y_5(63.4737^\circ, 0^\circ)}{Y_5(0^\circ, 0^\circ)} = -0.2008 \quad (4.1)$$

According to this model, if we transform back the initial amplitudes of the mode channels, we should get the initial amplitudes of the accelerometers. Figures 4.16 and 4.17 show the results of this calculation for several different impulse positions. For each impulse, we have the accelerometer opposite the hit getting excited by a large amount. The other five are also excited but to a lesser amplitude. The ratio of the amplitudes fits well with the number given in equation (4.1). The accelerometer opposite the impulse has opposite phase from the others because it lies on the other side of the line of nodes.

To calculate the initial magnitude of each accelerometer we need to know the initial relative phase of each mode channel. Due to filtering and other initial transients this cannot be done by simply looking at the measured phase at the time of the impulse. Instead, we do a least square fit to the phase (see Figure 4.18) well after the impulse (about 300 ms after). This allows us to extrapolate back to the initial impulse. There are some small systematic variances in the phase, probably due to phase differences in the

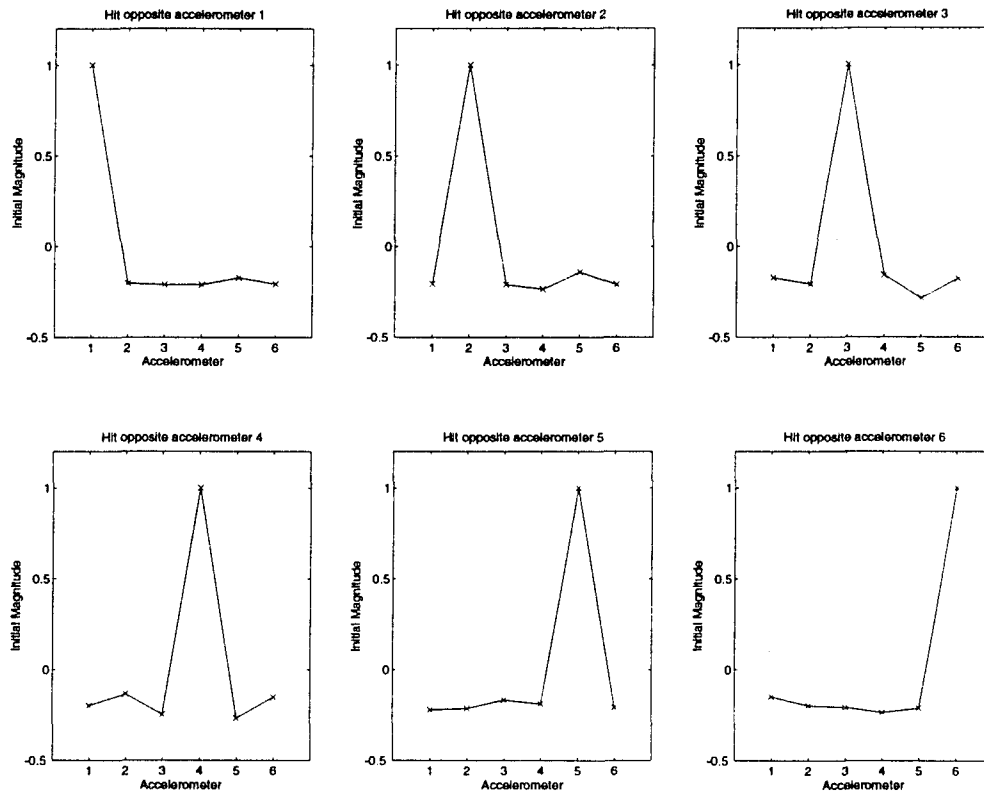


Figure 4.16: Calculated initial amplitudes of the accelerometers from impulses on pentagonal faces. They are normalized to the accelerometer opposite the impulse. The numbering of the faces correspond to the numbering scheme shown in Figure 2.7.

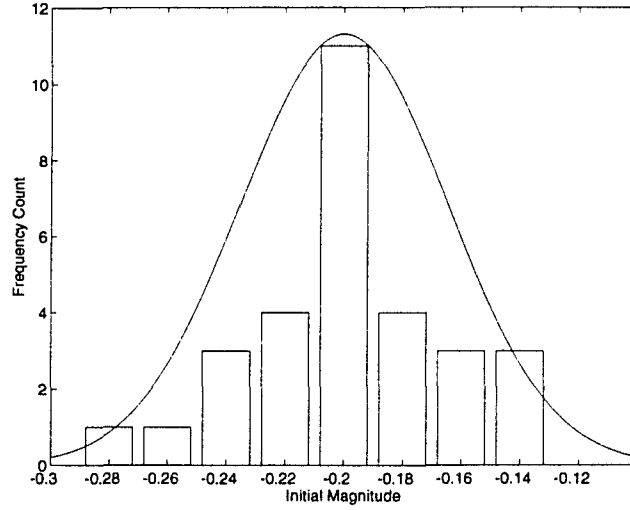


Figure 4.17: Histogram of the calculated initial amplitudes of the accelerometers from impulses on pentagonal faces. They are normalized to the accelerometer opposite the impulse. The ratio between the accelerometer opposite to the impulse to the other accelerometers is consistent with the theoretical value of -0.2008.

lock-ins and the mode channels frequency offset from the reference, but these can easily be taken into account.

## 4.8 Impulse Direction

The previous section verified that an impulse will only excite the  $Y_5$  mode in a reference frame where the  $z'$  axis is along the direction of the impulse. If only the  $Y_5$  mode is excited, then the only non-zero mode amplitude in that frame will be  $h_5$ . From equation (2.15) we see that, in this frame, the cartesian strain tensor will be diagonal, and the direction of the impulse will be in the direction of  $h_{3'3'}$ .

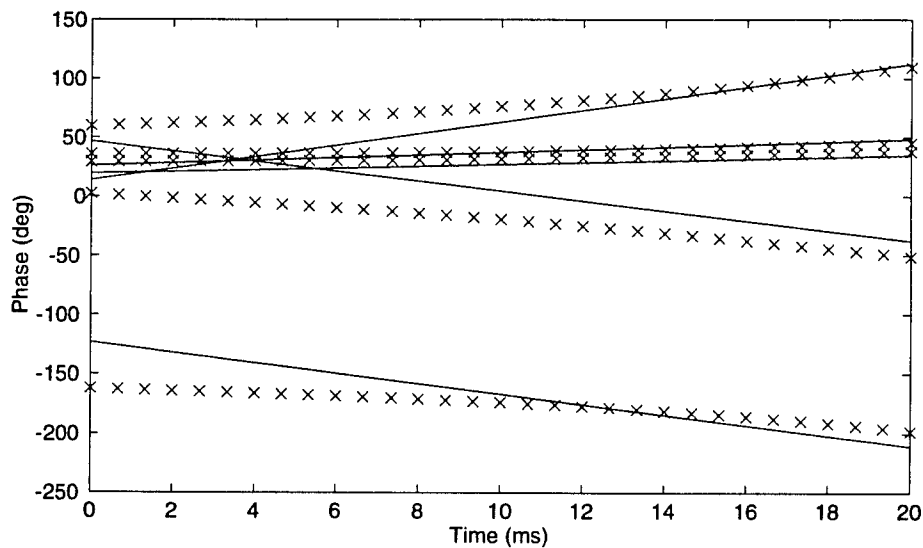
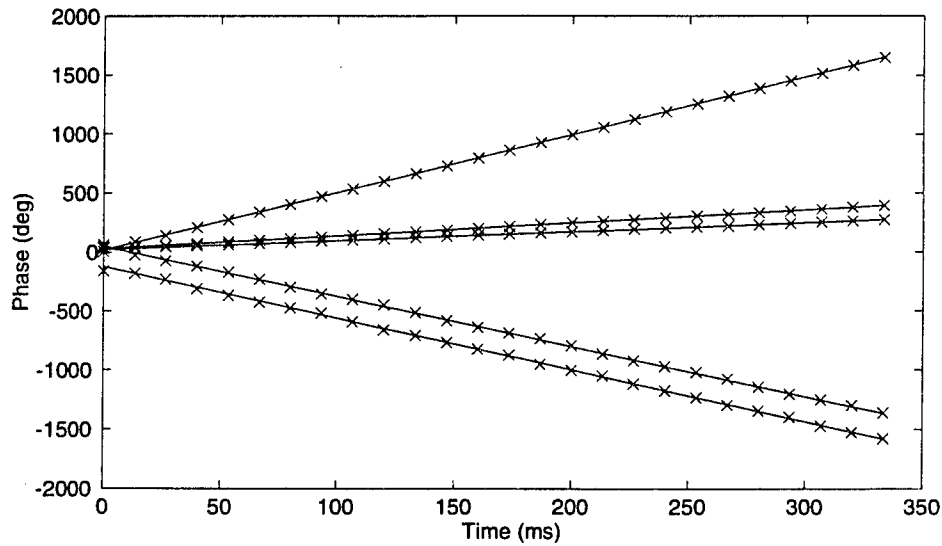


Figure 4.18: The phase of the mode channels for a typical impulse excitation. The  $\times$ 's are the measured phase, and the solid lines are a least square fit to the data. The fit appears to deviate from the data at the beginning because filtering of the data produces a lag in the phase.



However, suppose we do not know the direction of an impulse *a priori*. To determine the impulse direction, we diagonalize the lab frame cartesian strain tensor. This will find the transformation to a frame where only the  $Y_5$  mode is excited, so *the eigenvector of the  $h_{3'3'}$  eigenvalue (the maximum eigenvalue) will point in the direction of the impulse.*

The mode channels are proportional to the spherical amplitudes, so to determine the direction of the impulse we can replace  $h_m$  in equation (2.15) with the mode channels  $g_m$ . The mode channels were calculated using equation (2.43) where  $\underline{q}(t)$  are now the accelerometer outputs.

The results of this calculation for nine impulse locations are shown in Figure 4.19 and Table 4.2. The angles calculated from the data were very consistent; with three hits at each location, the overall standard deviation from the mean was  $\sim 0.4^\circ$ . The calculated locations were all within  $\sim 3\%$  of the values expected from the measured position of the impulse hammer. Most of the deviation from the expected values is apparently due to systematic errors, perhaps from imprecise placement of the accelerometers or the impulse hammer. The random errors were small compared to these systematic errors.

The accelerometers were positioned to the center of each pentagon face with an accuracy of about 0.5 cm. The hammer was positioned to with about the same accuracy, but its angle of impact was much more difficult to control. We estimate the accuracy on the angle of impact to be about  $5^\circ$ . For this stage of testing we felt that a 3% systematic error was acceptable.

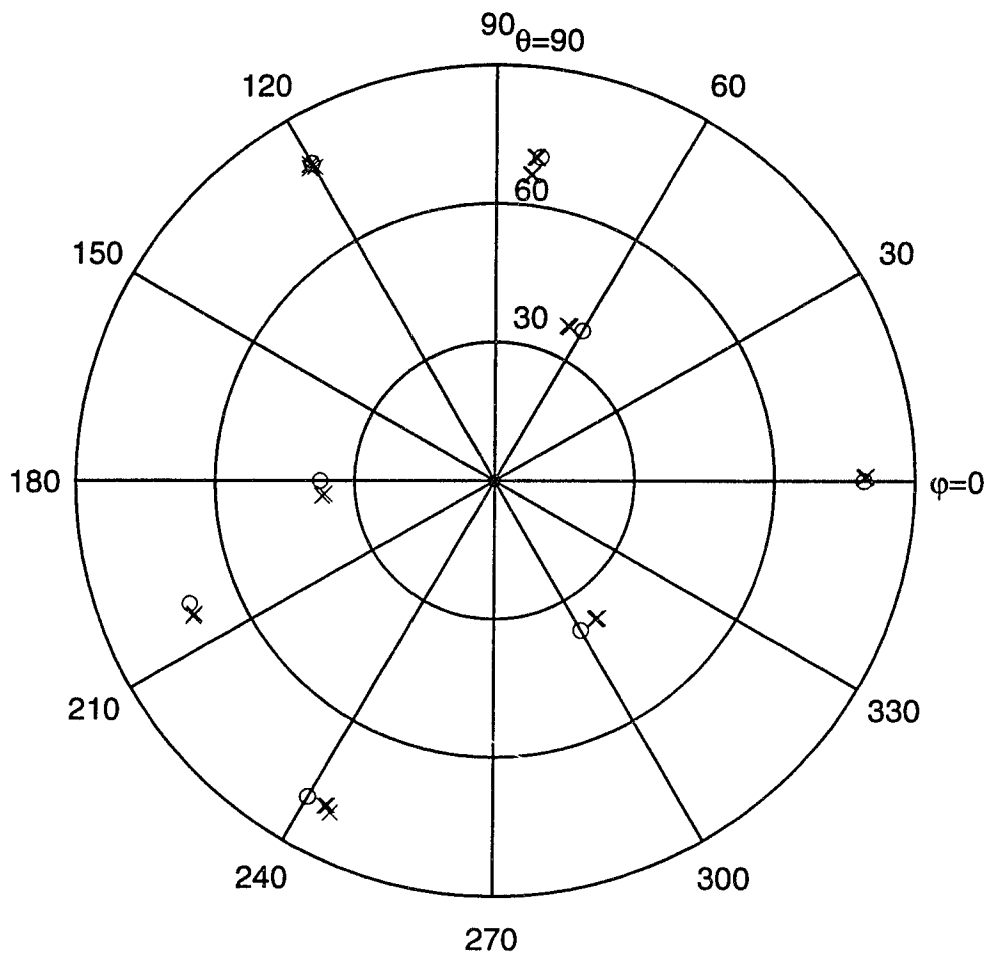


Figure 4.19: Location of several impulses calculated by diagonalizing the cartesian strain tensor. The x's mark the calculated locations, and the o's mark the expected location.

Impulse Face	$\theta$ Calculated	$\theta$ Expected	$\varphi$ Calculated	$\varphi$ Expected
Pent 1	36.8°	37.3°	64.6°	60.0°
Pent 2	37.0°	37.3°	-53.4°	-60.0°
Pent 3	36.8°	37.3°	-175.1°	180.0°
Pent 4	79.3°	79.1°	-116.4°	-120.0°
Pent 5	79.4°	79.1°	0.6°	0.0°
Pent 6	78.6°	79.1°	120.2°	120.0°
Top Hex 6	70.4°	70.5°	82.9°	82.2°
Bottom Hex 6	66.5°	70.5°	83.4°	82.2°
Top Hex 8	70.6°	70.5°	-155.6°	-157.7°

Table 4.2: The average location of several impulses calculated by diagonalizing the cartesian strain tensor. All the impulses to pentagon faces are opposite the accelerometer with the same identification number.

## 4.9 Experimental Obstacles

As with most experiments, the experimental techniques used often have limitations or problems associated with them. In this section we describe some of the problems we came across and how we fixed them.

Repeatability of impulses was a major problem in the beginning. Each time we hit the prototype with the hammer the response of the accelerometers was not consistent. One reason for the deviation was that the hammer was hitting the surface at slightly different angles and different positions for each impulse. A human can only position a hammer so well by eye, thus a mechanical device is necessary to get consistent impulses. The device we built was a shaft attached to a test stand. Figure 4.20 shows the hammer attached to the shaft, which can then be easily positioned to strike the prototype in a consistent manner. A spring (rubber band) was attached to the hammer to help prevent it from hitting the prototype more than once.

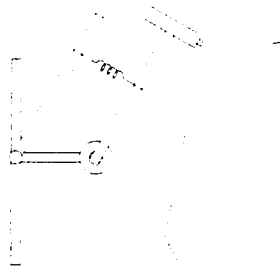


Figure 4.20: Impulse hammer held by a test stand. The spring attached to the hammer was used to prevent multiple hits to the prototype.

A major problem with taking this data digitally was aliasing. As described in section 4.1, most aliasing could be eliminated through filters. However, the filters we had did not roll-off quickly enough, so large signals at high frequency would get through. To help reduce the problem we looked at ways to avoid exciting the high frequency modes of the prototype. We accomplished this by changing the tip on the impulse hammer. We originally used a hard metal tip, which is specified to have good response to about 10 kHz. We switched it with a medium hardness tip which is specified to have good response to about 5 kHz. Because this reduced the number of high frequency modes being strongly excited, the aliasing was decreased to a tolerable level.

Another problem was irreproducibility in the response due to variations on how well the accelerometers were waxed to the prototype. The only solution found was to calibrate the system using the monopole mode prior to each test.

# Chapter 5

## Summary

The first half of this dissertation developed a theory for the mechanical behavior of a spherical gravitational wave antenna. We developed a multimode mechanical model for a sphere with an arbitrary number of mechanical resonators attached to its surface. The resonators act as mechanical-impedance transformers between the primary vibrational modes of the sphere and the actual motion sensors, producing an essential increase in the electro-mechanical coupling.

We modeled a specific arrangement of six mechanical resonators which we term the truncated icosahedral arrangement. We found an analytic solution to the coupled equations of motion for this arrangement. This arrangement resulted in equal frequency splitting of the coupled modes and equal coupling between all the attached resonators and the sphere's quadrupole modes. In other words, all the resonators were equally sensitive to the sphere modes.

We developed a specific set of linear combinations of the resonator displacements that enabled us to extract all the information about an incident gravitational wave. We called the resulting combinations “mode channels.” They had a one-to-one correspondence with the sphere modes and thus to the tensor components of a gravitational wave.

A simple noise model was constructed to predict the sensitivity of a spherical antenna. We found that a sphere is 56 times more sensitive in energy than an equivalent bar.

The second half of this dissertation described the testing of a room-temperature prototype TIGA. The prototype was constructed to examine the practical problems of applying the ideal mechanical description of a sphere, developed in the first half of this dissertation, to an actual detector.

The mode structure of the uncoupled prototype’s modes were verified. All the prominent modes were identified in the frequency domain. The quadrupole modes were no longer degenerate, but their frequency splitting could be understood by symmetry arguments.

The eigenfunctions of the uncoupled prototype were fixed in a particular orientation but were otherwise unchanged to within 2%. We were able to adjust the linear combinations of accelerometer outputs for the fixed orientation of the eigenfunctions to obtain mode channels. As a final test of the uncoupled system, we used these mode channels to reconstruct the location of an impulse excitation. The results were consistent with the expected location of the impulse within a 3% systematic error.

The results presented in this dissertation have verified several of the elements of our approach and theory for a multimode spherical antenna coupled to many resonators. The results presented here will be the foundation for the next stage of testing the prototype: the addition of mechanical resonators. The preliminary investigation of the prototype coupled to several resonators, presented in appendix B, lead us to believe we have not ignored any major factors in our theoretical model.

The next step in this project will be the verification that the non-degeneracy of the sphere modes and the small discrepancies of transducer tuning can be handled by the device of “mode channels”, and that the same methods can be used to reconstruct the direction of the excitation. We expect that the procedures developed for the uncoupled sphere should still apply in the coupled case.

Although a complete investigation of the practicality of a spherical gravitational wave antenna has not been completed, this work has generated great excitement in the field of resonant mass detectors. Several groups have begun exploring the possibility of constructing large spherical antennas. These include GRAVITON in Brazil, GRAIL in the Netherlands, ELSA in Italy, and TIGA in the United States. Two collaborations to build such antennas have also been formed: the US Gravity Wave Co-op and the international OMEGA collaboration.

# References

- [1] W. O. Hamilton, in *Proceedings of the Sixth Marcel Grossmann Conference on General Relativity and Gravitation*, edited by H. Sato and T. Nakamura (World Scientific Publishing Co., Singapore, 1992).
- [2] K. S. Thorne, in *Three Hundred Years of Gravitation*, edited by S. W. Hawking and W. Israel (Cambridge University Press, Cambridge, 1987).
- [3] C. W. Misner, K. S. Thorne, and J. Wheeler, *Gravitation* (W. H. Freeman, San Francisco, 1973).
- [4] A. Papoulis, *Signal Analysis* (McGraw-Hill, Inc., New York, 1977).
- [5] G. Tammann, in *Supernova: A Survey of Current Research*, edited by M. J. Rees and R. J. Stoneham (D. Reidel Publishing, Dordrecht, 1982).
- [6] R. A. Hulse and J. H. Taylor, *Astrophys. J. Lett.* **195**, L51 (1975).
- [7] J. Weber, *Phys. Rev.* **117**, 306 (1960).
- [8] J. Weber, *Phys. Rev. Lett.* **17**, 1228 (1966).
- [9] J. Weber, *Phys. Rev. Lett.* **22**, 1320 (1969).
- [10] W. M. Fairbank, W. O. Hamilton, and C. W. F. Everitt, in *Relativity*, edited by M. Carmeli, S. I. Fickler, and L. Whitten (Plenum Press, New York, 1970).
- [11] P. Astone *et al.*, *Phys. Rev. D* **47**, 362 (1993).
- [12] D. G. Blair *et al.*, *Phys. Rev. Lett.* **74**, 1908 (1995).
- [13] P. Astone *et al.*, *Europhysics. Letters* **16**, 231 (1991).



- [14] W. W. Johnson and S. M. Merkowitz, *Physical Review Letters* **70**, 2367 (1993).
- [15] R. Forward, *General Relativity Gravitation* **2**, 149 (1971).
- [16] R. V. Wagoner and H. J. Paik, in *Proceedings of International Symposium on Experimental Gravitation, Pavia* (Roma Accademia Nazionale dei Lincei, Roma, 1976), pp. 257–265.
- [17] S. Merkowitz and W. Johnson, *Physical Review D* **51**, 2546 (1995).
- [18] J. D. Jackson, *Classical Electrodynamics*, 2nd ed. (John Wiley & Sons, New York, 1975).
- [19] H. Goldstein, *Classical Mechanics*, 2nd ed. (Addison-Wesley Publishing Company, Reading, Massachusetts, 1980).
- [20] C. Zhou and P. F. Michelson, *Physical Review D* **51**, 2517 (1995).
- [21] N. S. Magalhães, W. W. Johnson, C. Frajuca, and O. D. Aguiar, *Monthly Notices of the Royal Astronomical Society* (1994), accepted September 1994.
- [22] L. D. Landau and E. M. Lifshitz, *Theory of Elasticity*, 3rd ed. (Pergamon Press, New York, 1986).
- [23] P. Jaerisch, *J.f. Math. (Crelle)* **Bd. 88**, (1880).
- [24] H. Lamb, in *Proceedings of the London Mathematical Society* (1882), Vol. 13.
- [25] N. Ashby and J. Dreitlein, *Physical Review D* **12**, 336 (1975).
- [26] P. F. Michelson and R. C. Taber, *J. Appl. Phys.* **52**, 4313 (1981).
- [27] P. Pearce and S. Pearce, *Polyhedra Primer* (Van Nostrand Reinhold Company, New York, 1978).
- [28] J. C. Price, *Physical Review D* **36**, 3555 (1987).
- [29] R. P. Giffard, *Physical Review D* **14**, 2478 (1976).
- [30] A. Abramovici *et al.*, *Science* **256**, 325 (1992).

- [31] N. Solomonson, W. W. Johnson, and W. O. Hamilton, Physical Review D **46**, 2299 (1992).
- [32] COSMOS/M, Structural Research & Analysis Corporation, 2951 28th Street, Suite 1000, Santa Monica, CA 90405.
- [33] FAMCO Enterprises, Inc., P.O. Box 143, Port Allen, LA 70767
- [34] DVX boards, Analogic Corporation, 8 Centennial Dr., Peabody, MA 01960.
- [35] EG&G Princeton Applied Research, P.O. Box 2565, Princeton, NJ 08543.
- [36] PCB Piezotronics, Inc., 3425 Walden Ave., Depew, NY 14043.
- [37] 5 minute epoxy, Cole Parmer Instrument Co., 7425 North Oak Park Ave., Niles, IL 60714
- [38] Stycast©, Emerson & Cumings, Inc., 77 Dragon Court, Woburn, MA 01888.
- [39] MATLAB©, The Math Works, Inc., 24 Prime Park Way, Natick, MA 01760.

## Appendix A

# Solution of the Equations of Motion

The equations of motion for a sphere with resonators were given by equation (2.34). We simplify this equation by making a number of transformations. First, we transform the resonator displacements and sphere amplitudes into the eleven mass weighted coordinates  $\underline{w}$ :

$$\begin{bmatrix} \underline{a} \\ \underline{q} \end{bmatrix} = \underline{\gamma} \underline{w} \equiv \begin{bmatrix} \frac{1}{\sqrt{m_S}} I & \underline{0} \\ \underline{0} & \frac{1}{\sqrt{m_R}} I \end{bmatrix} \underline{w}. \quad (\text{A.1})$$

Next, we remove the matrix multiplying the second time derivatives by multiplying both sides of the equation by its inverse. We end up with the equation

$$\begin{aligned}
& \ddot{\underline{w}} + \omega_o^2 \begin{bmatrix} \underline{I} & -\sqrt{\frac{m_R}{m_S}} \alpha \underline{B} \\ -\sqrt{\frac{m_R}{m_S}} \alpha \underline{B}^T & (\underline{I} + \frac{m_R}{m_S} \alpha^2 \underline{B}^T \underline{B}) \end{bmatrix} \underline{w} \\
&= \frac{1}{\sqrt{m_S}} \begin{bmatrix} \underline{I} & -\alpha \underline{B} \\ -\sqrt{\frac{m_R}{m_S}} \alpha \underline{B}^T & \sqrt{\frac{m_R}{m_S}} (\frac{m_S}{m_R} \underline{I} + \alpha^2 \underline{B}^T \underline{B}) \end{bmatrix} \begin{bmatrix} \underline{F}^S \\ \underline{F}^N \end{bmatrix}, \quad (\text{A.2})
\end{aligned}$$

which is of the form  $\ddot{\underline{w}} + \omega_o^2 \underline{M} \underline{w} = \underline{K} \underline{F}$ . The matrix  $\underline{M}$  is symmetric, therefore it can be diagonalized by the transformation  $\underline{U}^T \underline{M} \underline{U} = \underline{D}$  where  $\underline{U}$  is a set of eigenvectors, and  $\underline{D}$  is the diagonal matrix of the eigenvalues of  $\underline{M}$ . Substituting this in equation (A.2) and multiplying by  $\underline{U}^T$  we get

$$\ddot{\underline{\eta}} + \omega_o^2 \underline{D} \underline{\eta} = \underline{U}^T \underline{K} \underline{F}, \quad (\text{A.3})$$

where  $\underline{\eta}$  are now our normal coordinates. The problem has now been reduced to eleven decoupled harmonic oscillator equations that can easily be solved in a number of different ways. We begin by taking the Fourier transform of equation (A.3),

$$\underbrace{(-\omega^2 \underline{I} + \omega_o^2 \underline{D}(\omega))}_{\underline{G}^{-1}(\omega)} \underline{\eta}(\omega) = \underline{U}^T \underline{K} \underline{F}(\omega). \quad (\text{A.4})$$

Because  $\underline{D}(\omega)$  is diagonal,  $\underline{G}^{-1}(\omega)$  is diagonal, so its inverse is just the diagonal elements inverted. The normal coordinates are:

$$\underline{\eta}(\omega) = \underline{G}(\omega) \underline{U}^T \underline{K} \underline{F}(\omega) \quad (\text{A.5})$$

To return to the original coordinates we reverse the transformations:

$$\begin{bmatrix} \underline{a}(\omega) \\ \underline{q}(\omega) \end{bmatrix} = \underline{\gamma} \underline{U} \underline{\eta}(\omega) = \underline{\gamma} \underline{U} \underline{G}(\omega) \underline{U}^T \underline{K} \underline{F}(\omega). \quad (\text{A.6})$$

For the TI arrangement, the eigenvectors  $\underline{U}$  have the form given in equations (2.38) and (2.39), with the result that the matrices become:

$$\underline{\gamma} = \begin{bmatrix} \frac{1}{\sqrt{m_S}} \underline{I} & \underline{0} \\ \underline{0} & \frac{1}{\sqrt{m_R}} \underline{I} \end{bmatrix} \quad (\text{A.7})$$

$$\underline{K} = \frac{1}{\sqrt{m_S}} \begin{bmatrix} \underline{I} & -\alpha \underline{B} \\ -b \underline{B}^T & \sqrt{\frac{m_S}{m_R}} (\underline{I} + b^2 \underline{B}^T \underline{B}) \end{bmatrix} \quad (\text{A.8})$$

$$\underline{U} = \begin{bmatrix} n_+ \underline{I} & n_- \underline{I} & \underline{0} \\ n_+ c_+ \underline{B}^T & n_- c_- \underline{B}^T & n_o \underline{1} \end{bmatrix} \quad (\text{A.9})$$

$$\underline{G}(\omega) = \begin{bmatrix} \frac{1}{(\omega_+^2 - \omega^2)} \underline{I} & \underline{0} & \underline{0} \\ \underline{0} & \frac{1}{(\omega_-^2 - \omega^2)} \underline{I} & \underline{0} \\ \underline{0} & \underline{0} & \frac{1}{(\omega_o^2 - \omega^2)} \end{bmatrix} \quad (\text{A.10})$$

where  $b \equiv \alpha \sqrt{m_R/m_S}$  and  $n_{\pm}$ ,  $c_{\pm}$ , and  $n_o$  are given in equations (2.40)-(2.42).

To simplify further we define the following

$$\alpha_{\pm} \equiv \frac{3}{2\pi} n_{\pm}^2 c_{\pm} \left( 1 - \frac{3}{2\pi} c_{\pm} b \right) \quad (\text{A.11})$$

$$\beta_{\pm} \equiv \frac{3}{2\pi} n_{\pm}^2 c_{\pm} \sqrt{\frac{m_S}{m_R}} \left( -b + c_{\pm} \left( 1 + \frac{3}{2\pi} b^2 \right) \right) \quad (\text{A.12})$$

$$\omega_{\pm}^2 \equiv \lambda_{\pm} \omega_o^2. \quad (\text{A.13})$$

After some algebra we find the resonator displacements and sphere mode amplitudes to be given by:

$$\begin{aligned} \underline{a}(\omega) = & \frac{2\pi}{3m_S} \left( \frac{\alpha_+/c_+}{(\omega_+^2 - \omega^2)} + \frac{\alpha_-/c_-}{(\omega_-^2 - \omega^2)} \right) \underline{F}^S(\omega) \\ & + \frac{2\pi}{3m_S} \left( \frac{\beta_+/c_+}{(\omega_+^2 - \omega^2)} + \frac{\beta_-/c_-}{(\omega_-^2 - \omega^2)} \right) \underline{\underline{B}} \underline{F}^N(\omega), \end{aligned} \quad (\text{A.14})$$

$$\begin{aligned} \underline{q}(\omega) = & \frac{2\pi}{3\sqrt{m_S m_R}} \left( \frac{\alpha_+}{(\omega_+^2 - \omega^2)} + \frac{\alpha_-}{(\omega_-^2 - \omega^2)} \right) \underline{\underline{B}}^T \underline{F}^S(\omega) \\ & + \left[ \frac{2\pi}{3\sqrt{m_S m_R}} \left( \frac{\beta_+}{(\omega_+^2 - \omega^2)} + \frac{\beta_-}{(\omega_-^2 - \omega^2)} \right) \underline{\underline{B}}^T \underline{\underline{B}} \right. \\ & \left. + \frac{1}{6m_R(\omega_o^2 - \omega^2)} \underline{\underline{1}} \right] \underline{F}^N(\omega). \end{aligned} \quad (\text{A.15})$$

To convert the resonator displacements to mode channels we need only multiply by the pattern matrix  $\underline{\underline{B}}$ . In the frequency domain, the mode channels, in terms of the noise forces, are given by the remarkably simple expression

$$\begin{aligned} \underline{g}(\omega) = & \frac{1}{\sqrt{m_S m_R}} \left( \frac{\alpha_+}{(\omega_+^2 - \omega^2)} + \frac{\alpha_-}{(\omega_-^2 - \omega^2)} \right) \underline{F}^S(\omega) \\ & + \frac{1}{\sqrt{m_S m_R}} \left( \frac{\beta_+}{(\omega_+^2 - \omega^2)} + \frac{\beta_-}{(\omega_-^2 - \omega^2)} \right) \underline{\underline{B}} \underline{F}^N(\omega) \end{aligned} \quad (\text{A.16})$$

$$\equiv \sigma(\omega) \underline{F}_m^S(\omega) + \sum_j H_{mj}(\omega) \underline{F}_j^N(\omega). \quad (\text{A.17})$$

# Appendix B

## Prototype with Resonators

### B.1 Resonator Design and Tuning

Chapter 2 lists the rudimentary requirements for a resonator, but practical considerations require a more extensive list. First, the “transducer mode” must be reasonably easy to tune to the quadrupole frequency. Second, the transducer mode must be purely radial, so that it couples strongly only to the radial motion of the quadrupole modes. Third, there should not be any other modes of the resonator nearby in frequency. Fourth, there must be a practical method of attachment with sufficient mechanical  $Q$ .

The design we adopted approximates a lumped mass and a spring. The lumped mass, or “head”, is attached to a thin stem, or “neck.” The neck is fixed to a base. The transducer mode is such that radial motion of the head compresses and extends the neck against the base. While the neck is

relatively rigid in the radial direction, it is relatively flexible in the transverse directions, which decouples the transducer mode from transverse motions. The length and diameter of the neck can be adjusted to move the rocking and toroidal modes of the resonator well below the transducer mode frequency. Figure B.1 shows the dimensions of the resonator.

We used finite element analysis to fix the final parameters of the resonator. The transducer frequency was first tuned by modeling the resonator with its base attached to an infinite mass. We then modeled the same design attached to a small mass, because we anticipated attaching the resonators to a small aluminum block to test the tuning of the transducer mode. Table B.1 shows the results of the two models as well as measurements of the mode frequencies of the first machined resonator before any fine tuning was performed.

Initial testing of the resonators on the small mass looked promising; however, when we mounted the first resonator on the prototype, the coupled frequency was  $\sim 100$  Hz low. This is only a 3% discrepancy, but we needed to tune them more accurately. It was decided that we should tune the resonators while attached to the prototype rather than to the small mass.

By testing the resonator while attached to the prototype, we could use the equations developed in section 2.4 to calculate the coupled mode frequencies of the prototype and a single resonator. We combined the lumped mass model for the resonators with equation (2.34) for this purpose. We measured the coupled mode frequencies of the prototype and one resonator and compared them to the eigenvalue solution of equation (2.34) to determine the spring



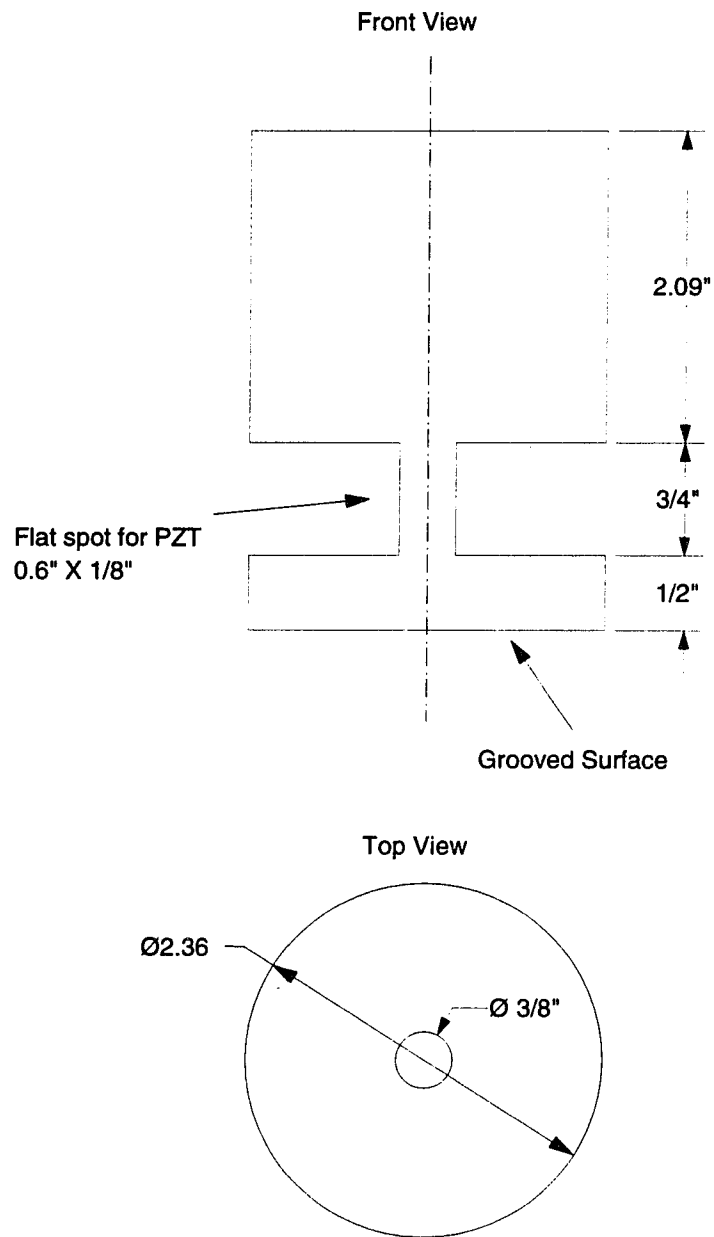


Figure B.1: Schematic of the resonator.

Calculated (Infinite Mass)	Calculated (Small Mass)	Measured (Small Mass)	Mode Description
181	193	194	head rocks
181	193	197	head rocks
345	346	352	head rotates
2252	2269	2185	head wobbles
2252	2269	2193	head wobbles
3234	3209	3118	transducer
24471	7807	—	—
29938	7830	—	—
29938	8624	—	—
30851	8968	—	—

Table B.1: The first ten eigenfrequencies for finite element models of the resonator. The boundary conditions for the models were 1. the base fixed to an infinite mass and 2. the base attached to the small mass. Also shown for comparison is the measurements of the resonator attached to the small mass prior to tuning.

constant of the neck of the small resonator. Appendix C gives the numerical procedure for calculating the eigenfrequencies and eigenvectors of the coupled system. The spring constant was determined by adjusting the spring constant in program 3 until the calculated eigenfrequencies matched the measured values.

Once the spring constant of the resonator is determined, we can calculate its uncoupled eigenfrequency:

$$f = \frac{1}{2\pi} \sqrt{\frac{\text{Transducer spring constant}}{\text{Transducer head mass}}}. \quad (\text{B.1})$$

This gave us two options for tuning the resonator: reduce the mass of the head, or lower the spring constant by reducing the diameter of the neck. If

the eigenfrequency was low, we made large reductions in the mass of the head by machining the top, and then made small adjustments by drilling holes in the end of the head. If the eigenfrequency was high we filed the side of the neck.

## B.2 Attachment of the Resonators

We attached the resonators to the prototype with epoxy. This method was chosen because it was a quick way to attach the resonators without permanently defacing the prototype. This method does, however, have a few difficulties: the resonator must be held in place while the epoxy is curing and it can be difficult to obtain a high mechanical quality factor  $Q$  of the coupled system. The first difficulty was easily solved: a flat rubber tiedown was strapped around the prototype to hold the resonators in place while the epoxy cured. The second difficulty required a little more work.

While testing the resonators on the small mass we experimented with details in the use of epoxy to attempt to improve the  $Q$  of the transducer mode, which was very poor in the first test. The first thing we tried was putting small groves in a checkerboard pattern across the base of the resonators. The groves were made by scratching the surface with a level gauge. This improved the  $Q$  dramatically from a smooth base. We tried deeper groves that were machined into the base, but this had negative results.

We also varied the type of epoxy. We tried “5 minute epoxy” from Cole Parmer [37], “Super Glue”, and Stycast©1266 [38]. The Stycast gave the best results ( $\sim 3100$ ) while the Super Glue gave the worst ( $\sim 0$ ).

To further improve the  $Q$ , we tried different methods of treating the epoxy. We first tried heating the resonator while the epoxy was curing. This gave inconsistent results. Heating would also be difficult once the resonator was attached to the prototype due to its large mass, so we did not pursue it further. Next we tried deairing the epoxy. The epoxy was placed in rough vacuum ( $\sim 1$  Torr) for about 10 minutes until it stopped bubbling. This improved the  $Q$  by about a factor of three.

Experimentally, we also found a few other steps that could improve the  $Q$ . The surface of the prototype should not be too smooth; a final sanding with 240 grit wet-dry sandpaper gave the best results. The layer of epoxy should not be too thin or thick; we found that applying extra epoxy to the base and then “working out” the excess by rubbing the resonator against the prototype’s surface in a circular fashion worked well. The best  $Q$  of the resonator we were able to reproduce while attached to the small mass was  $\sim 3100$  in air.

We also measured the  $Q$  of the resonator while attached to the prototype. The procedure for this is a little more complicated than when the resonator is attached to the small mass, because the resonator couples with the modes of the prototype. The effect of the coupling will be explained in more detail

Frequency (Hz)	Q
3116.6	10692
3222.5	122237
3233.6	107898
3236.8	40040
3242.8	98189
3272.8	28285
6878.5	181319

Table B.2: The frequency and Q of the modes of the prototype with one resonator in a vacuum (5 mTorr).

below. For this Q measurement we chose the coupled mode that was dominated by the transducer motion. It was at frequency 3117 Hz and had a Q of  $\sim 3900$  in air.

We also measured the Q of the prototype with one resonator in vacuum to determine how much of the mechanical loss was due to air damping. We excited the modes by putting a random voltage across a strain gauge epoxied to the neck of the resonator. This white noise is broad band so it excited all the modes we were interested in. We then disconnected the noise generator and switched the output of the strain gauge to a spectrum analyzer and measured the decay. The results are shown in Table B.2. The Q improved by about a factor of 2.5 for the mode that is dominated by the transducer motion (3117 Hz). This indicated that at this level, air damping plays a significant role in degrading the Q of the coupled system. Because of this, the final mode analysis testing of the system with six attached resonators will most likely need to be performed in vacuum.

### B.3 Coupled Antenna Spectra

The resonators were attached to the prototype one at a time, and the frequencies of the coupled modes were measured after each change. Equation 2.34 was solved to predict the behavior of the system as we attached each additional resonator.

The response of the resonators to an excitation was measured using a PZT strain gauge epoxied to the neck. The strain of the neck induces a strain in the PZT, which uses the piezoelectric effect to convert the strain to an electrical voltage. To measure the frequencies of the modes, we connected the strain gauge to a spectrum analyzer, which performed a Fourier transform on the signal.

We excited the modes with an impulse from a hammer in the same fashion that was used in testing the prototype without any resonators. We found that the impulse could not be applied to the head of the resonators. An impulse at this location would excite other modes of the resonator to too high an amplitude, thus overloading the function generator. Since these modes are not strongly coupled to the motion of the prototype's surface, they were not so highly excited when the impulse was applied to the prototype.

The strain gauge could also be used to drive the system. By putting a time dependent voltage across the PZT we could induce a strain in the neck of the resonator, exciting the modes. This was convenient when we wanted to excite a single mode. We could drive the PZT with a sine-wave at a

resonance frequency that would only excite the mode(s) at that frequency. This was also the method we used to excite the modes when the prototype was placed under vacuum in our bell jar where it was not practical to use the hammer.

The calculated and measured quadrupole mode frequencies were fairly consistent with each other. The non-degeneracy of the prototype's quadrupole modes did not introduce very much deviation from a perfectly degenerate system. It was also found that neither the toroidal modes nor the monopole mode were shifted by more than 1 Hz when the resonators were added. Figure B.2 shows the results of the frequency measurements of the coupled modes for each addition of a resonator. The results are compared with what is expected from the eigenvalue solution of equation (2.34). The two sets are consistent within 0.2%.

In section 4.6 we measured the eigenfunctions of the uncoupled system and found that, except for some rotations, they were within a few percent of the eigenfunctions calculated for a perfect sphere. Because there is good agreement between the measured and calculated frequencies of the *coupled* system, we conclude that the eigenfunctions have not been significantly altered. There may be a small amount of admixture between modes, but from the eigenfrequency results we estimate that it is below the 0.2% level. We should be able to measure the coupled modes orientation relative to the lab frame using the same methods developed in section 4.6. Once an accurate pattern matrix is measured, we should be able to determine the location and direction of a given excitation.

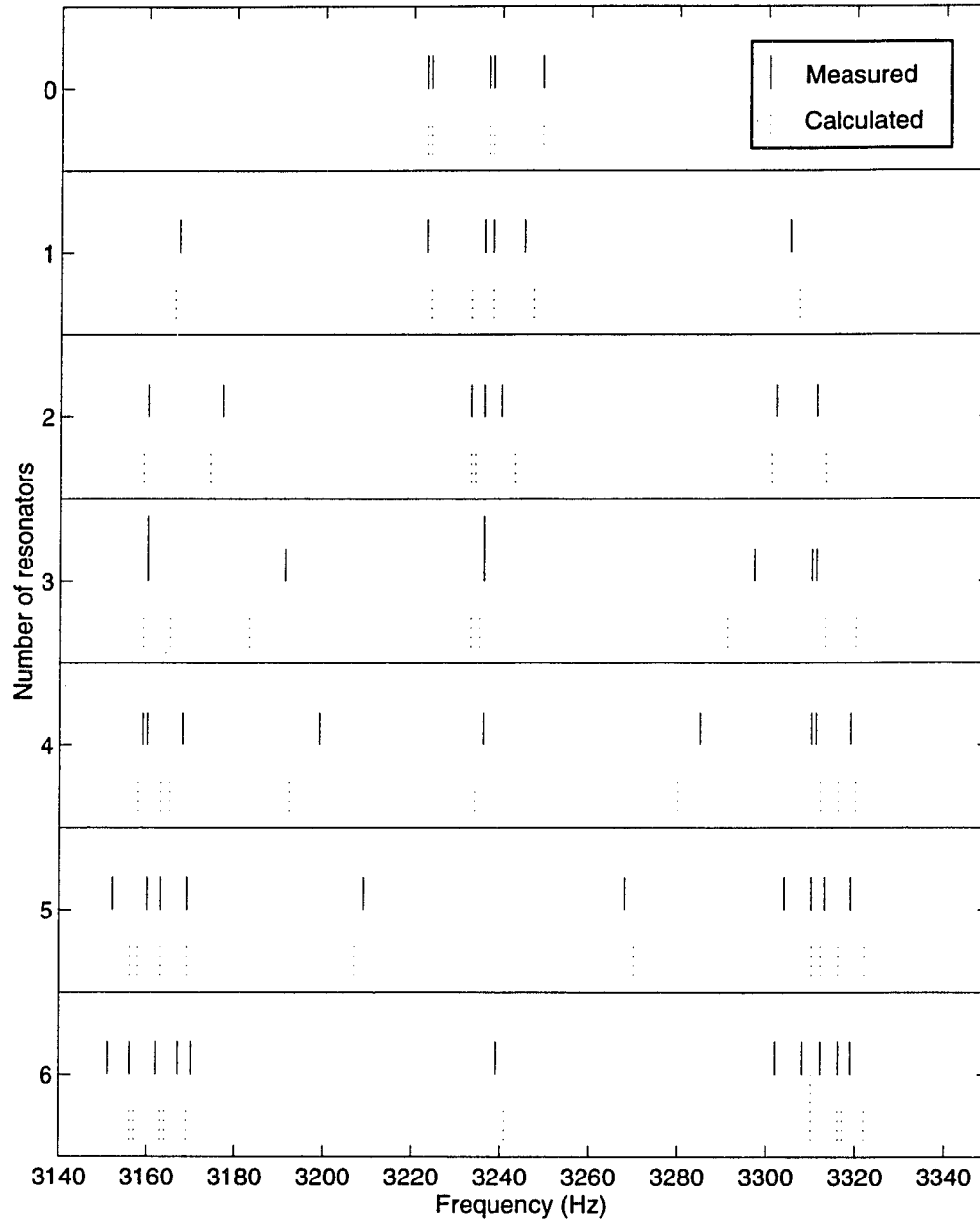


Figure B.2: Frequency measurements of the coupled modes for each addition of a resonator. The solid lines are the measured values and the dotted lines are the calculated. The lines that are double in height represent degenerate doublets.



# Appendix C

## Programs

The following programs are written in MATLAB®[39]. We include them here in the hopes that they may be useful to others. They are general enough that they may be easily adapted for various problems.

### Program 1 (lengths.m)

```
% Name:      lengths
%
% Purpose:   Calculate the distances and angles involved in
%            building a truncated icosahedron
%
% Notation:  angles have three letters, distances have two.
%            r = Radius of sphere
%            H = Hexagon center
%            P = Pentagon center
%            v = Vertex (corner)
%            e = Edge center
%            V = Vertex dodecahedron
%
```

```

r = 16.75; %inches

HcH = 41.8103 * pi/180;
PcH = 37.3773 * pi/180;
Hce = 0.5 * HcH;
ece = HcH;
Pce = PcH - Hce;
Pcv = atan(tan(Pce) / cos(36 * pi/180));
vcv = 2 * asin(sin(36 * pi/180) * sin(Pcv));
vce = 0.5 * vcv;
Hcv = acos(cos(Pcv) * cos(Hce) / cos(Pce));

cv = r;
vv = 2 * r * sin(vce);
Pv = r * sin(Pcv);
cP = r * cos(Pcv);
Pe = r * cos(Pcv) * tan(Pce);
ce = r * cos(Pcv) / cos(Pce);;
cH = ce * cos(Hce);
He = ce * sin(Hce);
Hv = r * sin(Hcv);
HH = 2 * cH * sin(HcH/2); % adjacent hexagons
PP = 2 * cP * sin((Pcv + vcv + PcH)/2); % adjacent pentagons

xvv = r * sin(Pcv+vcv) - Pv;

```

## Program 2 (Finite Element Model)

```
% Name:    tiga_points
%
% Purpose: To calculate the coordinates of the vertices of
%          a truncated icosahedron. Used to build the finite
%          element model of the TI
%
% Called:  lengths
%          sind (equivalent to sin(angle_in_degrees * pi/180))
%          cosd (equivalent to cos(angle_in_degrees * pi/180))
%
% Output:  File (soccer.dat) containing points
%
```

Lengths

```
z1 = cP; % top pentagon height
s1 = vv; % side length
r1 = Pe; % radius of inscribed circle
rr1 = Pv; % radius of circumscribed circle

p1 = [-s1/2,-r1,z1];
p2 = [s1/2,-r1,z1];
p3 = [-s1*(.5+cos(2*pi/5)) , s1*sin(2*pi/5)-r1 , z1];
p4 = [ s1*(.5+cos(2*pi/5)) , s1*sin(2*pi/5)-r1 , z1];
p5 = [0 , rr1 , z1];

z2 = r * cosd(Pcv + vcv);
s2 = 2 * Hv;
r2 = cH * sind(PcH);
rr2 = r * sind(Pcv + vcv);

pp1 = [-s2/2,-r2,z2];
pp2 = [s2/2,-r2,z2];
pp3 = [-s2*(.5+cos(2*pi/5)) , s2*sin(2*pi/5)-r2 , z2];
pp4 = [s2*(.5+cos(2*pi/5)) , s2*sin(2*pi/5)-r2 , z2];
pp5 = [0 , rr2 , z2];
```

```

% The third polygon is a nonregular decagon.
% Every other side has the same length.
% The two lengths are: the edge length of the pentagons
% and hexagons, and the length of a vertex diagonal of the
% pentagons. There are two possible inscribed circles but
% only one circumscribed circle.

z3 = ce * cosd(Pce+Hce+Hce);
s3 = vv; % edge length
s3p = 2*vv*sind(54); % vertex diagonal length
r3 = ce * sind(Pce+Hce+Hce); % decagon center to s3
rr3 = sqrt( (s3 / 2)^2 + (r3)^2 ); % decagon center to vertex
r3p = sqrt( (rr3)^2 - (s3p / 2)^2 ); % decagon center to s3p

% ang3 = angle between v on one side of an edge of length s3,
% the center of the decagon, and v on other side of edge.
% ang3p = angle between v on one side of an edge of length s3p,
% the center of the decagon, and v on other side of edge.
ang3 = 2 * asind( (s3 / 2) / rr3 );
ang3p = 2 * asind( (s3p / 2) / rr3 );

d1 = [-s3/2, -r3, z3];
d2 = [ s3/2, -r3, z3];
d3 = [-rr3*sind(ang3p+ang3/2), -rr3*cosd(ang3p+ang3/2), z3];
d4 = [ rr3*sind(ang3p+ang3/2), -rr3*cosd(ang3p+ang3/2), z3];
d5 = [-rr3*sind(ang3p+3*ang3/2), -rr3*cosd(ang3p+3*ang3/2), z3];
d6 = [ rr3*sind(ang3p+3*ang3/2), -rr3*cosd(ang3p+3*ang3/2), z3];
d7 = [-rr3*sind(ang3+ang3p/2), rr3*cosd(ang3+ang3p/2), z3];
d8 = [ rr3*sind(ang3+ang3p/2), rr3*cosd(ang3+ang3p/2), z3];
d9 = [-s3p/2, r3p, z3];
d10 = [ s3p/2, r3p, z3];

% The fourth polygon also is a nonregular decagon.
% Like the third, every other side has the same length.
% The two lengths are: the side length of the pentagons
% and hexagons, and the length of a vertex diagonal of the

```

% hexagons. There are two possible inscribed circles but  
 % only one circumscribed circle.

```
z4 = ce * cosd(Pcv+vcv+Pcv+Pce);
s4 = vv; % edge length
s4h = 2*Hv; % vertex diagonal length
r4 = ce * sind(Pcv+vcv+Pcv+Pce); % decagon center to s4
rr4 = sqrt( (s4 / 2)^2 + (r4)^2 ); % decagon center to vertex
r4h = sqrt( (rr4)^2 - (s4h / 2)^2 ); % decagon center to s4h
```

```
% angsh = angle between v on one side of an edge of length s4,
% the center of the decagon, and v on other side of edge.
% angsh = angle between v on one side of an edge of length s4h,
% the center of the decagon, and v on other side of edge.
angs = 2 * asind( (s4 / 2) / rr4 );
angsh = 2 * asind( (s4h / 2) / rr4 );
```

```
dd1 = [-s4h/2, -r4h, z4];
dd2 = [ s4h/2, -r4h, z4];
dd3 = [-rr4*sind(angsh+angs/2), -rr4*cosd(angsh+angs/2), z4];
dd4 = [ rr4*sind(angsh+angs/2), -rr4*cosd(angsh+angs/2), z4];
dd5 = [-rr4*sind(angsh+3*angs/2), rr4*cosd(angsh+3*angs/2), z4];
dd6 = [ rr4*sind(angsh+3*angs/2), rr4*cosd(angsh+3*angs/2), z4];
dd7 = [-rr4*sind(angsh+angs/2), rr4*cosd(angsh+angs/2), z4];
dd8 = [ rr4*sind(angsh+angs/2), rr4*cosd(angsh+angs/2), z4];
dd9 = [-s4/2, r4, z4];
dd10 = [ s4/2, r4, z4];
```

```
% Now we find the coordinates of the center of the faces
% The top face is easy:
```

```
tc = [0, 0, z1];
```

```
% Next we have a pentagon that connects the centers of the top
% hexagons
```

```
z5 = cH * cosd(PcH);
s5 = HH;
```

```

r5 = cH * sind(PcH) * cosd(36);
rr5 = cH * sind(PcH);

phc1 = [-s5/2,r5,z5];
phc2 = [s5/2,r5,z5];
phc3 = [-s5*(.5+cos(2*pi/5)) , -(s5*sin(2*pi/5)-r5) , z5];
phc4 = [ s5*(.5+cos(2*pi/5)) , -(s5*sin(2*pi/5)-r5) , z5];
phc5 = [0 , -rr5 , z5];

% Now we have a pentagon that connects the centers of the
% middle pentagons

z6 = cH * cosd(Pcv + vcv + Pcv);
s6 = PP;
r6 = cH * sind(Pcv + vcv + Pcv) * cosd(36);
rr6 = cH * sind(Pcv + vcv + Pcv);

ppc1 = [-s6/2,-r6,z6];
ppc2 = [s6/2,-r6,z6];
ppc3 = [-s6*(.5+cos(2*pi/5)) , s6*sin(2*pi/5)-r6 , z6];
ppc4 = [ s6*(.5+cos(2*pi/5)) , s6*sin(2*pi/5)-r6 , z6];
ppc5 = [0 , rr6 , z6];

% The last one is a pentagon that connects the centers of the
% middle hexagons

z7 = cH * cosd(Pce + Hce + HcH);
s7 = 2 * HH * sind(54);
r7 = cH * sind(Pce + Hce + HcH) * cosd(36);
rr7 = cH * sind(Pce + Hce + HcH);

phhc1 = [-s7/2,r7,z7];
phhc2 = [s7/2,r7,z7];
phhc3 = [-s7*(.5+cos(2*pi/5)) , -(s7*sin(2*pi/5)-r7) , z7];
phhc4 = [ s7*(.5+cos(2*pi/5)) , -(s7*sin(2*pi/5)-r7) , z7];
phhc5 = [0 , -rr7 , z7];

pt = zeros(61,3);

```

```

pt(2,:) = [p1(1),p1(2),p1(3)];
pt(3,:) = [p2(1),p2(2),p2(3)];
pt(4,:) = [p3(1),p3(2),p3(3)];
pt(5,:) = [p4(1),p4(2),p4(3)];
pt(6,:) = [p5(1),p5(2),p5(3)];

pt(7,:) = [ pp1(1),pp1(2),pp1(3)];
pt(8,:) = [ pp2(1),pp2(2),pp2(3)];
pt(9,:) = [ pp3(1),pp3(2),pp3(3)];
pt(10,:) = [pp4(1),pp4(2),pp4(3)];
pt(11,:) = [pp5(1),pp5(2),pp5(3)];

pt(12,:) = [d1(1),d1(2),d1(3)];
pt(13,:) = [d2(1),d2(2),d2(3)];
pt(14,:) = [d3(1),d3(2),d3(3)];
pt(15,:) = [d4(1),d4(2),d4(3)];
pt(16,:) = [d5(1),d5(2),d5(3)];
pt(17,:) = [d6(1),d6(2),d6(3)];
pt(18,:) = [d7(1),d7(2),d7(3)];
pt(19,:) = [d8(1),d8(2),d8(3)];
pt(20,:) = [d9(1),d9(2),d9(3)];
pt(21,:) = [d10(1),d10(2),d10(3)];

pt(22,:) = [dd1(1),dd1(2),dd1(3)];
pt(23,:) = [dd2(1),dd2(2),dd2(3)];
pt(24,:) = [dd3(1),dd3(2),dd3(3)];
pt(25,:) = [dd4(1),dd4(2),dd4(3)];
pt(26,:) = [dd5(1),dd5(2),dd5(3)];
pt(27,:) = [dd6(1),dd6(2),dd6(3)];
pt(28,:) = [dd7(1),dd7(2),dd7(3)];
pt(29,:) = [dd8(1),dd8(2),dd8(3)];
pt(30,:) = [dd9(1),dd9(2),dd9(3)];
pt(31,:) = [dd10(1),dd10(2),dd10(3)];

pt(32,:) = [-dd1(1),-dd1(2),-dd1(3)];
pt(33,:) = [-dd2(1),-dd2(2),-dd2(3)];
pt(34,:) = [-dd3(1),-dd3(2),-dd3(3)];
pt(35,:) = [-dd4(1),-dd4(2),-dd4(3)];

```

```

pt(36,:) = [-dd5(1),-dd5(2),-dd5(3)];
pt(37,:) = [-dd6(1),-dd6(2),-dd6(3)];
pt(38,:) = [-dd7(1),-dd7(2),-dd7(3)];
pt(39,:) = [-dd8(1),-dd8(2),-dd8(3)];
pt(40,:) = [-dd9(1),-dd9(2),-dd9(3)];
pt(41,:) = [-dd10(1),-dd10(2),-dd10(3)];

```

```

pt(42,:) = [-d1(1),-d1(2),-d1(3)];
pt(43,:) = [-d2(1),-d2(2),-d2(3)];
pt(44,:) = [-d3(1),-d3(2),-d3(3)];
pt(45,:) = [-d4(1),-d4(2),-d4(3)];
pt(46,:) = [-d5(1),-d5(2),-d5(3)];
pt(47,:) = [-d6(1),-d6(2),-d6(3)];
pt(48,:) = [-d7(1),-d7(2),-d7(3)];
pt(49,:) = [-d8(1),-d8(2),-d8(3)];
pt(50,:) = [-d9(1),-d9(2),-d9(3)];
pt(51,:) = [-d10(1),-d10(2),-d10(3)];

```

```

pt(52,:) = [-pp1(1),-pp1(2),-pp1(3)];
pt(53,:) = [-pp2(1),-pp2(2),-pp2(3)];
pt(54,:) = [-pp3(1),-pp3(2),-pp3(3)];
pt(55,:) = [-pp4(1),-pp4(2),-pp4(3)];
pt(56,:) = [-pp5(1),-pp5(2),-pp5(3)];

```

```

pt(57,:) = [-p1(1),-p1(2),-p1(3)];
pt(58,:) = [-p2(1),-p2(2),-p2(3)];
pt(59,:) = [-p3(1),-p3(2),-p3(3)];
pt(60,:) = [-p4(1),-p4(2),-p4(3)];
pt(61,:) = [-p5(1),-p5(2),-p5(3)];

```

```

pt(62,:) = [tc(1),tc(2),tc(3)];

```

```

pt(63,:) = [phc1(1),phc1(2),phc1(3)];
pt(64,:) = [phc2(1),phc2(2),phc2(3)];
pt(65,:) = [phc3(1),phc3(2),phc3(3)];
pt(66,:) = [phc4(1),phc4(2),phc4(3)];
pt(67,:) = [phc5(1),phc5(2),phc5(3)];

```



```

pt(68,:) = [ppc1(1),ppc1(2),ppc1(3)];
pt(69,:) = [ppc2(1),ppc2(2),ppc2(3)];
pt(70,:) = [ppc3(1),ppc3(2),ppc3(3)];
pt(71,:) = [ppc4(1),ppc4(2),ppc4(3)];
pt(72,:) = [ppc5(1),ppc5(2),ppc5(3)];

pt(73,:) = [phhc1(1),phhc1(2),phhc1(3)];
pt(74,:) = [phhc2(1),phhc2(2),phhc2(3)];
pt(75,:) = [phhc3(1),phhc3(2),phhc3(3)];
pt(76,:) = [phhc4(1),phhc4(2),phhc4(3)];
pt(77,:) = [phhc5(1),phhc5(2),phhc5(3)];

pt(78,:) = -[phhc1(1),phhc1(2),phhc1(3)];
pt(79,:) = -[phhc2(1),phhc2(2),phhc2(3)];
pt(80,:) = -[phhc3(1),phhc3(2),phhc3(3)];
pt(81,:) = -[phhc4(1),phhc4(2),phhc4(3)];
pt(82,:) = -[phhc5(1),phhc5(2),phhc5(3)];

pt(83,:) = -[ppc1(1),ppc1(2),ppc1(3)];
pt(84,:) = -[ppc2(1),ppc2(2),ppc2(3)];
pt(85,:) = -[ppc3(1),ppc3(2),ppc3(3)];
pt(86,:) = -[ppc4(1),ppc4(2),ppc4(3)];
pt(87,:) = -[ppc5(1),ppc5(2),ppc5(3)];

pt(88,:) = -[phc1(1),phc1(2),phc1(3)];
pt(89,:) = -[phc2(1),phc2(2),phc2(3)];
pt(90,:) = -[phc3(1),phc3(2),phc3(3)];
pt(91,:) = -[phc4(1),phc4(2),phc4(3)];
pt(92,:) = -[phc5(1),phc5(2),phc5(3)];

pt(93,:) = -[tc(1),tc(2),tc(3)];

rot_angle = -PcH;
rot_matrix = [1, 0, 0
              0, cosd(rot_angle), sind(rot_angle)
              0, -sind(rot_angle), cosd(rot_angle)];

pt = pt * rot_matrix;

```

```
for i=1:93
    fprintf('soccer.dat;1','PT,%g,',i);
    fprintf('soccer.dat;1','%g,%g,%g\n',pt(i,1),pt(i,2),pt(i,3));
end
```

### Program 3 (coupled\_modes.m)

```
%
% coupled_modes
%
% Purpose: Find the spectrum of the TI with different number
%          of resonators
%
% Called: cartesian = convert to cartesian coordinates
%          y1c - y5c = the five spherical harmonics in cartesian
%                   coordinates. These functions also perform
%                   the beta and gamma rotations. See y1c for
%                   an example.
%
%
% Data for comparison
%

f0 = [3223 3224 3237 3238 3249];
f1 = [3167 3223 3236 3238 3245 3305 3307];
f2 = [3160 3177 3233 3236 3240 3302 3311];
f3 = [3160 3160 3191 3236 3236 3297 3310 3311];
f4 = [3159 3160 3168 3199 3236 3285 3310 3311 3319];
f5 = [3152 3160 3163 3169 3209 3268 3304 3310 3313 3319];
f6 = [3151 3156 3162 3167 3170 3239 3302 3308 3312 3316 3319];

%
% Uncoupled frequencies of the TI and resonatoras
%

fo = f0;
fR = [3241, 3241, 3241, 3241, 3241 3241];

nModes = length(fo);

for nRes = 1:6,
```

```

wo = fo*2*pi;           % sphere angular freq (rad/s)
wR = fR*2*pi;           % Resonator angular freq (rad/s)
rs = 8190.46/mean(wo);   % sphere radius
density = 2.7e3;         % density of Al Kg/m^3
ms = (4*pi/3)*rs^3*density; % sphere mass (Kg)
mR = 0.42; %ms*3.6e-4;   % transducer mass (Kg)

aeff = -0.300632587; % actually aeff/r
alpha = -2.86541;

ks = ms * wo.^2;
kR = mR * wR(1:nRes).^2;

%
% Location of resonators
%

phi = [60,-60,180,-120,0,120] * pi/180;
theta=[37.3773,37.3773,37.3773,79.1876,79.1876,79.1876]*pi/180;

resOrder = [4 6 5 2 3 1]; % order the resonators were put on TI
phi = phi(resOrder);
theta = theta(resOrder);

%convert to cartesian coords
[x, y, z] = cartesian(ones(size(phi)),theta, phi);

%
% Rotation angles of the pattern matrix
%

beta_rot = 1.0*ones(1,5);
gamma_rot = [-0.1 -0.1 -7.2 -7.2 0.0];

%
% Calculate the pattern matrix
%
```

```

B = zeros(nModes,nRes);
for i=1:nRes,
    B(:,i) = [y1c(x(i),y(i),z(i),beta_rot(1),gamma_rot(1)) ;
              y2c(x(i),y(i),z(i),beta_rot(2),gamma_rot(2)) ;
              y3c(x(i),y(i),z(i),beta_rot(3),gamma_rot(3)) ;
              y4c(x(i),y(i),z(i),beta_rot(4),gamma_rot(4)) ;
              y5c(x(i),y(i),z(i),beta_rot(5),gamma_rot(5))];
end;

%
% Mass weight matrix
%

gamma = [ (1/sqrt(ms)) * eye(nModes,nModes), zeros(nModes,nRes);
          zeros(nRes, nModes), (1/sqrt(mR)) * eye(nRes,nRes)];

%
% Mass matrix
%

M = [ ms * eye(nModes,nModes), zeros(nModes,nRes);
      mR * alpha * B', mR * eye(nRes,nRes)];

%
% Stiffness matrix
%

K = [ diag(ks), -kR(ones(nModes,1),:) .* alpha .* B
      zeros(nRes, nModes), diag(kR)];

%
% Put in mass weighted coords.
%

M = gamma * M;
K = gamma * K;

%

```

```
% Find the eigenvalues and eigenvectors
%

[U,D] = eig(inv(M)*K);

%
% Output the results
%

freqs = sqrt(diag(D))/(2*pi)
end;
```

#### Program 4 (y1c.m)

```

function result = y1c(x,y,z,beta_rot,gamma_rot)
%
% Purpose: Calculate the y1 spherical harmonic in
%          cartesian coordinates
%
% Inputs:  x = x position
%          y = y position
%          z = z position
%          beta_rot = rotation about the y axis
%          gamma_rot = rotation about the new z axis
%
% Outputs: result = spherical harmonic
%

Ry = [cos(beta_rot), 0, -sin(beta_rot);
      0,             1, 0;
      sin(beta_rot), 0,  cos(beta_rot)];

Rz = [ cos(gamma_rot), sin(gamma_rot), 0;
      -sin(gamma_rot), cos(gamma_rot), 0;
      0,               0,             1];

v = Rz*Ry*[x(:)';y(:)';z(:)'];

xp = v(1,:);
yp = v(2,:);
zp = v(3,:);

result=sqrt(15/(16*pi))*(xp.^2-yp.^2)./(xp.^2+yp.^2+zp.^2);

```

# Appendix D

## Letter of Permission

Most of chapter 2 was previously published in *Physical Review D*. It is reprinted with permission from *Physical Review D* **51**, 2546 (1995), “Spherical Gravitational Wave Antennas and the Truncated Icosahedral Arrangement” by S. Merkowitz and W. Johnson. Copyright 1995 The American Physical Society. Included below is a copy of the letter requesting permission for reprinting as well as the letter granting permission.



May 16, 1995

María Lebrón  
Associate Publisher  
The American Physical Society  
One Physics Ellipse  
College Park, MD 20740-3844

Dear Ms. Lebrón,

I am preparing my Ph.D. dissertation entitled: "Truncated Icosahedral Gravitational Wave Antenna" to be reproduced and distributed by UMI Dissertation Services. I would appreciate your permission to use the materials in our paper: "Spherical gravitational wave antennas and the truncated icosahedral arrangement", Stephen Merkowitz and Warren Johnson, Physical Review D **51**, 2546 (1995). Credit to this journal will be given.

Thank you very much for your timely response.

Sincerely,

Stephen Merkowitz

# The American Physical Society

One Physics Ellipse, College Park, Maryland 20740-3844 (301) 209-3200

June 19, 1995

Code: 950619ME

Stephen Merkowitz  
Louisiana State University  
Dept of Physics and Astronomy  
Baton Rouge, LA 70803-4001

Dear Mr. Merkowitz:

This is further to your request for permission to use materials from The American Physical Society (APS) journals.

Permission is hereby granted for the one time reproduction -- in print only and as per the requirements indicated below -- of the following:

*Physical Review D* 51, 2546 (1995), "Spherical gravitational wave antennas and the truncated icosahedral arrangement" by S. Merkowitz and Warren Johnson;

to appear in your Ph.D. dissertation entitled "Truncated Icosahedral Gravitational Wave Antenna" to be reproduced and distributed by UMI Dissertation Services.

- [XX] 1. The following credit line must appear in all copies (please fill in the information in CAPITAL LETTERS): "Reprinted (abstracted) with permission from FULL CITATION. Copyright YEAR The American Physical Society."
- [XX] 2. NOTE: This permission does not apply to figures, tables, or other materials credited to sources other than the APS.
- [ ] 3. Obtain the authors' permission to use the material. The author's address can be obtained from the article.
- [ ] 4. Remit a permissions fee of \$\_\_\_\_. THIS LETTER WILL SERVE AS YOUR INVOICE. Please make check payable to The American Physical Society and enclose a copy of this letter with your remittance.  
**PLEASE NOTE: PERMISSION IS NOT VALID UNTIL PAYMENT IS RECEIVED.**

Thank you for requesting permission to use materials copyrighted by the APS. Please do not hesitate to contact us should you have further questions.

*Maria L. Lebron*

Maria L. Lebron, Ph.D.  
Associate Publisher

# Vita

Stephen Merkowitz was born on July 8, 1968 in Boulder, Colorado to Maria and David Merkowitz. In 1986 he graduated from the selective science and technology program at Eleanor Roosevelt High School in Greenbelt, Maryland. He attended the University of Colorado at Boulder and earned a B.A. in physics in 1989.

During the summer of 1988, he served an internship at NASA's Goddard Space Flight Center where he analyzed data from the International Ultraviolet Explorer (IUE) satellite. Afterwards, he continued working with IUE data at the Laboratory for Atmospheric and Space Physics (LASP) at the University of Colorado, where he also worked with data from the Infrared Astronomical Satellite (IRAS).

He was awarded a teaching assistantship from Louisiana State University and began graduate studies there in the fall of 1989. He immediately began research in gravitational wave detection with professors Warren Johnson and William O. Hamilton, and was awarded a research assistantship in 1991. He received his master's degree in physics in the fall of 1994, and is currently a candidate for the degree of Doctor of Philosophy.

DOCTORAL EXAMINATION AND DISSERTATION REPORT

Candidate:

Stephen Michael Merkowitz

Major Field:

Physics

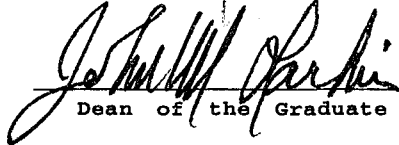
Title of Dissertation:

Truncated Icosahedral Gravitational Wave Antenna

Approved:

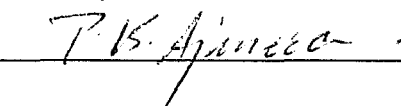
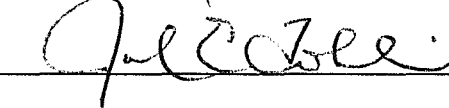
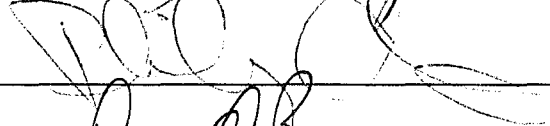


Major Professor and Chairman



Dean of the Graduate School

EXAMINING COMMITTEE:



Date of Examination:

6/23/95